1949

Modelling of singly charged ion-atom collisions in fusion plasma

Thesis for the Degree of Doctor of
Philosophy (PhD)

Musab Salameh Ali Al-Ajaleen

Supervisor:
Dr. Károly Tőkési

UNIVERSITY OF DEBRECEN
Doctoral Council of Natural Sciences and
Information Technology
Doctoral School of Physics
Debrecen, 2024

Prepared at
The University of Debrecen
PhD school of Physics
and
The institute for Nuclear Research
(ATOMKI)

Készült:
Debreceni Egyetem
Fizikai Tudományok Doktori Iskolában
és
az Atommagkutató intézetben
(ATOMKI)

Hereby I declare that I prepared this thesis within the Doctoral Council of Natural Sciences and Information Technology, Doctoral School of Physics, University of Debrecen in order to obtain a PhD Degree in Natural Sciences at Debrecen University.
The results published in the thesis are not reported in any other PhD theses.

Debrecen, 2024. . . . . *Musab Salameh Ali Al-Ajaleen*
Candidate

Hereby I confirm that Musab Salameh Ali Al-Ajaleen candidate conducted his studies with my supervision within the Atomic and Molecular Doctoral Program of the Doctoral School of Physics between 2020 and 2024. The independent studies and research work of the candidate significantly contributed to the results published in the thesis.
I also declare that the results published in the thesis are not reported in any other theses.
I support the acceptance of the thesis.

Debrecen, 2024. . . . . *Dr. Károly Tőkési*
Supervisor

Modelling of atomic processes in fusion plasma

Dissertation submitted in partial fulfilment of the requirements for the doctoral (PhD) degree in physics

Written by Musab Salameh Ali Al-Ajaleen certified physicist

Prepared in the framework of the doctoral school of Physics of the University of Debrecen
Atomic and Molecular programme

Dissertation advisor: Dr. Károly Tőkési

The official opponents of the dissertation:

Dr. ………………… …..………………..
Dr. ………………… …..………………..

The evaluation committee:

chairperson: Dr. ………………… …..………………..
members: Dr. ………………… …..………………..
Dr. ………………… …..………………..
Dr. ………………… …..………………..
Dr. ………………… …..………………..

The date of the dissertation defence: …………….. 20…

Contents

List of Publications

Publication related to the dissertation.

1. **M. Al-Ajaleen**, A Taoutioui and K. Tőkési. Charge transfer and ionization cross-sections in collisions of singly charged lithium ions with helium and nitrogen atoms. *Plasma Physics and Controlled Fusion* **65** (2023) 065002. **DOI** 10.1088/1361-6587/acc6ed
   Impact Score: 2.53, Q1.

2. **M. Al-Ajaleen** and K. Tőkési. Total and differential ionization cross sections in collision between nitrogen atom and singly charged sodium ion. *Scientific Reports* **13** (2023) 14080. **DOI** 10.1038/s41598-023-41134-0
   Impact Factor: 4.6, D1.

3. **M. Al-Ajaleen** and K. Tőkési. Total and Differential Cross Sections of Collision of Singly Charged Sodium Ions with Noble Gases, (under review by *Scientific Reports*).
   Impact Factor: 4.6, D1.

4. **M. Al-Ajaleen** and K. Tőkési. Interaction of Protons with noble Gas Atoms: Total and Differential Ionization Cross Section. *Atoms* **12** (2024), 28. DOI 10.3390/atoms12050028
   Impact Factor: 1.8, Q2.

List of Conference Publications and Posters

Conference Publication

1. **M. Al-Ajaleen**, A. Taoutioui and K.Tőkési, *Ionization and electron capture processes induced in collisions between singly charged ions and nitrogen atom*, 48th EPS Conference on Plasma Physics, June 27, 2022, Amsterdam (online), Netherlands. **Publication:** P1b.405

Conference short talk

1. **M. Al-Ajaleen** and Károly Tőkési, *Interaction of electrons and positrons with two-dimensional proton lattice*. Virtual Meeting on the Molecular Dynamics in the GAS phase (MD-GAS 2021) - COST Action (CA18212): 2nd General Meeting, October 4, 2021.

Conference Posters

1. **M. S. Al-Ajaleen** and Károly Tőkési, *Interaction of electrons and positrons with protons aligned in one-dimension line*. The 27th International Symposium on ion-atom collisions-virtual format (ISIAC 2021), July 16, 2021, Cluj-Napoca, Romania.
2. **M. Al-Ajaleen** and Károly Tőkési, *Interaction of electrons and positrons with two-dimensional proton lattice*. The 32nd International Conference on Photonic, Electronic and Atomic Collisions- virtual format (ViCPEAC 2021), July 20, 2021, Ottawa, Canada.
3. **M. Al-Ajaleen**, A. Taoutioui and K.Tőkési, Ionization and charge exchange cross sections induced in collisions between singly charged ions and He(1s) and N(2p) atoms, International Conference on Many Particle Spectroscopy of Atoms, Molecules, Clusters and Surfaces (MPS-2022), June 15-17, 2022, Turku, Finland.
4. **M. Al-Ajaleen**, A. Taoutioui and K.Tőkési, *Ionization and electron capture processes induced in collisions between singly charged ions and nitrogen atom*, 48th EPS Conference on Plasma Physics, June 27, 2022, Amsterdam (online), Netherlands.
5. **M. Al-Ajaleen**, A. Taoutioui and K.Tőkési, Ionization and charge exchange cross sections in collisions between singly charged ions and ground-state atomic nitrogen, 14th European Conference on Atoms Molecules and Photons (ECAMP14), June 27-July 1, 2022, 2022, Vilnius, Lithuania.
6. **M. Al-Ajaleen**, A. Taoutioui and K.Tőkési, *Ionization and electron capture processes induced in collisions between Li and He(1s) and N(2p) atoms*, 32nd Symposium on Fusion Technology (SOFT), September 18, 2022, Dubrovnik, Croatia.

Other Publication Not related to the dissertation.

1. **Musab S. Al-Ajaleen** and K. Tőkési. Interaction of Electrons and Positrons with Protons Aligned in One-Dimension Line. *Atoms* **11** (2023) 46. DOI 10.3390/atoms11030046
   Impact Factor: 1.8, Q2.

2. **M. Al-Ajaleen** and K. Tőkési. Interaction of electrons and positrons with two-dimensional artificially generated proton lattice and with carbon lattice. *Physica Scripta* **98** (2023) 075404. DOI 10.1088/1402-4896/acd969
   Impact Factor: 3.081, Q2.

Introduction

In ion-atom collisions, inelastic electron processes have a crucial significance across multiple fields. Notably, these processes have profound implications in particle beam therapy, a field primarily utilizing beams of carbon ion and proton [1,2]. Additionally, they contribute significantly to the modelling and diagnostics of fusion plasmas within tokamak reactors.

Of paramount importance among these phenomena is ionization, a phenomenon of great significance in radiation physics and the exploration of atomic and molecular structures [3]. Its relevance extends further into the study of fusion plasma. Within magnetically confined fusion plasmas, such as those in tokamaks, the distributions and concentrations of excited impurity ions critically shape the profiles of the plasma edge. To accurately assess plasma parameters – encompassing temperature, impurity concentrations, density, and plasma turbulence [4] – a diagnostic approach involving the injection of a high-speed neutral atomic beam into the plasma edge is employed, enabling high spatiotemporal resolution.

The collision of the injected neutral atomic beam with plasma constituents results in the generation of emission lines, offering enhanced insights into the profiles of the plasma edge. This is particularly relevant in the context of tokamaks, recognized as the most promising design for achieving magnetic confinement-based fusion energy. However, the stability of these systems can be compromised, leading to plasma disruptions [5,6] characterized by rapid losses of magnetic and thermal energy, termed thermal quench. Moreover, such disruptions impose substantial forces on reactor components and walls upon loss of plasma confinement. In light of this, effective plasma disruption mitigation [7,8] is imperative for ensuring the safe and dependable operation of fusion reactors.

Disruption mitigation strategies encompass various approaches, such as the injection of significant gas quantities into the plasma to expedite cooling and quenching, thereby minimizing energy release during disruptions. This process, while effective, introduces a notable quantity of impurities from the injected gas into the plasma [9]. A range of noble gases and methods [7,8,10–12] have been proposed and scrutinized for their efficacy in plasma disruption mitigation. Due to differences in mass, ionization, and reflection coefficients, noble gas particles are anticipated to exhibit distinct behaviours at the plasma boundary relative to the majority of plasma constituents [13].

Another vital application of gas injection in tokamaks is plasma diagnostics, where injected gases, including neutral alkali beams such as lithium and sodium with an energy around 60 keV, have proven invaluable for measuring plasma turbulence and electron density profiles, especially within the scrape-off layer and plasma edge [14–19].

In the realm of fusion research, various neutral high-energy beams have emerged as valuable tools. Hydrogen isotopes and helium are prime examples, as they find application both in heating the fusion plasma and in its diagnostic processes within the tokamak reactor's vacuum vessel [4,20–25]. A different strategy involves the utilization of nitrogen seeding, aimed at cooling the edge plasma within tokamak reactors [26].

In the quest for improved magnetic fusion plasma performance and enhanced protection for plasma-facing components, a range of fusion experiments have endorsed the use of liquid lithium [27–29]. Notably reactive, lithium readily ionizes, giving rise to lithium ions that can collide with neutral atoms (such as helium and nitrogen) at the plasmas edge.

A noteworthy study conducted by Wolfrum et al. [30] explored the potential of sodium as an alternative diagnostic beam to lithium. This choice was underpinned by sodium's distinct advantages, including lower emitter temperature and a larger charge exchange cross section, particularly in collisions involving helium and carbon impurities.

The precise modelling and management of the edge plasma, which interacts with the tokamak reactor's blanket and divertor and to facilitate accurate diagnostics, a deep understanding of the cross-sectional properties of the collision systems within the edge plasma is imperative. The acquisition of precise cross-sectional data plays a pivotal role in effectively simulating and regulating the plasma in proximity to the tokamak reactor's wall and related components.

In this dissertation, we present a classical treatment of an inelastic single electron processes in collision systems related to fusion plasma. However, the expanded range of impact energy within the total cross section encompasses many applications such as astrophysics, and controlled thermo-nuclear fusion research [31–34]. We focused our studies on collision systems of singly charged ion projectiles with atomic targets; the projectiles studied in this dissertation are proton, lithium, and sodium ions, while the targets are nitrogen and noble gases, namely, helium, neon argon, krypton, and xenon. The collision system is reduced to a three-body problem and solved using the classical trajectories Monte Carlo method [35–37].

Chapter 1 provides a brief description of the main collisional processes induced during atom-atom and ion-atom collisions, velocity regimes, and brief descriptions for some theoretical approaches. In Chapter 2, the theoretical approach of the CTMC calculation method using Garvey-type distance-dependent model potential is described. In Chapter 3, discussions of our findings are presented. Finally, a summary and concluding remarks are given in Chapter 4. References are provided at the end of this dissertation.

Chapter 1 Collision system

This dissertation is dedicated to exploring single-electron processes, with particular emphasis on ionisation processes concerning the targets and electron capture onto the projectile. This dissertation is committed to delivering detailed single (SDCS), double-differential (DDCS), and total cross-sectional (TCS) information of collision systems between singly charged ions with neutral targets. In this section, we present a general theoretical description of ion-atom collision system.

1.1 Collision processes

In ion-atom collision, fundamental processes are possible depending on the conditions of the collision and the characteristics of the target and the projectile. The exits channel depends on many factors, such as, energy of the projectile, the binding energy of the electron, and the impact parameter. A brief description of ionisation, electron capture, and excitation channels is introduced the following sub-sections.

1.1.1 Ionisation

Ionisation (figure 1.1) is the process of ejection of one or more electrons from an atom or molecule. Ionisation can be direct or indirect. In direct ionisation, a charged projectile such as electrons, protons, and ions collide with the target. In indirect ionisation, the target interacts with neutral particles and photons.

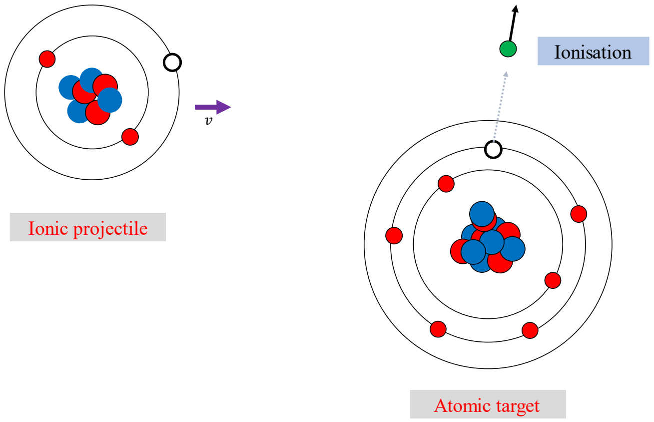

Figure 1.1 A schematic diagram of ionisation in ion-atom collision.

Focusing on direct ionisation by singly charged ions, when an ion collides with an atom, the ion transfers energy to an electron of the atom; if the transferred energy is larger than or equal to the binding energy of the electron then the electron is ejected from the atom. There is another possibility where an electron is ejected from the ionic projectile in the same procedure. The following reaction shows ionisation process in a collision between singly charged ion (A^{+}) and an atom (B):

$$A^{+} + B \longrightarrow \begin{cases} A^{+} + B^{+} + e^{-} \\ A^{2+} + B + e^{-} \end{cases} \tag{1.1}$$

The cross section of the ionisation channel increases with decreasing the binding energy of a specific shell, hence the ionisation of an electron from outer shells is easier than the ionisation from inner shells, because outer shells have lower binding energies compared to inner shells, see table 2.2.

1.1.2 Electron capture

When an ion collides with an atom, an electron from the atom might be captured by the ion, this process is called electron capture. There are two main conditions for electron capture to take place, the capturer should have a higher charge than the colliding partner, or the capturer should have a high kinetic energy. The cross section of the electron capture (figure 1.2) channel increases by increasing the charge of the ion and/or its kinetic energy.

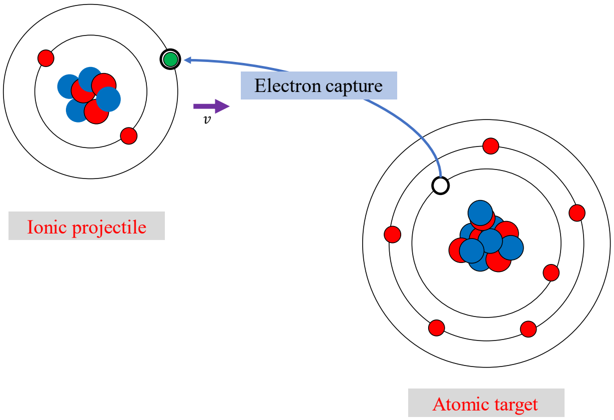

Figure 1.2 A schematic diagram of electron capture in ion-atom collision.

The electron capture process happens in two steps, firstly, when the ion approaches the atom, the nucleus of the ion attracts an electron from the atom, secondly, the electron is captured by the ion leaving a singly charged ion, see the following reaction which shows the electron capture process in a collision between singly charged ion (A^+) and an atom (B):

$$A^+ + B \longrightarrow A + B^+ \tag{1.2}$$

1.1.3 Excitation

In ion-atom collision, the ion might transfer kinetic energy to the atom without ionising it, the energy is not sufficient to eject an electron, however, it is enough to elevate the electron to a higher energy shell, this process is called excitation (figure 1.3).

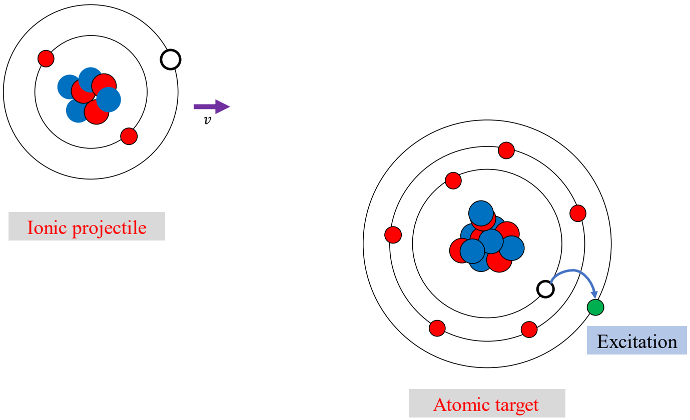

Figure 1.3 A schematic diagram of excitation in ion-atom collision.

The following reaction shows the excitation process in a collision between singly charged ion (A^+) and an atom (B), we see no changes on the charge of the interacting particles:

$$A^+ + B \longrightarrow \begin{cases} A^{+*} + B \\ A^+ + B^* \end{cases} \tag{1.3}$$

1.2 Velocity regimes of collision processes

The velocity regime of ionisation, excitation, and electron capture processes depend on the relative velocity between the projectile and the target's electron. There are three main regimes, which are, low-velocity, intermediate-velocity, and high-velocity regimes. The boundary between the different velocity regimes is not sharp, and the relative importance of the different processes can vary depending on the specific collision system.

In the low-velocity regime, the projectile has a very low velocity compared to the electron, the dominant process is electron capture [38]. This process is favoured low-velocity regime because the kinetic energy is not sufficient to overcome the electrostatic attraction between the projectile ion and the target electron. The cross section of electron capture increases with decreasing velocity because at lower velocities, the ions spend more time near the target atom, increasing the chances of electron capture. In the intermediate-velocity regime where the projectile and electron have relatively close velocities, all three processes have relatively equal cross sections [39]. In the high-velocity regime, the projectile is much faster than the electron, where the kinetic energy of the colliding particles is very high, the dominant processes are ionisation and excitation [40]. At high velocities, the kinetic energy is more than enough to overcome the binding energy of the electrons to induce ionisation or excitation depending on several factors. In this regime, the cross sections of ionisation and excitation are significantly high because the impact energy is much greater.

1.3 Theoretical models

This section is devoted to present some theoretical models used to calculate cross sections in atom-atom and ion-atom collisions.

1.3.1 First Born Approximation

The first Born approximation (FBA) is a theoretical method used in quantum mechanics to calculate scattering amplitudes and cross-sections for the interaction between a projectile and a target, typically in the context of atomic or molecular physics. It was first introduced by Max Born in 1926 [41] as a way to describe electron-atom scattering processes, marking one of the earliest attempts to apply quantum mechanics to calculate scattering cross-sections. Born does not seem to have applied the approximation that now carries his name; instead, it was initially employed by Bethe in 1930 [42]. Bell et al. [41] used the first born approximation to calculate the excitation and ionisation cross sections by electron, proton, and atomic impact.

The first Born approximation primary purpose lies in the computation of scattering amplitudes and cross sections for particle interactions with a target in quantum systems, frequently finding application in atomic and molecular physics to gain insights into how electrons or other particles interact with atoms or molecules when subjected to an external potential. This theoretical framework provides a relatively simple and computationally tractable method for calculating scattering cross-sections, making it an accessible starting point for more advanced quantum mechanical scattering theories, such as higher-order Born approximations [43–45]. However, the first Born approximation comes with its limitations. Being a first-order approximation, it may not accurately describe scattering processes at very high energies or when strong interactions are involved. It relies on the assumption that the interaction potential between the projectile and target is weak, which may not hold true in all situations.

The underlying assumptions of this approximation include the presumption of a weak interaction potential, allowing for a perturbative treatment, and the description of initial and final states of the system using simple wave functions, typically represented as plane waves for the incoming and outgoing states. Moreover, the interaction between the projectile and the target occurs over a relatively short period of time, hence, this allows to neglect any time-dependence in the interaction potential. Furthermore, projectile and target do not undergo significant rearrangement of their internal structure during the scattering process. Beyond the first Born approximation, higher order Born approximations like the Second Born Approximation and the Third Born Approximation can be derived to enhance accuracy.

1.3.2 Continuum Distorted Wave (CDW) method and Continuum Distorted Wave-Eikonal Initial State (CDW-EIS) method

The Continuum Distorted Wave (CDW) method [46–48] serves a primary purpose, focusing on characterizing the interaction between charged particles, predominantly electrons or ions, and atoms or molecules in the continuum region. Its applications encompass the calculation of cross-sections and scattering amplitudes for various collision processes, such as electron impact ionization or electron scattering from molecules.

The CDW method offers several advantages. It provides a semi-classical description that harmoniously combines elements of quantum mechanics and classical physics. Its computational efficiency and ability to handle intricate target structures make it a preferred choice. Moreover, it often plays a pivotal role in interpreting experimental data, providing insights into collision dynamics.

Nevertheless, CDW also comes with its set of disadvantages. Being a semi-classical method, it tends to overlook certain quantum mechanical effects, particularly at low energies, limiting its accuracy for specific processes. It relies on various approximations, introducing potential errors in results. Furthermore, when applied to highly excited states or interactions involving heavy ions, its accuracy may falter.

The CDW method is grounded in several key assumptions. These include the assumption that the incident particle follows a classical trajectory in the field of the target atom or molecule. Additionally, it assumes that the target electrons remain in their bound states during the collision and that the incident particle interacts with the target electrons via a screened Coulomb potential.

The potential utilized in CDW calculations predominantly takes the form of a screened Coulomb potential, thoughtfully accounting for the screening effects of the target electrons, thus contributing to the method's effectiveness in describing collision processes involving charged particles and atoms or molecules in the continuum region.

The Continuum Distorted Wave-Eikonal Initial State (CDW-EIS) Method [49,50] is a simplification of the CDW method, in contrast to the CDW method, which employs the complete electronic Coulomb wavefunction, CDW-EIS leverages the asymptotic behaviour of this wavefunction, specifically, the logarithmic Coulomb phase. It provides reasonably accurate results for a wide range of collision processes and various collision systems, including heavy ions. Like the CDW method, CDW-EIS is still semi-classical in nature and may not fully account for all quantum mechanical effects. Moreover, Computational requirements can be significant, especially for complex collision systems.

1.3.3 Atomic Orbital Close Coupling method

The Atomic Orbital Close Coupling (AOCC) method is a semi-classical approach [51,52] used in the field of atomic, molecular, and nuclear physics to study collision processes involving atoms and molecules. In AOCC, the wave function of the system is expanded in terms of a set of basis functions [53], which are typically atomic or molecular orbitals. The AOCC considers the following assumptions, the electrons and the nuclei are treated quantum mechanically and classically, respectively, moreover, the collision is treated as a one-dimensional process. Furthermore, the scattering equations are the core of AOCC, in which they are a set of coupled integro-differential equations. The scattering equations describe the behaviour of the colliding particles as they interact with each other and the target system, providing information about scattering amplitudes, cross-sections, and other properties of the collision process.

AOCC exhibits remarkable accuracy when describing collision processes, especially when employing a large number of basis functions. However, the high accuracy comes at the cost of complex computations, because solving the scattering equations can be computationally demanding, particularly when dealing with complex systems. Over the years, AOCC has undergone significant development, with researchers continually refining the methodology and expanding its applicability [52,54]. A development of AOCC is the molecular close-coupling

(MOCC) method [55,56], which handles molecular targets more effectively. While AOCC provides accurate results, it is computationally intensive and may not always be feasible for large-scale systems. To mitigate this, approximations and simplifications are often employed to reduce the computational burden while maintaining a reasonable level of accuracy.

1.3.4 Oppenheimer-Brinkman-Kramers (OBK) approximation

The Oppenheimer-Brinkman-Kramers (OBK) approximation [57–59], named after its contributors J. Robert Oppenheimer [60], and George Brinkman and Hendrik Anthony Kramers [61]. It was developed independently by these physicists and serves the primary purpose of describing the motion of nuclei in molecules during chemical reactions, simplifying the quantum mechanical treatment of molecular dynamics by separating the motion of electrons and nuclei.

The OBK approximation offers several advantages, including the simplification of the quantum mechanical description of molecular dynamics by separating nuclear and electronic motions, treating electrons as moving on a fixed nuclear framework and nuclei as classical particles, thereby reducing computational complexity, and providing a reasonable approximation for many molecular processes, particularly in cases where the nuclei's motion is significantly slower than that of electrons. Hence, in its nature, the OBK approximation is a semi-classical method that combines classical treatment of nuclei with quantum mechanical treatment of electrons.

However, the OBK approximation has its limitations. It is not accurate for describing processes where nuclear motion significantly impacts electronic structure or when nuclei move at high speeds. Moreover, it is unsuitable for describing phenomena involving nuclear quantum effects, such as hydrogen tunnelling.

Chapter 2 Theory

In the realm of theoretical physics and computational chemistry, the Classical Trajectory Monte Carlo (CTMC) simulation has emerged as a powerful tool with diverse applications, spanning a wide spectrum of collision processes [35,36,62–67]. Notably, this methodology has found considerable success in investigating hydrogen-hydrogen atom collisions across a range of velocities. The origins of CTMC simulations trace back to the pioneering work of Wall et al. [68], who conducted the first trajectory calculations for collinear molecular $H + H_2$ reactions on early computing machines. However, their initial efforts were limited by the computational resources of the time, yielding a relatively low number of trajectories and inadequate statistical precision for reaction rate determination. Subsequent advancements in the field were spearheaded by Blais and Bunker [69], who conducted the first true Monte Carlo calculation for this reaction. It is worth noting that the CTMC method's extensive utilization in atom-molecule collisions, as elucidated by Bunker in his seminal works [69,70], underwent distinct methodological adaptations when employed in collision studies involving charged particles and atoms. The long-range Coulomb interaction and attractive singularities inherent to such collisions necessitated specialized treatment [66,71]. The assessment of the Monte Carlo method's efficacy was further explored by Burgess, Percival, and their contemporaries [66]. Additionally, Abrines and Percival delved into the realm of ion-atom collisions [64], while Olson and Salop expanded the frontiers of CTMC calculations [72]. Their work extended the method's scope to the study of ion impacts on hydrogen atoms, including an exploration of projectile charge state-dependent charge transfer and ionization cross-sections.

I delved into the fundamental principles and methodologies underlying my PhD research, which centres around the development and application of a 3-body Monte Carlo (CTMC) approach. The CTMC method is a non-perturbative computational technique that employs numerical solutions to classical equations of motion [63,65]. This choice is well-founded since, at ordinary temperatures, the wavelengths associated with the motion of atoms and molecules are significantly shorter than the effective range of interaction between them [63,72].

Within the CTMC framework, the primary focus is on computing trajectories for three essential particles: the ionic projectile, the target's core, and the active electron of the target. These trajectories are governed by a Garvey-type distance-dependent model potential [73,74]. A pivotal element of this approach lies in the sampling of initial coordinates of the active electrons in both coordinate and momentum space. To achieve this, an initial ensemble, often referred to as the 'micro-canonical distribution,' is meticulously constructed to mimic the spatial and momentum properties of the initial state. Random selection techniques, particularly employing the Monte Carlo method, are instrumental in determining these initial conditions. Subsequently, my study proceeds by numerically solving Hamilton's equations for a substantial number of trajectories, each characterized by a randomly chosen set of relevant impact parameters. One of the distinctive advantages of the CTMC approach is its ability to simulate various reaction channels within the same framework. This includes the exploration.

2.1 Classical model of the collision system

The collision system consisting of ionic projectile and atomic target is reduced to a three-body system. The atomic target is described using the Single Active Electron (SAE) approximation, employing a distance-dependent model potential by Garvey. In this model, solely the outermost electron in its ground state participates in the collision dynamics, serving as the active electron, while the remaining bound electrons are deemed inactive [73,74]. The ionic projectile is described using the same approximation but with no electrons, see figure 2.1. For convenience, in further discussion we will refer to the previous bodies as projectile (P), target (T) and electron (e).

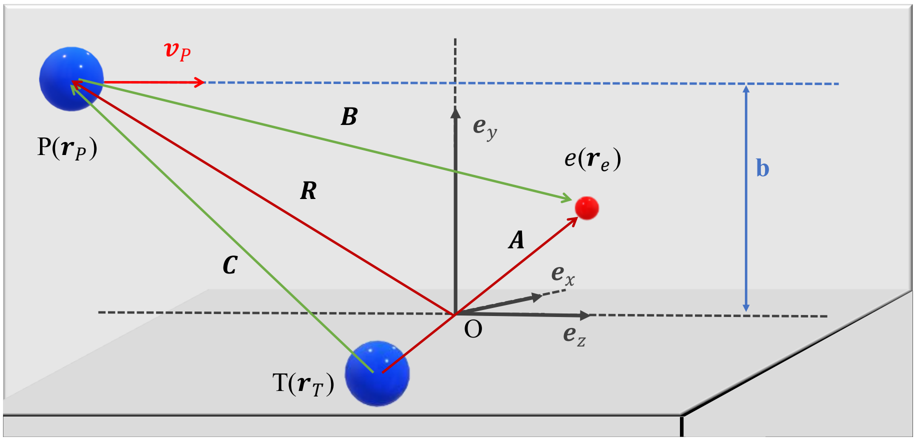

Figure 2.1 Schematic illustration of the relative position vectors of the particles involved in 3-body collisions. $\boldsymbol{A} = \boldsymbol{r}_e - \boldsymbol{r}_T$, $\boldsymbol{B} = \boldsymbol{r}_P - \boldsymbol{r}_e$, $\boldsymbol{C} = \boldsymbol{r}_T - \boldsymbol{r}_P$, and $\boldsymbol{R}$ is the position vector of the projectile with respect to centre-of-mass of the target system, and b is the impact parameter.

For the computer simulation of the collision process, a multi-step process crucial for understanding the dynamics of ionic projectiles colliding with atomic targets. This intricate experiment comprises three pivotal steps, each meticulously designed to ensure the reliability and accuracy of the results [64]. In Step 1, the system is meticulously prepared, with initial conditions selected from a statistical distribution that closely mimics the real distributions of ionic projectiles and atomic targets. Additionally, careful measures are taken to ensure that these particles start sufficiently far apart to avoid any mutual influence, and the impact parameter is judiciously adjusted to maintain precision. Step 2 involves the numerical solution of the equations of motion for the 3-body system, where the equations are solved while maintaining a significant separation between the projectile and the target, minimizing perturbations to their orbits during the collision. Finally, in Step 3, the output analysis is conducted, with recorded data ready for subsequent examination and interpretation. It is imperative to highlight that achieving accuracy in cross-section calculations necessitates the execution of a substantial number of trajectories, underscoring the importance of each step in this intricate experimental process.

2.2 Equations of motion

2.2.1 Garvey type distance-dependent model potential

The nuclear independent-particle model (IPM) [75] model relies on the utilization of phenomenological analytic shell and optical-model potentials as its core components. IPM has played a pivotal role in the calculation of various nuclear properties, including but not limited to nuclear elastic and inelastic scattering cross sections and transition probabilities. Green et al.'s study in 1969 [76] aimed to provide an analytical characterization of the universal Thomas-Fermi potential [77,78] as a starting point by developing IPM model. They sought to apply this analytic atomic IPM to the realm of applied atomic physics. In their groundbreaking work, Green et al. [76] analysed the Thomas-Fermi screening functions, employing the two-parameter Verhulst function [79] to facilitate their investigations.

Notably, Green et al. [76] refined their models through empirical adjustments of the two parameters associated with the screening function, enhancing predictive accuracy for each atom. Green et al. work in 1975 [80] further refined the model. In this context, empirical adjustments for neutral atoms allowed for the fixation of one parameter, based on a Thomas-Fermi-like dependence on atomic number Z, across all elements. This optimization left only one parameter requiring empirical adjustment for each element.

The scope of the IPM potential determination in Green et al.'s 1969 study [76] encompassed atoms and positive ions with atomic numbers ranging from 36 to 54, while extending to a select few ions with $54 < Z \leq 57$. It is important to note that Garvey et al.'s 1975 work [73] represented an extension and enhancement of the modified form of Hartree-Fock theory (MHF) initially developed by Bass et al. [81] for neutral atoms, Szydlik et al. [82] for atoms and ions with $Z \leq 18$, and Green et al. [80] for atoms and ions within the range of $18 < Z \leq 36$.

The model potential based on Green et al.'s [76] calculations and developed by Garvey et al. [73] has the form:

$$V(\boldsymbol{r}) = q\frac{Q(\boldsymbol{r})}{\boldsymbol{r}} \tag{2.1}$$

Where q is a test charge, $\boldsymbol{r}$ is the interaction separation, and $Q(\boldsymbol{r})$ is the distance-dependent effective charge. The effective charge is given by the formula:

$$Q(\boldsymbol{r}) = Z - (N-1)\left(1 - \Omega^{-1}(\boldsymbol{r})\right) \tag{2.2}$$

Where Z and N are the nuclear charge and the total number of electrons, respectively. A special case that the model potential reduces to a pure Coulombic potential for the case of hydrogen. The function $\Omega(\boldsymbol{r})$ has the form:

$$\Omega(\boldsymbol{r}) = \frac{\eta}{\xi}\left(e^{r\xi} - 1\right) + 1 \tag{2.3}$$

The potential parameters ξ and η can be acquired in a manner that minimizes the energy associated with a specific atom or ion. The effective charge form gives the model potential the correct asymptotic for small and large interaction separations, given in the next formulae:

$$\lim_{r \to 0} Q(\boldsymbol{r}) = Z \tag{2.4}$$

$$\lim_{r \to \infty} Q(\boldsymbol{r}) = Z - (N-1) \tag{2.5}$$

Figure 2.2 shows the effective charge of two examples, ionic sodium and nitrogen core, by nitrogen core we mean atomic nitrogen with excluding the outermost active electron.

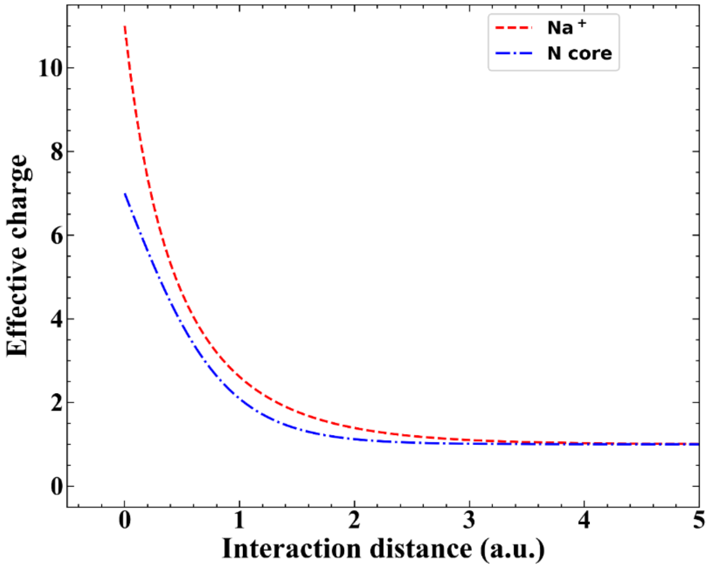

Figure 2.2 Effective charge of, red dashed line: singly ionised sodium, and blue dashed-dotted line: nitrogen core.

The potential parameters ξ and η have the following forms for the projectile (P):

$$\eta_P = \eta_P^o + \eta_P^1(Z_P - N_P - 1) \tag{2.6}$$

$$\xi_P = \xi_P^o + \xi_P^1(Z_P - N_P - 1) \tag{2.7}$$

And for the target (T):

$$\eta_T = \eta_T^o + \eta_T^1(Z_T - N_T) \tag{2.8}$$

$$\xi_T = \xi_T^o + \xi_T^1(Z_T - N_T) \tag{2.9}$$

The parameters η_i^o, η_i^1, ξ_i^o, and ξ_i^1 are listed by Garvey et al [73]. The parameters η_i^o, η_i^1, ξ_i^o, and ξ_i^1 of the atoms and ions studied in this thesis are listed in table 2.1.

Table 2.1 The parameters values of the particles included in the study.

	Z	ξ^o	ξ^1	η^o	η^1
He	2	2.625	1.2996	1.770	1.1402
Li	3	2.164	0.9764	1.750	0.6821
N	7	1.179	0.4677	2.270	0.4143
Ne	10	1.792	0.4515	2.710	0.3671
Na	11	1.712	0.3923	2.850	0.3469
Ar	18	0.957	0.2165	3.500	0.2560
Kr	36	1.351	0.1872	4.418	0.1611
Xe	54	1.044	0.1107	5.101	0.1316

The Screening functions for the both the projectile (Ω_P) and the target (Ω_T) will be given by the following formulae:

$$\Omega_P(\boldsymbol{r}) = \frac{\eta_P}{\xi_P}\left(e^{r\xi_P} - 1\right) + 1 \tag{2.10}$$

And

$$\Omega_T(\boldsymbol{r}) = \frac{\eta_T}{\xi_T}\left(e^{r\xi_T} - 1\right) + 1 \tag{2.11}$$

2.2.2 Hamiltonian of the collision system

The atomic units will be used in the following equations unless stated otherwise. The Hamiltonian of the collision system is written as:

$$H = T + V_{Pe} + V_{eT} + V_{TP} \tag{2.12}$$

Where T is the total kinetic energy of the system in terms of momentum vector ($\vec{P}$) and the mass of the corresponding interacting particles. V_{Pe}, V_{eT} and V_{TP} are projectile-electron interaction, target-electron interaction, and projectile-target interaction, respectively. The kinetic energy is given by:

$$T = \frac{\boldsymbol{P}_P^2}{2m_p} + \frac{\boldsymbol{P}_T^2}{2m_T} + \frac{\boldsymbol{P}_e^2}{2m_e} \tag{2.13}$$

And V is the total potential of the system in terms of the interaction separations and the effective charge, the total potential is written as:

$$\begin{aligned} V = {} & \frac{Q_e Q_P(|\boldsymbol{r}_P - \boldsymbol{r}_e|)}{|\boldsymbol{r}_P - \boldsymbol{r}_e|} + \frac{Q_e Q_T(|\boldsymbol{r}_e - \boldsymbol{r}_T|)}{|\boldsymbol{r}_e - \boldsymbol{r}_T|} \\ & + \frac{Q_P(|\boldsymbol{r}_T - \boldsymbol{r}_P|) Q_T(|\boldsymbol{r}_T - \boldsymbol{r}_P|)}{|\boldsymbol{r}_T - \boldsymbol{r}_P|} \end{aligned} \tag{2.14}$$

Where Q_e, Q_P, and Q_T are the charge of the electron, the effective charge of the projectile, and the effective charge of the target, respectively.

The total Hamiltonian of the collision system is:

$$\begin{aligned} H = {} & \frac{\boldsymbol{P}_P^2}{2m_p} + \frac{\boldsymbol{P}_T^2}{2m_T} + \frac{\boldsymbol{P}_e^2}{2m_e} + \frac{Q_e Q_P(|\boldsymbol{r}_P - \boldsymbol{r}_e|)}{|\boldsymbol{r}_P - \boldsymbol{r}_e|} \\ & + \frac{Q_e Q_T(|\boldsymbol{r}_e - \boldsymbol{r}_T|)}{|\boldsymbol{r}_e - \boldsymbol{r}_T|} \\ & + \frac{Q_P(|\boldsymbol{r}_T - \boldsymbol{r}_P|) Q_T(|\boldsymbol{r}_T - \boldsymbol{r}_P|)}{|\boldsymbol{r}_T - \boldsymbol{r}_P|} \end{aligned} \tag{2.15}$$

The Hamilton’s equations in the phase coordinates:

$$\dot{\boldsymbol{r}}_i = \frac{\partial H}{\partial \boldsymbol{P}_i} \tag{2.16}$$

$$\dot{\boldsymbol{P}}_i = \frac{\partial H}{\partial \boldsymbol{r}_i} \tag{2.17}$$

The equations of motion in the Hamiltonian mechanics are given by:

$$
\begin{aligned}
&\dot{\boldsymbol{P}}_P \\
&= \frac{Q_e \eta_P (N_P - 1) e^{\xi_P (\boldsymbol{r}_P - \boldsymbol{r}_e)}}{|\boldsymbol{r}_P - \boldsymbol{r}_e| \big(\mathit{\Omega}_P (\boldsymbol{r}_P - \boldsymbol{r}_e)\big)^2} \\
&+ \frac{Q_e \Big\{ Z_P - \Big(1 - \mathit{\Omega}_P^{-1} (\boldsymbol{r}_P - \boldsymbol{r}_e)\Big) (N_P - 1) \Big\} (\boldsymbol{r}_P - \boldsymbol{r}_e)}{|\boldsymbol{r}_P - \boldsymbol{r}_e|^3} \\
&- \frac{\eta_P (N_P - 1) \Big\{ Z_T - \Big(1 - \mathit{\Omega}_T^{-1} (\boldsymbol{r}_T - \boldsymbol{r}_P)\Big) (N_T - 1) \Big\} e^{\xi_P (\boldsymbol{r}_T - \boldsymbol{r}_P)}}{|\boldsymbol{r}_T - \boldsymbol{r}_P| \big(\mathit{\Omega}_P (\boldsymbol{r}_T - \boldsymbol{r}_P)\big)^2} \\
&- \frac{\eta_T (N_T - 1) \Big\{ Z_P - \Big(1 - \mathit{\Omega}_P^{-1} (\boldsymbol{r}_T - \boldsymbol{r}_P)\Big) (N_P - 1) \Big\} e^{\xi_T (\boldsymbol{r}_T - \boldsymbol{r}_P)}}{|\boldsymbol{r}_T - \boldsymbol{r}_P| \big(\mathit{\Omega}_T (\boldsymbol{r}_T - \boldsymbol{r}_P)\big)^2} \\
&- \frac{1}{|\boldsymbol{r}_T - \boldsymbol{r}_P|^3} \Big\{ Z_P - \Big(1 - \mathit{\Omega}_P^{-1} (\boldsymbol{r}_T - \boldsymbol{r}_P)\Big) (N_P - 1) \Big\} \Big\{ Z_T \\
&- \Big(1 - \mathit{\Omega}_T^{-1} (\boldsymbol{r}_T - \boldsymbol{r}_P)\Big) (N_T - 1) \Big\} (\boldsymbol{r}_T - \boldsymbol{r}_P) \qquad (2.18)
\end{aligned}
$$

$$\dot{\boldsymbol{r}}_P = \frac{\boldsymbol{P}_P}{m_P} \qquad (2.19)$$

$$
\begin{aligned}
\dot{\boldsymbol{P}}_T = &- \frac{Q_e \eta_T (N_T - 1) e^{\xi_T (\boldsymbol{r}_e - \boldsymbol{r}_T)}}{|\boldsymbol{r}_e - \boldsymbol{r}_T| (\mathit{\Omega}_T (\boldsymbol{r}_e - \boldsymbol{r}_T))^2} \\
&- \frac{Q_e \{ Z_T - (1 - \mathit{\Omega}_T^{-1} (\boldsymbol{r}_e - \boldsymbol{r}_T)) (N_T - 1) \} (\boldsymbol{r}_e - \boldsymbol{r}_T)}{|\boldsymbol{r}_e - \boldsymbol{r}_T|^3} \\
&+ \frac{\eta_P (N_P - 1) \{ Z_T - (1 - \mathit{\Omega}_T^{-1} (\boldsymbol{r}_T - \boldsymbol{r}_P)) (N_T - 1) \} e^{\xi_P (\boldsymbol{r}_T - \boldsymbol{r}_P)}}{|\boldsymbol{r}_T - \boldsymbol{r}_P| (\mathit{\Omega}_P (\boldsymbol{r}_T - \boldsymbol{r}_P))^2} \\
&+ \frac{\eta_T (N_T - 1) \{ Z_P - (1 - \mathit{\Omega}_P^{-1} (\boldsymbol{r}_T - \boldsymbol{r}_P)) (N_P - 1) \} e^{\xi_T (\boldsymbol{r}_T - \boldsymbol{r}_P)}}{|\boldsymbol{r}_T - \boldsymbol{r}_P| (\mathit{\Omega}_T (\boldsymbol{r}_T - \boldsymbol{r}_P))^2} \\
&+ \frac{1}{|\boldsymbol{r}_T - \boldsymbol{r}_P|^3} \{ Z_P - (1 - \mathit{\Omega}_P^{-1} (\boldsymbol{r}_T - \boldsymbol{r}_P)) (N_P - 1) \} \{ Z_T \\
&- (1 - \mathit{\Omega}_T^{-1} (\boldsymbol{r}_T - \boldsymbol{r}_P)) (N_T - 1) \} (\boldsymbol{r}_T - \boldsymbol{r}_P) 2.20)
\end{aligned}
$$

$$\dot{\boldsymbol{r}}_T = \frac{\boldsymbol{P}_T}{m_T} \tag{2.21}$$

$$\begin{aligned}\dot{\boldsymbol{P}}_e = &-\frac{Q_e \eta_P (N_P - 1) e^{\xi_P (\boldsymbol{r}_P - \boldsymbol{r}_e)}}{|\boldsymbol{r}_P - \boldsymbol{r}_e| \big(\Omega_P(\boldsymbol{r}_P - \boldsymbol{r}_e)\big)^2} + \frac{Q_e \eta_T (N_T - 1) e^{\xi_T (\boldsymbol{r}_e - \boldsymbol{r}_T)}}{|\boldsymbol{r}_e - \boldsymbol{r}_T| \big(\Omega_T(\boldsymbol{r}_e - \boldsymbol{r}_T)\big)^2} \\ &- \frac{Q_e \left\{ Z_P - \left(1 - \Omega_P^{-1}(\boldsymbol{r}_P - \boldsymbol{r}_e)\right)(N_P - 1)\right\} (\boldsymbol{r}_P - \boldsymbol{r}_e)}{|\boldsymbol{r}_P - \boldsymbol{r}_e|^3} \\ &+ \frac{Q_e \left\{ Z_T - \left(1 - \Omega_T^{-1}(\boldsymbol{r}_e - \boldsymbol{r}_T)\right)(N_T - 1)\right\} (\boldsymbol{r}_e - \boldsymbol{r}_T)}{|\boldsymbol{r}_e - \boldsymbol{r}_T|^3}\end{aligned} \tag{2.22}$$

$$\dot{\boldsymbol{r}}_e = \frac{\boldsymbol{P}_e}{m_e} \tag{2.23}$$

We can clearly see that:

$$\ddot{\boldsymbol{r}}_P = \frac{\dot{\boldsymbol{P}}_P}{m_P} \tag{2.24}$$

$$\ddot{\boldsymbol{r}}_T = \frac{\dot{\boldsymbol{P}}_T}{m_T} \tag{2.25}$$

$$\ddot{\boldsymbol{r}}_e = \frac{\dot{\boldsymbol{P}}_e}{m_e} \tag{2.26}$$

Hence the equations of motion will be written as:

$$\begin{aligned}
m_P\ddot{\boldsymbol{r}}_P = {} & \frac{Q_e\eta_P(N_P-1)e^{\xi_P(\boldsymbol{r}_P-\boldsymbol{r}_e)}}{|\boldsymbol{r}_P-\boldsymbol{r}_e|\big(\Omega_P(\boldsymbol{r}_P-\boldsymbol{r}_e)\big)^2} \\
& + \frac{Q_e\left\{Z_P-\left(1-\Omega_P^{-1}(\boldsymbol{r}_P-\boldsymbol{r}_e)\right)(N_P-1)\right\}(\boldsymbol{r}_P-\boldsymbol{r}_e)}{|\boldsymbol{r}_P-\boldsymbol{r}_e|^3} \\
& - \frac{\eta_P(N_P-1)\left\{Z_T-\left(1-\Omega_T^{-1}(\boldsymbol{r}_T-\boldsymbol{r}_P)\right)(N_T-1)\right\}e^{\xi_P(\boldsymbol{r}_T-\boldsymbol{r}_P)}}{|\boldsymbol{r}_T-\boldsymbol{r}_P|\big(\Omega_P(\boldsymbol{r}_T-\boldsymbol{r}_P)\big)^2} \\
& - \frac{\eta_T(N_T-1)\left\{Z_P-\left(1-\Omega_P^{-1}(\boldsymbol{r}_T-\boldsymbol{r}_P)\right)(N_P-1)\right\}e^{\xi_T(\boldsymbol{r}_T-\boldsymbol{r}_P)}}{|\boldsymbol{r}_T-\boldsymbol{r}_P|\big(\Omega_T(\boldsymbol{r}_T-\boldsymbol{r}_P)\big)^2} \\
& - \frac{1}{|\boldsymbol{r}_T-\boldsymbol{r}_P|^3}\left\{Z_P-\left(1-\Omega_P^{-1}(\boldsymbol{r}_T-\boldsymbol{r}_P)\right)(N_P-1)\right\}\Big\{Z_T \\
& - \left(1-\Omega_T^{-1}(\boldsymbol{r}_T-\boldsymbol{r}_P)\right)(N_T-1)\Big\}(\boldsymbol{r}_T-\boldsymbol{r}_P) \qquad (2.27)
\end{aligned}$$

$$\begin{aligned}
m_T\ddot{\boldsymbol{r}}_T = {} & -\frac{Q_e\eta_T(N_T-1)e^{\xi_T(\boldsymbol{r}_e-\boldsymbol{r}_T)}}{|\boldsymbol{r}_e-\boldsymbol{r}_T|\big(\Omega_T(\boldsymbol{r}_e-\boldsymbol{r}_T)\big)^2} \\
& - \frac{Q_e\left\{Z_T-\left(1-\Omega_T^{-1}(\boldsymbol{r}_e-\boldsymbol{r}_T)\right)(N_T-1)\right\}(\boldsymbol{r}_e-\boldsymbol{r}_T)}{|\boldsymbol{r}_e-\boldsymbol{r}_T|^3} \\
& + \frac{\eta_P(N_P-1)\left\{Z_T-\left(1-\Omega_T^{-1}(\boldsymbol{r}_T-\boldsymbol{r}_P)\right)(N_T-1)\right\}e^{\xi_P(\boldsymbol{r}_T-\boldsymbol{r}_P)}}{|\boldsymbol{r}_T-\boldsymbol{r}_P|\big(\Omega_P(\boldsymbol{r}_T-\boldsymbol{r}_P)\big)^2} \\
& + \frac{\eta_T(N_T-1)\left\{Z_P-\left(1-\Omega_P^{-1}(\boldsymbol{r}_T-\boldsymbol{r}_P)\right)(N_P-1)\right\}e^{\xi_T(\boldsymbol{r}_T-\boldsymbol{r}_P)}}{|\boldsymbol{r}_T-\boldsymbol{r}_P|\big(\Omega_T(\boldsymbol{r}_T-\boldsymbol{r}_P)\big)^2} \\
& + \frac{1}{|\boldsymbol{r}_T-\boldsymbol{r}_P|^3}\left\{Z_P-\left(1-\Omega_P^{-1}(\boldsymbol{r}_T-\boldsymbol{r}_P)\right)(N_P-1)\right\}\Big\{Z_T \\
& - \left(1-\Omega_T^{-1}(\boldsymbol{r}_T-\boldsymbol{r}_P)\right)(N_T-1)\Big\}(\boldsymbol{r}_T-\boldsymbol{r}_P) \qquad (2.28)
\end{aligned}$$

$$
\begin{aligned}
m_e\ddot{\boldsymbol{r}}_e = & -\frac{Q_e\eta_P(N_P-1)e^{\xi_P(\boldsymbol{r}_P-\boldsymbol{r}_e)}}{|\boldsymbol{r}_P-\boldsymbol{r}_e|\big(\Omega_P(\boldsymbol{r}_P-\boldsymbol{r}_e)\big)^2}+\frac{Q_e\eta_T(N_T-1)e^{\xi_T(\boldsymbol{r}_e-\boldsymbol{r}_T)}}{|\boldsymbol{r}_e-\boldsymbol{r}_T|\big(\Omega_T(\boldsymbol{r}_e-\boldsymbol{r}_T)\big)^2} \\
& -\frac{Q_e\left\{Z_P-\left(1-\Omega_P^{-1}(\boldsymbol{r}_P-\boldsymbol{r}_e)\right)(N_P-1)\right\}(\boldsymbol{r}_P-\boldsymbol{r}_e)}{|\boldsymbol{r}_P-\boldsymbol{r}_e|^3} \\
& +\frac{Q_e\left\{Z_T-\left(1-\Omega_T^{-1}(\boldsymbol{r}_e-\boldsymbol{r}_T)\right)(N_T-1)\right\}(\boldsymbol{r}_e-\boldsymbol{r}_T)}{|\boldsymbol{r}_e-\boldsymbol{r}_T|^3}\,(2.29)
\end{aligned}
$$

Recalling that $\boldsymbol{A}=\boldsymbol{r}_e-\boldsymbol{r}_T,\ \boldsymbol{B}=\boldsymbol{r}_P-\boldsymbol{r}_e,\ \boldsymbol{C}=\boldsymbol{r}_T-\boldsymbol{r}_P$ and $\boldsymbol{A}+\boldsymbol{B}+\boldsymbol{C}=0$, equations (2.27-2.29) can be written as:

$$
\begin{aligned}
& \ddot{\boldsymbol{A}} \\
& =\frac{Q_e}{A^2}\left(\frac{1}{m_e}+\frac{1}{m_T}\right)\left[\frac{\eta_T(N_T-1)e^{\xi_T(A)}}{(\Omega_T(A))^2}+\frac{\{Z_T-(1-\Omega_T^{-1}(A))(N_T-1)\}}{A}\right]\boldsymbol{A} \\
& -\frac{Q_e}{m_eB^2}\left[\frac{\eta_P(N_P-1)e^{\xi_P(B)}}{\big(\Omega_P(B)\big)^2}+\frac{\left\{Z_P-\left(1-\Omega_P^{-1}(B)\right)(N_P-1)\right\}}{B}\right]\boldsymbol{B} \\
& -\frac{1}{m_TC^2}\left[\frac{\eta_P(N_P-1)\left\{Z_T-\left(1-\Omega_T^{-1}(C)\right)(N_T-1)\right\}e^{\xi_P(C)}}{\big(\Omega_P(C)\big)^2}\right. \\
& +\frac{\eta_T(N_T-1)\left\{Z_P-\left(1-\Omega_P^{-1}(C)\right)(N_P-1)\right\}e^{\xi_T(C)}}{\big(\Omega_T(C)\big)^2} \\
& \left.+\frac{\left\{Z_P-\left(1-\Omega_P^{-1}(C)\right)(N_P-1)\right\}\left\{Z_T-\left(1-\Omega_T^{-1}(C)\right)(N_T-1)\right\}}{C}\right]\boldsymbol{C}2.30)
\end{aligned}
$$

$$\begin{aligned}
&\ddot{\boldsymbol{B}}\\
&= -\frac{Q_e}{m_e A^2}\left[\frac{\eta_T(N_T-1)e^{\xi_T(A)}}{\left(\Omega_T(A)\right)^2} + \frac{\left\{Z_T - \left(1-\Omega_T^{-1}(A)\right)(N_T-1)\right\}}{A}\right]\boldsymbol{A}\\
&+ \frac{Q_e}{B^2}\left(\frac{1}{m_P}+\frac{1}{m_e}\right)\left[\frac{\eta_P(N_P-1)e^{\xi_P(B)}}{\left(\Omega_P(B)\right)^2} + \frac{\left\{Z_P - \left(1-\Omega_P^{-1}(B)\right)(N_P-1)\right\}}{B}\right]\boldsymbol{B}\\
&- \frac{1}{m_P C^2}\left[\frac{\eta_P(N_P-1)\left\{Z_T - \left(1-\Omega_T^{-1}(C)\right)(N_T-1)\right\}e^{\xi_P(C)}}{\left(\Omega_P(C)\right)^2}\right.\\
&+ \frac{\eta_T(N_T-1)\left\{Z_P - \left(1-\Omega_P^{-1}(C)\right)(N_P-1)\right\}e^{\xi_T(C)}}{\left(\Omega_T(C)\right)^2}\\
&\left.+ \frac{\left\{Z_P - \left(1-\Omega_P^{-1}(C)\right)(N_P-1)\right\}\left\{Z_T - \left(1-\Omega_T^{-1}(C)\right)(N_T-1)\right\}}{C}\right]\boldsymbol{C}
\end{aligned}\tag{2.31}$$

$$\begin{aligned}
&\ddot{\boldsymbol{C}}\\
&= -\frac{Q_e}{m_T A^2}\left[\frac{\eta_T(N_T-1)e^{\xi_T(A)}}{\left(\Omega_T(A)\right)^2} + \frac{\left\{Z_T - \left(1-\Omega_T^{-1}(A)\right)(N_T-1)\right\}}{A}\right]\boldsymbol{A}\\
&- \frac{Q_e}{m_P B^2}\left[\frac{\eta_P(N_P-1)e^{\xi_P(B)}}{\left(\Omega_P(B)\right)^2} + \frac{\left\{Z_P - \left(1-\Omega_P^{-1}(B)\right)(N_P-1)\right\}}{B}\right]\boldsymbol{B}\\
&+ \frac{1}{C^2}\left(\frac{1}{m_T}+\frac{1}{m_P}\right)\left[\frac{\eta_P(N_P-1)\left\{Z_T - \left(1-\Omega_T^{-1}(C)\right)(N_T-1)\right\}e^{\xi_P(C)}}{\left(\Omega_P(C)\right)^2}\right.\\
&+ \frac{\eta_T(N_T-1)\left\{Z_P - \left(1-\Omega_P^{-1}(C)\right)(N_P-1)\right\}e^{\xi_T(C)}}{\left(\Omega_T(C)\right)^2}\\
&\left.+ \frac{\left\{Z_P - \left(1-\Omega_P^{-1}(C)\right)(N_P-1)\right\}\left\{Z_T - \left(1-\Omega_T^{-1}(C)\right)(N_T-1)\right\}}{C}\right]\boldsymbol{C}
\end{aligned}\tag{2.32}$$

To write equations (2.30-2.32) in more compact form, the following functions are used:

$$f_i(r) = Z_i - \left(1 - \Omega_i^{-1}(r)\right)(N_i - 1) \tag{2.33}$$

$$g_i(r) = \eta_i (N_i - 1) e^{\xi_i(r)} \tag{2.34}$$

Equations (2.30-2.32) in the compact form will be:

$$\begin{aligned}\ddot{\boldsymbol{A}} = {} & \frac{Q_e}{A^2}\left(\frac{1}{m_e} + \frac{1}{m_T}\right)\left[\frac{g_T(A)}{\left(\Omega_T(A)\right)^2} + \frac{f_T(A)}{A}\right]\boldsymbol{A} \\ & - \frac{Q_e}{m_e B^2}\left[\frac{g_P(B)}{\left(\Omega_P(B)\right)^2} + \frac{f_P(B)}{B}\right]\boldsymbol{B} \\ & - \frac{1}{m_T C^2}\left[\frac{g_P(C) f_T(C)}{\left(\Omega_P(C)\right)^2} + \frac{g_T(C) f_P(C)}{\left(\Omega_T(C)\right)^2}\right. \\ & \left. + \frac{f_p(C) f_T(C)}{C}\right]\boldsymbol{C}\end{aligned} \tag{2.35}$$

$$\begin{aligned}\ddot{\boldsymbol{B}} = {} & -\frac{Q_e}{m_e A^2}\left[\frac{g_T(A)}{\left(\Omega_T(A)\right)^2} + \frac{f_T(A)}{A}\right]\boldsymbol{A} \\ & + \frac{Q_e}{B^2}\left(\frac{1}{m_P} + \frac{1}{m_e}\right)\left[\frac{g_P(B)}{\left(\Omega_P(B)\right)^2} + \frac{f_P(B)}{B}\right]\boldsymbol{B} \\ & - \frac{1}{m_P C^2}\left[\frac{g_P(C) f_T(C)}{\left(\Omega_P(C)\right)^2} + \frac{g_T(C) f_P(C)}{\left(\Omega_T(C)\right)^2}\right. \\ & \left. + \frac{f_p(C) f_T(C)}{C}\right]\boldsymbol{C}\end{aligned} \tag{2.36}$$

$$\ddot{\boldsymbol{C}} = -\frac{Q_e}{m_T A^2}\left[\frac{g_T(A)}{\left(\Omega_T(A)\right)^2} + \frac{f_T(A)}{A}\right]\boldsymbol{A} - \frac{Q_e}{m_P B^2}\left[\frac{g_P(B)}{\left(\Omega_P(B)\right)^2} + \frac{f_P(B)}{B}\right]\boldsymbol{B} + \frac{1}{C^2}\left(\frac{1}{m_T} + \frac{1}{m_P}\right)\left[\frac{g_P(C)f_T(C)}{\left(\Omega_P(C)\right)^2} + \frac{g_T(C)f_P(C)}{\left(\Omega_T(C)\right)^2} + \frac{f_p(C)f_T(C)}{C}\right]\boldsymbol{C} \qquad (2.37)$$

Using $\boldsymbol{A} + \boldsymbol{B} + \boldsymbol{C} = 0$ to write equations (2.35 and 2.36) are reduced to:

$$\ddot{\boldsymbol{A}} = \left\{\frac{Q_e}{A^2}\left(\frac{1}{m_e} + \frac{1}{m_T}\right)\left[\frac{g_T(A)}{\left(\Omega_T(A)\right)^2} + \frac{f_T(A)}{A}\right] + \frac{1}{m_T C^2}\left[\frac{g_P(C)f_T(C)}{\left(\Omega_P(C)\right)^2} + \frac{g_T(C)f_P(C)}{\left(\Omega_T(C)\right)^2} + \frac{f_p(C)f_T(C)}{C}\right]\right\}\boldsymbol{A} + \left\{\frac{1}{m_T C^2}\left[\frac{g_P(C)f_T(C)}{\left(\Omega_P(C)\right)^2} + \frac{g_T(C)f_P(C)}{\left(\Omega_T(C)\right)^2} + \frac{f_p(C)f_T(C)}{C}\right] - \frac{Q_e}{m_e B^2}\left[\frac{g_P(B)}{\left(\Omega_P(B)\right)^2} + \frac{f_P(B)}{B}\right]\right\}\boldsymbol{B} \qquad (2.38)$$

$$\ddot{\boldsymbol{B}} = \left\{\frac{1}{m_P C^2}\left[\frac{g_P(C)f_T(C)}{\left(\Omega_P(C)\right)^2} + \frac{g_T(C)f_P(C)}{\left(\Omega_T(C)\right)^2} + \frac{f_p(C)f_T(C)}{C}\right] - \frac{Q_e}{m_e A^2}\left[\frac{g_T(A)}{\left(\Omega_T(A)\right)^2} + \frac{f_T(A)}{A}\right]\right\}\boldsymbol{A} + \left\{\frac{Q_e}{B^2}\left(\frac{1}{m_P} + \frac{1}{m_e}\right)\left[\frac{g_P(B)}{\left(\Omega_P(B)\right)^2} + \frac{f_P(B)}{B}\right] + \frac{1}{m_P C^2}\left[\frac{g_P(C)f_T(C)}{\left(\Omega_P(C)\right)^2} + \frac{g_T(C)f_P(C)}{\left(\Omega_T(C)\right)^2} + \frac{f_p(C)f_T(C)}{C}\right]\right\}\boldsymbol{B} \qquad (2.38)$$

The standard Runge-Kutta method was employed to numerically solve the differential equations (2.38-2.39) with time as the independent variable. The Solution of the differential equations was performed using a specified set of initial conditions, these initial conditions are discussed in the next sub-section.

2.2.3 Initial conditions of the projectile

Our coordinate system is established in the laboratory frame, with the centre-of-mass of the target atom serving as the point of origin. At the initial time, $t = 0$, we define the projectile's initial conditions in terms of its initial distance, R_o, from the center of mass of the target, its velocity (v_P), and the impact parameter (b). See Figure 2.3.

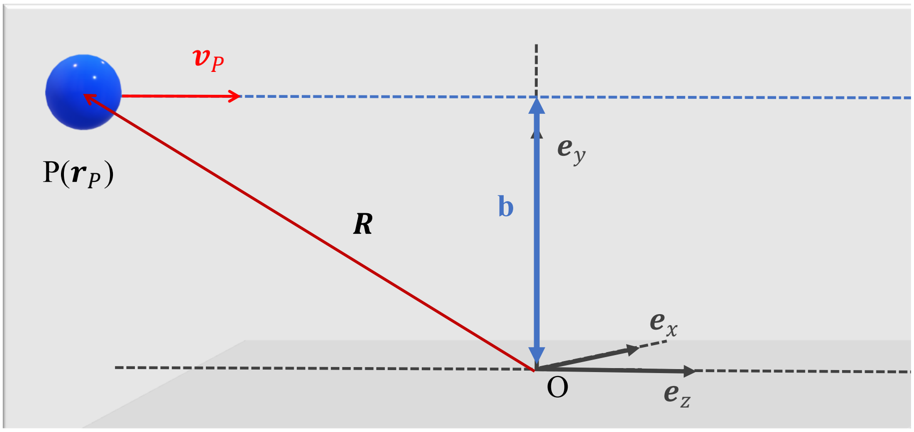

Figure 2.3 Initial conditions for the collision system.

The value of projectiles velocity (v_P) is fixed, and we take the projectile to be moving initially in an approximately straight line along the z-axis. To ensure minimal interaction with the target, we set R_o to a sufficiently large value where the projectile-electron interaction is significantly smaller than the target-electron interaction, and our results should remain independent of the specific choice of R_o. Additionally, we select the impact parameter within the range $[0, b_{max}^2]$ to maintain a uniform flux of incident particles, where b_{max} represents the threshold above which ionization and capture processes become insignificant. The initial relative motion is represented by the following conditions:

$$\boldsymbol{R}_o = \begin{pmatrix} 0 \\ b \\ -\sqrt{R_0^2 - b^2} \end{pmatrix} \tag{2.39}$$

$$v = \begin{pmatrix} 0 \\ 0 \\ v_P \end{pmatrix} \tag{2.41}$$

2.2.4 Initial conditions of the active electron

the determination of the initial electronic state of the target atom is achieved by extracting information from the microcanonical distribution. The process of selecting these initial states closely adheres to a methodology by Reinhold and Falcon's, originally designed for non-Coulombic systems as outlined in reference [83]. Within this framework, the microcanonical ensemble serves as the defining parameter for establishing the initial state of the target atom, with specific emphasis on imposing constraints pertaining to the initial binding energy associated with the designated electron shell.

$$\rho_{E_0}(\boldsymbol{A}, \dot{\boldsymbol{A}}) = k\delta\left(E_0 - \frac{1}{2}\mu_{Te}\dot{\boldsymbol{A}}^2 - V_{eT}(A)\right) \tag{2.42}$$

where k, E_o and μ_{T_e} are a normalization constant, the ionization energy of the active electron, and the reduced mass of particles target core (T) and the active electron (e), respectively. $V(A)$ is the model potential of the electron and target-core, where $A = |\boldsymbol{r}_e - \boldsymbol{r}_T|$. based on equation (2.39), the electronic coordinate is confined to the intervals where the following relation is verified:

$$\frac{1}{2}\mu_{Te}\dot{\boldsymbol{A}}^2 = \frac{\boldsymbol{P}^2}{2\mu_{Te}} = E_0 - V(A) > 0 \tag{2.43}$$

It is difficult to find the roots of the inequality in equation (2.40), to make calculations simpler, we can rewrite equation (2.40) to have only one root, which is A_o, equation (2.40) becomes:

$$E_0 - V(A) = 0 \tag{2.44}$$

Hence, the values of A are limited between 0 and A_o. Potentials that meet this criterion depict the interaction between the active electron and the target core.

To establish an initial state for the active electron, we need to transform the variables $(\boldsymbol{A}, \boldsymbol{P})$ into a set of uniformly distributed variables that fully describe the system's initial condition as defined in equation (2.39). This transformation involves two consecutive changes of coordinates, which are detailed as follows. The first transformation:

$$(\boldsymbol{A}, \boldsymbol{P}) \rightarrow (E, A, v_A, v_P, \varphi_A, \varphi_P) \tag{2.45}$$

The parameters in equation (2.42) are defined by the following relations:

$$\boldsymbol{A} = \begin{pmatrix} x \\ y \\ z \end{pmatrix} = \begin{pmatrix} A(1 - v_A^2)^{1/2} \, cos\, \varphi_A \\ A(1 - v_A^2)^{1/2} \, sin\, \varphi_A \\ z = Av_A \end{pmatrix} \tag{2.46}$$

$$\dot{\boldsymbol{A}} = \frac{1}{\mu_{Te}}\begin{pmatrix} P_x \\ P_y \\ P_z \end{pmatrix} = \frac{1}{\mu_{Te}}\begin{pmatrix} \{2\mu_{Te}[E - V(A)]\}^{1/2}(1 - v_P^2)^{1/2}\, cos\, \varphi_A \\ \{2\mu_{Te}[E - V(A)]\}^{1/2}(1 - v_P^2)^{1/2}\, sin\, \varphi_A \\ \{2\mu_{Te}[E - V(A)]\}^{1/2} \end{pmatrix} \quad (2.47)$$

The previous parameters in equations (2.43) and (2.44) are restricted by the intervals:

$$\begin{aligned} &E \in (-\infty, 0), \qquad A \in [0, A_o], \\ &v_A, v_P \in [-1,1], \qquad \varphi_A, \varphi_P \in [0,2\pi] \end{aligned} \quad (2.40)$$

The first transformation has the Jacobian:

$$J_1 = \mu_{Te}A^2\{2\mu_{Te}[E - V(A)]\}^{1/2} \quad (2.49)$$

For on the new parameters, we introduce the corresponding initial distribution:

$$k\mu_{Te}A^2\{2\mu_{Te}[E_0 - V(A)]\}^{1/2}(E - E_0) \quad (2.50)$$

For the second transformation, A is transformed to ω by using the relation:

$$\omega(A) = \int_0^A dA'\, \mu_{Te}A'^2\{2\mu_{Te}[E_0 - V(A')]\}^{1/2} \quad (2.51)$$

The interval of the variable ω depending on the intervals of A:

$$0 < \omega < \omega(A_o) \quad (2.52)$$

The new Jacobian of the second transformation is given by:

$$J_2 = \frac{dA}{d\omega} = \mu_{Te}^{-1}A^{-2}\{2\mu_{Te}[E_0 - V(A)]\}^{1/2} \quad (2.53)$$

Finally, we get the desired distribution which is independent of the parameters $(\omega, v_A, v_P, \varphi_A, \varphi_P)$:

$$f(E, \omega, v_A, v_P, \varphi_A, \varphi_P) = k\delta(E - E_0) \tag{2.54}$$

Based on this distribution, we can produce the initial conditions of the active electrons, the new parameters are selected randomly in the intervals:

$$\omega \in \big(0, \omega(A_o)\big), \qquad v_A, v_P \in [-1,1], \qquad \varphi_A, \varphi_P \in [0,2\pi] \tag{2.55}$$

Hence, equations (2.43), (2.44) and (2.48) are used to obtain the initial conditions of **A** and **p**. In the initial stages of the CTMC calculations, for practical reasons, we start by tabulating the values of **A** and their corresponding numerical computations of ω, which are derived from equation (2.48). While conducting the Monte Carlo simulations, we use interpolation to select specific values of **A** from this table. Three-dimensional CTMC calculations of three-body system are performed for a specified set of initial conditions.

Table 2.2 Binding energies (eV)

	He	N	Ne	Ar	Kr	Xe
1s	24. 58	409.9				
2s		37.3	48.5			
2p		14. 54	21.6	248.4		
3s				29.3		
3p				15.7		
3d					93.8	676.4
4s					27.5	213.2
4p					14.1	145.5
4d						67.5
5s						23.3
5p						12.1

Table 2.2 shows the binding energies of different shells of the targets under investigation.

2.3 Cross sections

We employed the CTMC calculation method [84] to investigate the dynamics of a system characterized by model potential. To efficiently utilize computational resources, we integrate the equations of motion over a span of 10^5 atomic units (a.u.) to save computer time [85]. Our integration procedure is conducted in two steps: firstly, we integrate up to the point of observing ionisation, excitation, and charge transfer processes. Subsequently, we continue the integration solely for the ionisation channel. Within this context, we record the final energy and the scattering polar (θ) and azimuthal (ϕ) angles of both the projectile and the ionised electron associated with the ionisation channel. Furthermore, these parameters are computed at a substantial distance between the projectile and the target-core, ensuring comprehensive analysis of the system's behaviour.

The total, single and double differential cross-sections are evaluated using the following formulae,

$$\sigma = \frac{2\pi b_{max}}{N_{tot}} \sum_{i=1}^{N_t} b_i \tag{2.56}$$

$$\frac{d\sigma}{dE} = \frac{2\pi b_{max}}{N_{tot} \Delta E} \sum_{i=1}^{N_t} b_i \tag{2.57}$$

$$\frac{d\sigma}{d\Omega} = \frac{2\pi b_{max}}{N_{tot} \Delta\Omega} \sum_{i=1}^{N_t} b_i \tag{2.58}$$

$$\frac{d^2\sigma}{d\Omega dE} = \frac{2\pi b_{max}}{N_{tot}\Delta\Omega\Delta E}\sum_{i=1}^{N_t} b_i \tag{2.59}$$

where N_{tot} represents the cumulative count of trajectories computed for impact parameters smaller than $b_{\max}$. N_t the number of trajectories achieved the requested electron process. b_i denotes the effective impact parameter associated with the electronic process for the respective trajectory. For ionisation process, ionised electrons can be grouped using an energy interval (ΔE) and an emission angle interval ($\Delta\Omega$).

For a certain electron process, the standard deviation of total cross section is given by:

$$\Delta\sigma = \sigma\left(\frac{N_{tot}-N_t}{N_{tot}N_t}\right)^{1/2} \tag{2.60}$$

2.4 Exit channels of the collision system

In the vicinity of an atom, colliding particles engage in intricate interactions, resulting in a variety of collision products. These products can be broadly categorized into four distinct channels. The first channel encompasses ionization processes. Within this category, we have target ionization, where a target atom gains a positive charge through the loss of electrons, and projectile ionization, where a projectile particle undergoes a similar process of acquiring a positive charge through electron loss. Additionally, there exists a more complex scenario known as projectile and target ionization, wherein both the projectile and the target atoms acquire positive charges through electron loss, with all constituent particles, including the projectile-core, target-core, projectile's electron, and target's electron, independently dissociating after the collision.

Moving on to the second channel, it encompasses scattering process. This channel involves direct scattering, wherein the colliding particles interact in such a way that a single particle remains bound, accounting for elastic and excitation states post-collision.

The third channel pertains to electron capture processes. This channel encompasses capture to projectile, where a projectile particle acquires a negative charge through the acquisition of electrons. In this process, the active electron of the target is captured by the projectile, and the target-core moves independently following the collision. Similarly, there is capture to target, where a target atom's core gains a negative charge through electron capture. In this case, the active electron of the projectile is captured by the target, and the projectile-core moves independently after the collision.

Lastly, the fourth channel combines simultaneous ionization and capture processes. Within this category, we find target ionization and capture to projectile, wherein a target atom gains a positive charge through electron loss while simultaneously capturing the projectile's electron. Conversely, there is projectile ionization and capture to target, where a projectile particle gains a positive charge through electron loss while simultaneously capturing the target's electron. These intricate interactions and diverse channels of collision products play a significant role in understanding the behaviour of particles as they approach atoms.

In this thesis, as the main focus is a three-body collision system, i.e., projectile (P), target-core (T) and the active electron of the target, hence, the exit channels are considered for single electron processes only.

Chapter 3 Results and Discussion

3.1 Pre-calculations tests

In this section, some remarks regarding calculating the cross section using the model potential previously discussed using CTMC method are presented.

3.1.1 The role of nuclear-nuclear interaction on the cross section

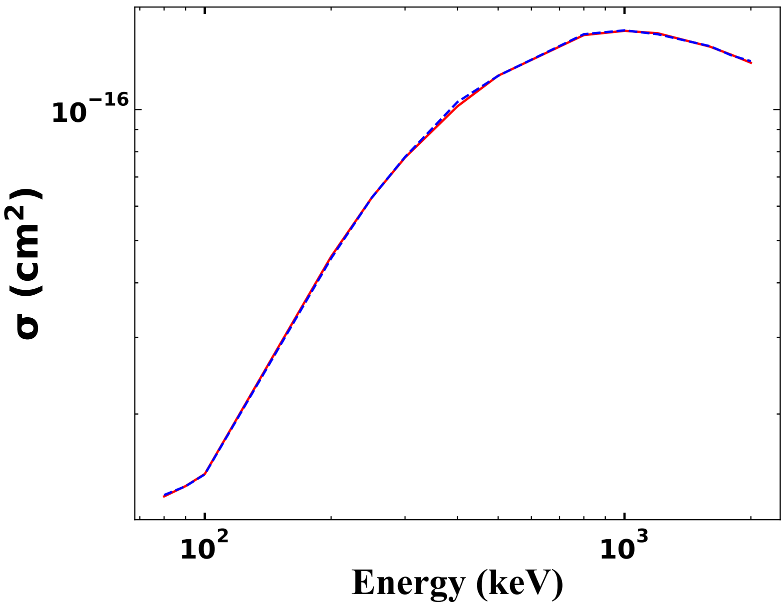

Figure 3.1 Total ionisation cross section in the interaction of singly charge lithium with helium atom. Red solid line: nucleus-nucleus interaction is on, blue dashed line: nucleus-nucleus interaction is off.

In the three body system, as discussed previously, the total potential includes the projectile-target interaction V_{TP}, which is also referred to as the nuclear-nuclear interaction. According to Belkic et. al. [86], the total cross section of heavy particles ($1/\mathrm{M}_{(\mathrm{P,T})} \ll 1$) should be independent of the nuclear-nuclear interaction. In order to confirm this remark, the total ionisation cross section (σ) was calculated for the collision system of singly charged lithium (Li^{+}) with helium (He) in the energy range ($80 - 2000\ keV$), the cross section was calculated with σ_{on} and without σ_{off} including the nuclear-nuclear potential (V_{TP}). Figure 3.1 shows our calculations, it is clearly seen that in our model, there is insignificant difference between the two cross sections σ_{on} and σ_{off}.

3.1.2 Contribution of the inner shells into the total cross section

In the collision system of protons with xenon ($H^{+} - Xe$), the total cross sections (TCS) for 3d, 4s, 4p, 4d, 5s and 5p shells are calculated, then the overall TCS of Xe would be the sum of cross sections of all shells, see figure 3.2. The peak of the overall TCS (red curve in figure 3.2) is at impact energy around 50 keV, which the same peak of the TCS of the 5p shell. For impact energies below 50 keV, the overall TCS is roughly equal to the TCS of the 5p shell. However, for impact energies above 50 keV, the remaining inner shells start to slightly contribute to the overall cross section, especially 4d and 5s shells. Moreover, at high impact energies, the contribution of the inner shells to the overall TCS becomes significant. A noteworthy point to mention is that the TCS of 5s is significantly larger than that of the 4d shell at low impact energies, however, at large impact energies, the TCS of 4d shell becomes larger than the TCS of 5s shell. Another point to mention is that the peak positions of individual shells shift to the right for lower shells.

Based on these results, the results of total cross section (TCS) for all collision systems in this thesis will include the TCS of inner shells. However, since the focus of the thesis for the single (SDCS) and double

(DDCS) differential cross sections is in the range of $30 - 60\ keV$ (green shaded area in figure 3.2), it would be a good approximation to consider only the outermost shell for each target.

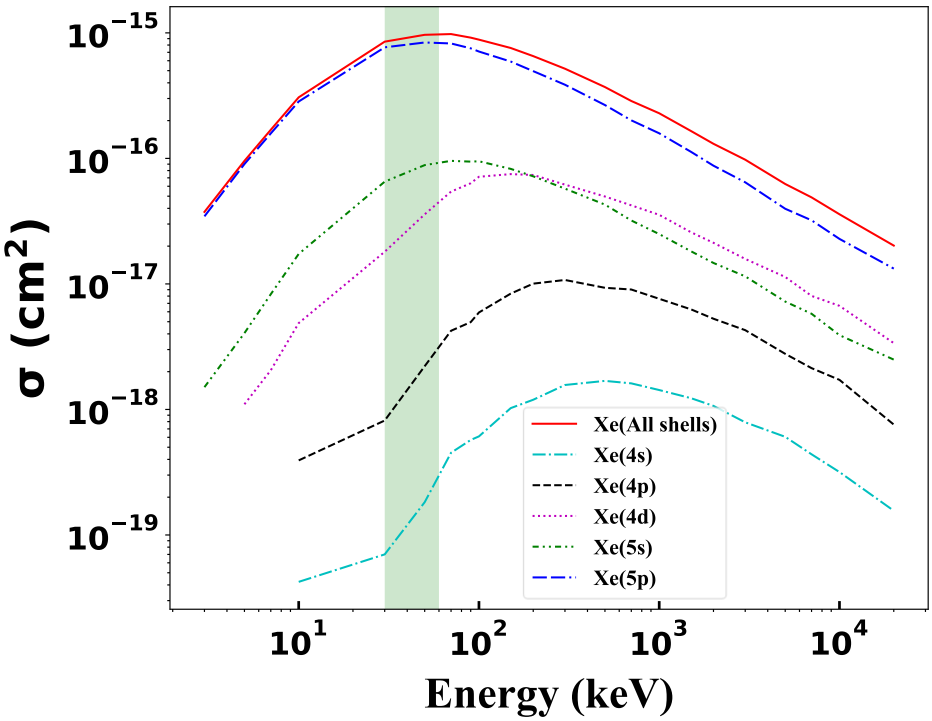

Figure 3.2 Total cross section of ionisation channel of the collision $H^+ - Xe$ for 3d, 4s, 4p, 4d, 5s and 5p shells. Model potential CTMC results; cyan dashed-dotted line: 4s, black dashed lined: 4p, magenta dotted line: 4d, green dashed-dotted-dotted line: 5s, blue dashed-dashed-dotted line: 5p. Red solid line is the sum of the sub-shells of Xe.

3.1.3 Probabilities of electronic processes as function of impact parameters

Analysing the probabilities of electronic processes (i.e., ionisation and electron capture) is important to appropriately determine the maximum impact parameters (b). The probability multiplied by the impact parameter for electron capture (figure 3.3) and ionisation (figure 3.4) channels are plotted as a function of impact parameter. After fitting the results, the probabilities have shape of almost gaussian. The chosen impact energies are, 10, 50, 100, 400, 1000, 2000 keV.

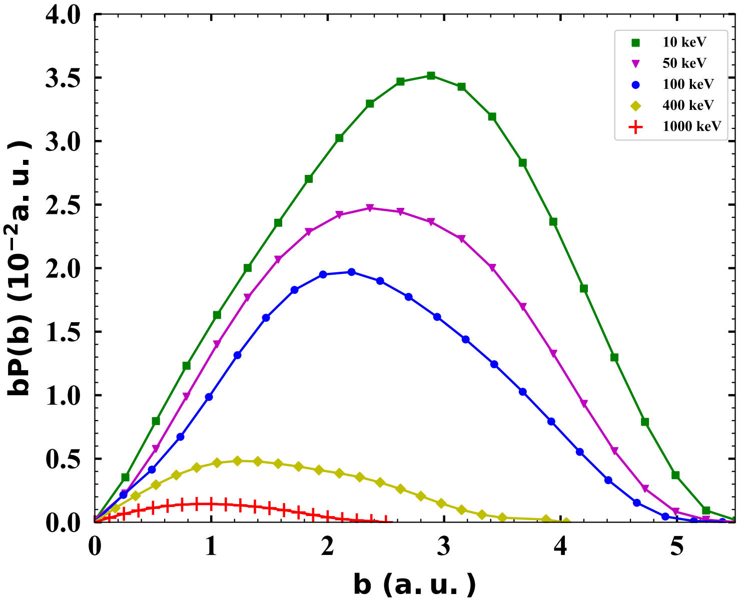

Figure 3.3 Probability $[bP(b))]$ of the electron capture from in the collision system $\mathrm{Li}^+ - \mathrm{N(2p)}$ versus the impact parameter for many impact energies. Green squares: 10 keV, magenta triangles: 50 keV, blue circles: 100 keV, yellow diamonds: 400 keV and red plus: 1000 keV. The solid lines represent the fit of the probability.

For the electron capture case, figure 3.3, we can see that the maximum probability is for the lowest impact energy, and by increasing the impact energy, the probability decreases, and the peaks shift to the left. The peaks shift indicates that the maximum impact parameter decreases for higher impact energies.

For the ionisation case, figure 3.4, we can see that the probability starts low for impact energy of 10 keV, then the probability increases reaching maximum value at impact energy of 400 keV. For impact energies larger than 400 keV, the probability starts to decrease. The peaks for the higher probabilities are shifted to right, while the peaks for the lower probabilities are shifted to left.

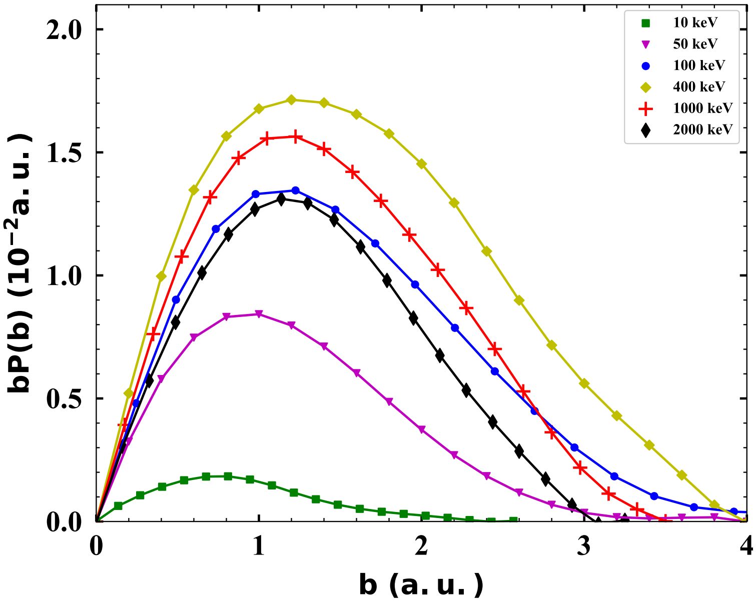

Figure 3.4 Same as figure 3.3 but for the ionisation from in the collision system $\mathrm{Li}^{+} - \mathrm{N(2p)}$. Here black diamond: 2000 keV.

3.2 Total cross sections of single electron capture and ionisation from He(1s) by Li^+

The total cross sections (TCS) of electron capture (figure 3.5) and ionisation (figure 3.6) of the in the collision system $\mathrm{Li}^+ - \mathrm{He}(1\mathrm{s})$ are measured in the energy ranges $(10\ \mathrm{keV} - 10\ \mathrm{MeV})$ and $(20\ \mathrm{keV} - 100\ \mathrm{MeV})$, respectively.

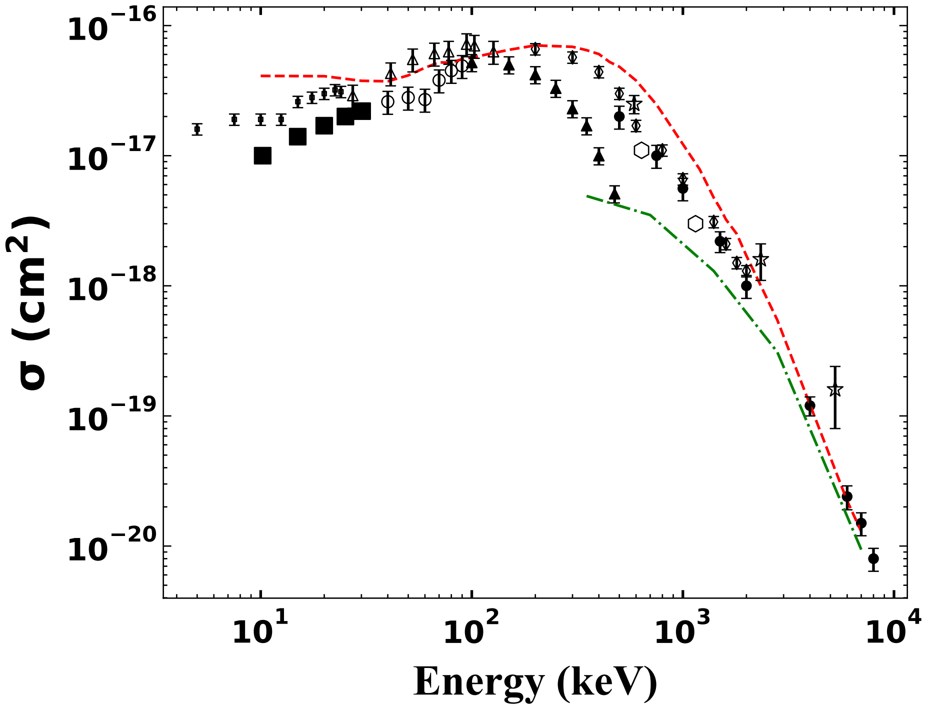

Figure 3.5 Electron capture TCS of the collision system $\mathrm{Li}^+ - \mathrm{He}(1\mathrm{s})$ versus the impact energy. red dashed line: CTMC results [35]. Theoretical references; green dash-dotted line: Samanta et al [33]. Experimental references; solid triangle: Allison et al [87], open square: Van Eck et al [88], open hexagon: Nikolaev et al [89], solid square: Ogurtsov et al [90], open triangle: Pivovar et al [91], open diamond: Pivovar et al [92], open star: Dmitriev et al [93], open circle: Hvelplund [94].

For the case of electron capture cross section, we compared them with both experimental data and theoretical results by Samanta et al utilizing the BCCIS-4B approximation [33]. Encouragingly, within the investigated range of impact energies, our CTMC results exhibited a favourable agreement with experimental data. However, an intriguing discrepancy emerged between the experimental data of Allison et al [87] and Pivovar et al [92] for impact energies spanning 200 keV to 500 keV. Notably, both our CTMC results and Samanta et al's[33] theoretical results demonstrated an impressive alignment with experimental data above 5 MeV. It is crucial to highlight that Samanta et al's BCCIS-4B model exhibited a substantial underestimation of electron capture cross sections for impact energies below 5 MeV, thereby shedding light on the limitations of this theoretical approach.

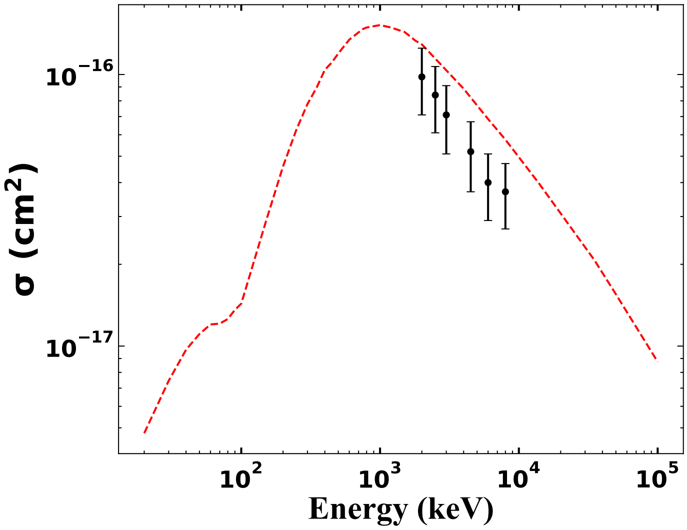

Figure 3.6 Single-electron ionization TCS of the collision system$\mathrm{Li}^+ - \mathrm{He}(1s)$ versus the impact energy. CTMC results [35]. Solid circle: experimental data by Woitke et al [34].

In the single ionisation cross section case of the $\mathrm{Li}^+ - \mathrm{He}(1s)$ collision system, a striking feature observed in the ionization cross section of helium by Li^+ is the presence of a conspicuous bump at low impact energies. This distinctive feature has been attributed to the oscillation of the target electron between the projectile ion and the target nucleus just prior to ionisation, see Schultz et al work [95]. It is noteworthy to mention that prior to our study, Woitke et al [34] were the sole source of ionisation results for the $\mathrm{Li}^+ - \mathrm{He}(1s)$ system within the energy range of 2000 to 8000 keV. Our CTMC results revealed a subtle divergence from the experimental data provided by Woitke et al [34], with our findings indicating slightly larger ionisation cross sections. This discrepancy highlights the need for further investigation to elucidate this disparity between theoretical predictions and experimental observations in the ionisation process of the $\mathrm{Li}^+ - \mathrm{He}(1s)$ collision system.

3.3 Total cross sections of single electron capture and ionisation from ground state nitrogen by Li^+

The total cross sections (TCS) of electron capture (figure 3.7) and ionisation (figure 3.8) of the in the collision system $\mathrm{Li}^+ - \mathrm{N}$ are measured in the energy ranges $(10\ \mathrm{keV} - 2\ \mathrm{MeV})$ and $(20\ \mathrm{keV} - 100\ \mathrm{MeV})$, respectively.

Table 3.1 shows TCSs of electron capture from N(1s), N(2s) and N(2p) shells by Li^+ at selected impact energies. Notably, the cross sections arising from the N(1s) shell were found to be negligible when compared to contributions from N(2s) and N(2p), for this reason they were not plotted in figure 3.8. However, the cross sections from N(1s) are included in the overall TCS of nitrogen, which is the summation of electron capture TCSs from N(1s), N(2s) and N(2p) shells. The TCS in table 3.1 are for single electron, however, the plotted TCSs are multiplied by the number of electrons in that shell, i.e., TCS of (2s) shell is multiplied by 2 where TCS of (2p) shell is multiplied by 3. From figure 3.7 and table 3.1, we see that the TCS from N(2s) shell surpasses the TCS of the N(2p) shell.

Table 3.1 TCS of electron capture in the intraction of Li^+ with N(1s), N(2s) and N(2p) shells.

E (keV)	$\sigma(N1s)$ cm^2	$\sigma(N2s)$ cm^2	$\sigma(N2p)$ cm^2
600	4.4470×10^{-21}	1.4093×10^{-17}	2.5991×10^{-17}
1000	3.9026×10^{-20}	6.7748×10^{-18}	8.1135×10^{-18}
1400	2.4266×10^{-20}	3.3120×10^{-18}	2.7918×10^{-18}
1600	2.4318×10^{-20}	2.6264×10^{-18}	2.1513×10^{-18}
1800	2.9212×10^{-20}	1.8373×10^{-18}	1.4759×10^{-18}
2000	3.6426×10^{-20}	1.5117×10^{-18}	8.0249×10^{-19}

The calculations revealed that electron capture predominantly originates from the outermost electrons (N(2p)) for impact energies below 800 keV, with N(2s) gaining significance at higher energies. The CTMC results align closely with experimental data by Pivovar et al [92] for impact energies exceeding 200 keV. In contrast, Allison et al's [87] experimental data consistently underestimates electron capture cross sections for impact energies above 100 keV, while below 200 keV, CTMC calculations surpass experimental data as reported by Ogurtsov et al [90] and Lockwood [96]. Collectively, the available experimental data suggests that electron capture from the nitrogen ground state by Li^+ tends to decrease at both high and low projectile impact energies, with the highest cross sections occurring at approximately 100 keV energies.

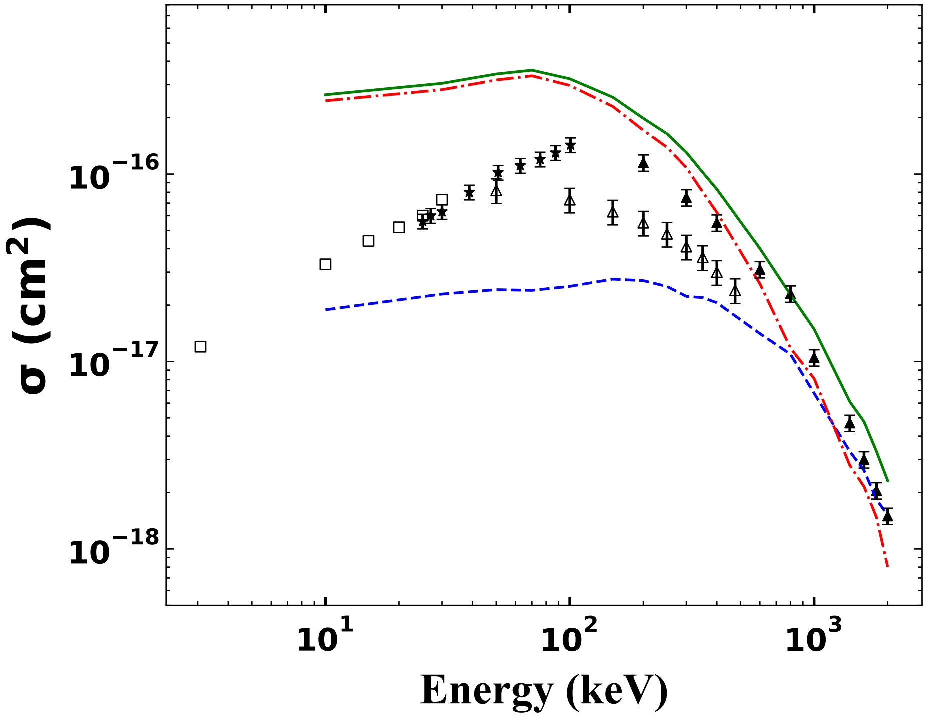

Figure 3.7 Electron capture TCS of the collision system $\mathrm{Li}^+ - \mathrm{N}$ versus the impact energy. CTMC results [35], blue dashed line: TCS from $N(2s)$, red dashed-dotted line: TCS from $N(2p)$, green solid line: sum of TCS from $N(2s)$ and $N(2p)$. Experimental references, open triangle: Allison et al [87], open square: Ogurtsov et al [90], solid star: Lockwood [96], solid triangle: Pivovar et al [92].

Figure 3.8 shows the ionisation TCS of $\mathrm{Li}^+ - \mathrm{N}$ collision as a function of projectile impact energy. Unlike the $\mathrm{Li}^+ - \mathrm{He}(1\mathrm{s})$ system, we can see there is no bump in total cross section the $\mathrm{Li}^+ - \mathrm{N}$ system. Figures 3.6 and 3.8 clearly demonstrate that the $\mathrm{Li}^+ - \mathrm{N}$ system consistently exhibits higher cross-sections at corresponding impact energies. This behaviour can be attributed to the lower binding energy of the N(2p) active electron in the nitrogen target compared to the He(1s) target, resulting in more favourable conditions for ionization in $\mathrm{Li}^+ - \mathrm{N}$ collisions.

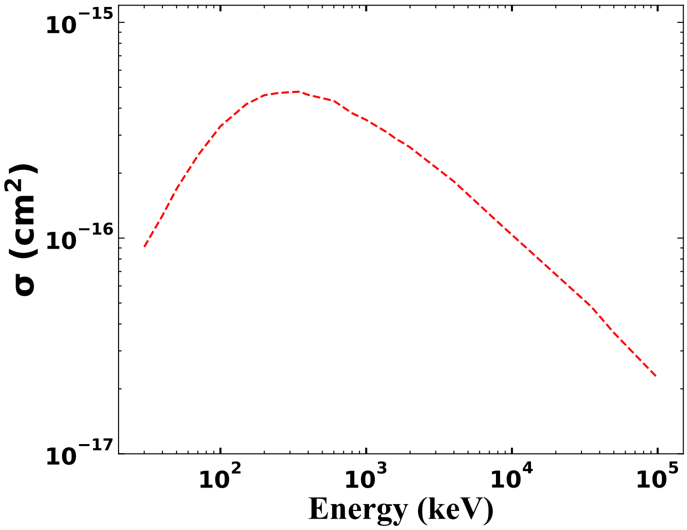

Figure 3.8 Single-electron ionization TCS of the collision system $\mathrm{Li}^{+} - \mathrm{N}$ versus the impact energy. Red dashed line: CTMC results [35].

3.4 Total and Differential Ionisation Cross Sections in collision between Nitrogen atom and Singly Charged Sodium Ion

This section presents the total (TCS), single (SDCS) and double differential (DDCS) cross sections in the collision of singly charged sodium ion (Na^{+}) with neutral nitrogen atom (N). The TCS of ionisation process is measured in the impact energy range $(10\ \mathrm{keV} - 10\ \mathrm{MeV})$. The differential cross sections were calculated for Na^{+} impact energies' 30, 40, 50 and 60 keV.

3.4.1 Total ionisation cross section

Figure 3.9 illustrates the ionisation TCS in the collision system $\mathrm{Na}^{+} -$ N. The broad impact energy range in the TCS case serves as a benchmark for future measurements or calculations. The maximum observed ionisation TCS occurs around an impact energy of 2 MeV. The green shaded area specifically highlights the energy range needed for plasma diagnostics in fusion plasma research.

The results of TCS of $Na^+ - N$ collision system in this thesis are compared with the experimental data of Graham et al [97]. It is crucial to note that while Graham et al [97] studied molecular nitrogen, this study focused on atomic target. To facilitate a meaningful comparison, we made adjustments by multiplying our results by two (to account for two equivalent nitrogen atoms) and by three (reflecting the three electrons in the 2p shell). Ultimately, our calculated total cross sections showed a good agreement with the experimental data of Graham et al [97].

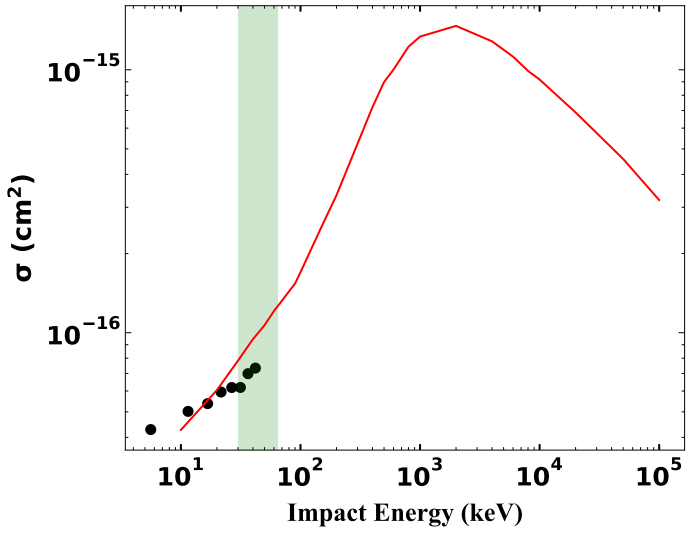

Figure 3.9 TCS of ionisation in the collision system $Na^+ - N$ as a function of the impact energy. Solid red line: CTMC results, solid circles: experimental data by Graham et al [97].

3.4.2 Ionisation single differential cross section (SDCS)

Figures 3.10 and 3.11 show the energy and angular single differential cross section (SDCS) of ejected electrons from nitrogen atom in $Na^+ - N(2p)$ collision system. In Figure 3.10, the energy SDCS is presented across various projectile impact energies ranging from 30 keV to 60 keV. Regardless of the impact energy, the dominance of low-energy electrons is evident. The energy SDCS values exhibit close proximity and follow a consistent trend, reflecting the similarity in impact energy values investigated. Notably, a rapid decrease in SDCS is observed around 10 eV.

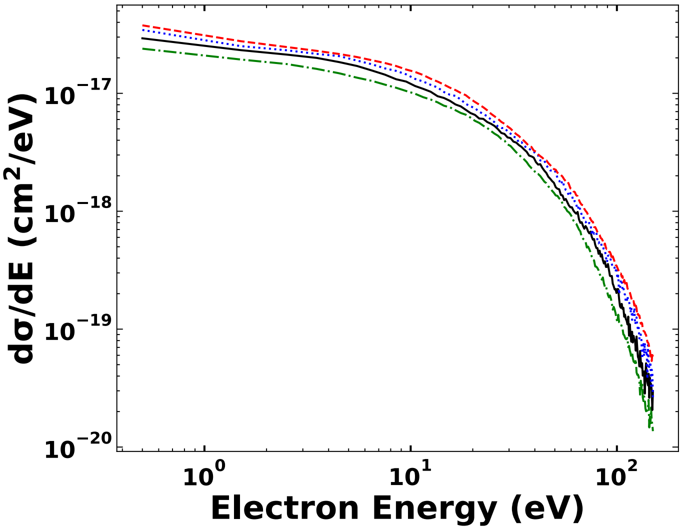

Figure 3.10 Energy single differential cross section of the ejected electrons from nitrogen in the interaction $\mathrm{Na}^+ - \mathrm{N(2p)}$ as a function of the ejected electron energies. Green dashed-dotted line: 30 keV, black solid line: 40 keV, blue dotted line: 50 keV, red dashed line: 60 keV.

Moving to figure 3.11, there is a direct relationship between impact energy and angular differential cross sections (SDCS). Higher impact energies correspond to increased angular SDCS, with dominant electron yields concentrated at lower scattering angles. Interestingly, substantial electron yield is also observable at backward angles. The cross section minimums are located within an emission angle range around 90 degrees.

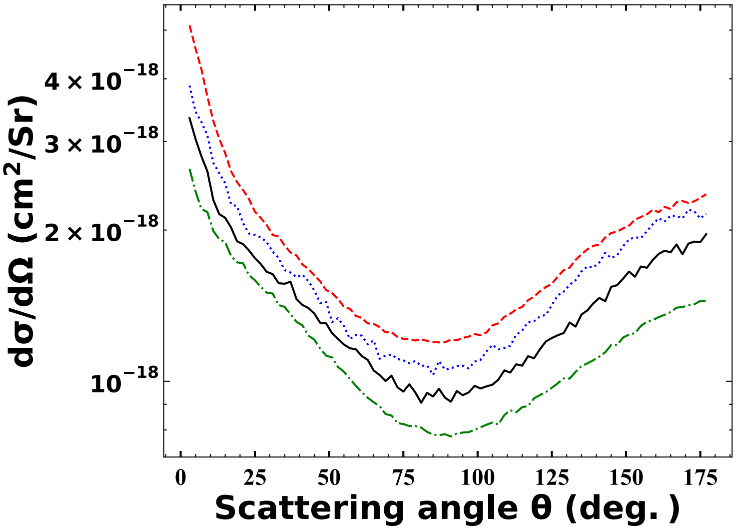

Figure 3.11 Angular single differential cross section of the ejected electrons from nitrogen in the interaction $\mathrm{Na}^+ - \mathrm{N}(2\mathrm{p})$ as a function of the ejection angle of the electron. Green dashed-dotted line: 30 keV, black solid line: 40 keV, blue dotted line: 50 keV, red dashed line: 60 keV.

3.4.3 Ionisation Double differential cross section (DDCS)

The DDCSs of $\mathrm{Na}^+ - \mathrm{N}(2\mathrm{p})$ collision system at Na^+ projectile energy of 30 and 60 keV are presented as contour plots in figures 3.12 and 3.13, respectively. The DDCSs in the contour plots are function of energy and scattering angle of the ionised electron. The maximum DDCS is acquired at low scattering angles ($\theta < 20^o$) and low ejection energies ($< 10\ eV$) of the ionised electron. The DDCSs of 30 keV and 60 keV projectile energies of electrons ejected with energy greater than 15 eV show equivalent results sweeping all scattering angles. However, over scattering angles between 60^o and 120^o and ejection energy less than 10 eV, the DDCSs for both impact energies show different trend. In this region, the DDCS results of 30 keV projectile energy show curved up behaviour with a low minimum, however, the DDCS results of 60 keV projectile energy do not show similar curves.

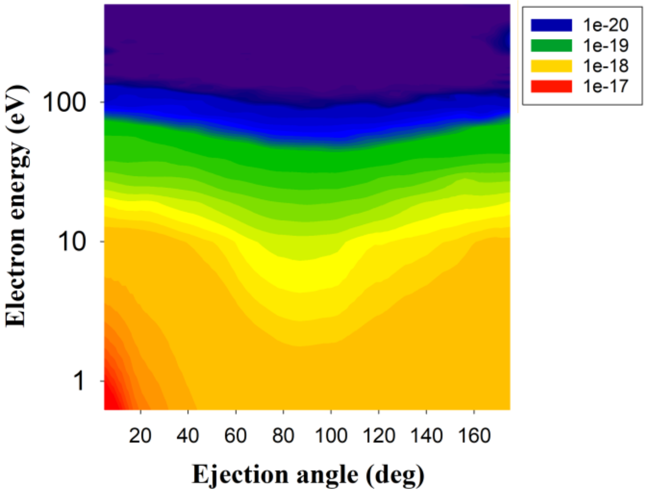

Figure 3.12 DDCS of ionisation of the outermost electron of nitrogen after colliding with 30 keV Na$^+$. The DDCS is a function of the energy and angle of scattering of the electron.

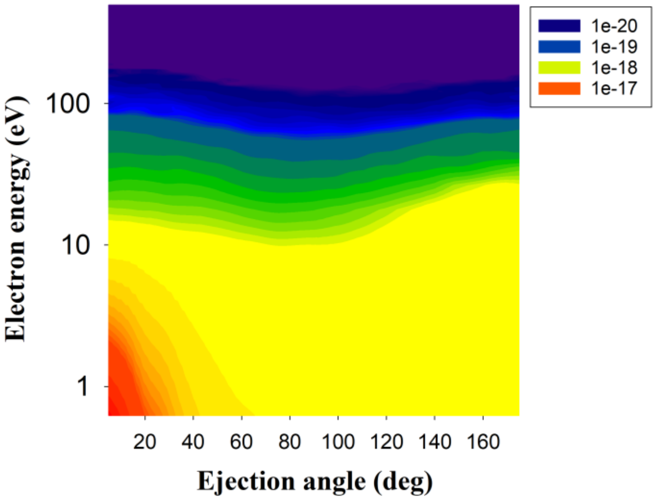

Figure 3.13 DDCS of ionisation of the outermost electron of nitrogen after colliding with 60 keV Na$^+$. The DDCS is a function of the energy and angle of scattering of the electron.

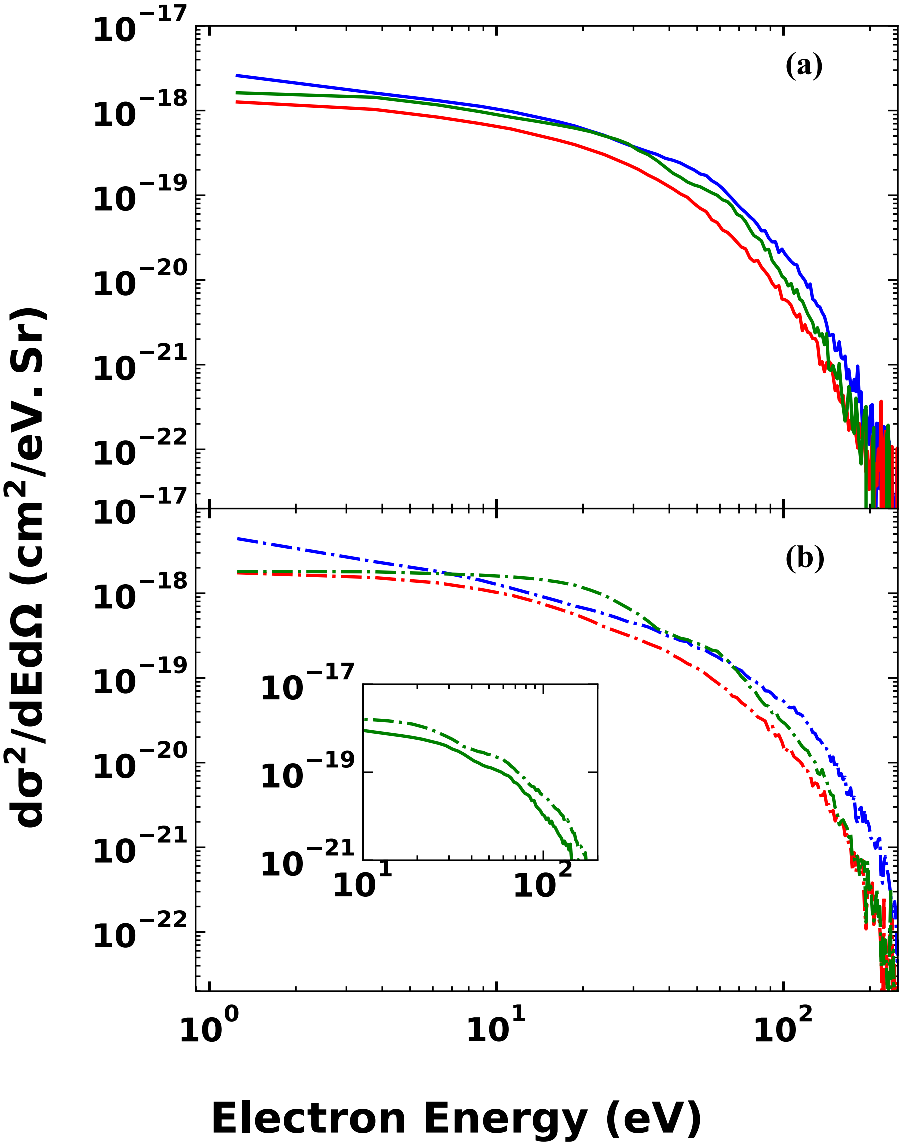

Figure 3.14 DDCS of ionisation of the outermost electron of nitrogen after colliding with Na^+ projectile with energy **a)** 30 keV and **b)** 60 keV. The DDCS is a function of electron energy. Solid lines are for 30 keV while the dashed lines are for 60 keV. The considered scattering angles: blue line: $30^o \pm 15^o$; red line: $90^o \pm 15^o$; green line: $150^o \pm 15^o$.

Figure 3.14 displays the dependence of the DDCS on the energy of the ionised electron. For This analysis, DDCSs are calculated at impact energies 30 keV and 60 keV at selected ejection angles, namely, 30^o, 90^o

and 150^o with $\pm 15^o$ range. For electrons ionised with energy 5 eV and less, the highest and lowest DDCS values are acquired at forward scattering (30^o) at 60 keV impact energy and right scattering (90^o) at 30 keV impact energy, respectively.

From figure 3.14, we can see that the overall pattern for all curves is almost similar, all DDCS curves starts high at lower ejection energies of electrons, then, the DDCS curves steadily decline until the electron energy approaches 20 eV [an exception here is the DDCS curve of impact energy of 60 keV in backward scattering (150^o), which sustains nearly consistent values in this energy range]. Beyond electron energies 20 eV, the DDCS curves plummet sharply.

The presence of the Fermi shuttle-type ionisation process is discernible in energy spectra, (green lines in small box in figure 3.14 (b))[98–101]. This complex mechanism entails ejected electrons undergoing multiple scattering events on both the projectile and target core throughout the projectile's motion. Notably, each collision with the projectile core leads to an increase in electron energy. The cumulative effect of these back-and-forth collisions manifests in electrons attaining relatively high energies. The heightened energy levels of these accelerated electrons are reflected in energy spectra, showcasing an increased electron yield at corresponding energies.

The inception of the Fermi acceleration concept can be traced back to 1949 when Fermi [102] proposed it as a potential origin of high-energy cosmic rays. Fermi's theoretical framework involves the interaction of giant electromagnetic fields moving in opposition, thereby accelerating charged particles through a series of reflections. Subsequent investigations unveiled a comparable "ping-pong" dynamic occurring within much smaller microscopic fields of atoms, molecules, or clusters [98–101,103–108]. Even a brief succession of scattering events within these microscopic fields can yield noteworthy observations.

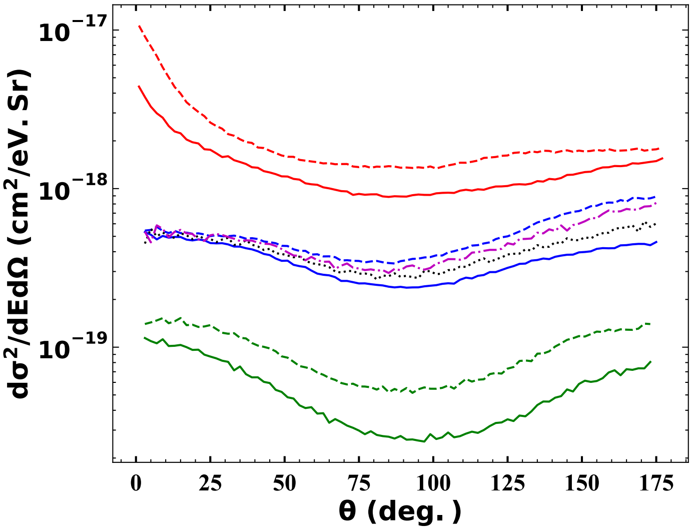

Figure 3.15 DDCS of ionisation of the outermost electron of nitrogen after colliding with Na^+ projectile with energy, solid lines: 30 keV, dotted lines: 40 keV, dashed-dotted lines: 50 keV and, dashed lines: 60 keV. The DDCS is a function of scattering angles. Electrons energies are categorized by colours as follows: red lines: $0 < E_e \leq 12\ eV$; blue, black, and magenta lines: $12 < E_e \leq 50\ eV$; green lines: $50 < E_e \leq 100\ eV$.

Figure 3.15 displays the dependence of the DDCS on the scattering angle of the ionised electron. For This analysis, DDCSs are calculated at impact energies 30 keV, 40 keV, 50 keV and 60 keV at selected electrons energies, namely, $0 < E_e \leq 12\ eV$, $12 < E_e \leq 50\ eV$ and $50 < E_e \leq 100\ eV$.

DDCSs exhibit the maximum values for ionised electrons with energies less than 12 eV when observed at small scattering angles. As the scattering angles increase, the DDCS values show a decreasing trend until they reach 60 degrees. Beyond this point, the DDCSs remain relatively unchanged.

Notably, at a projectile energy of 60 keV, DDCS values surpass those obtained at 30 keV for all angles and electron energies.

For ejected electrons with energies ranging from 50 to 100 eV, DDCS values are at their smallest, and both direct and back scattering DDCSs demonstrate comparable magnitudes. The minimum DDCSs are observed at right scattering ($\theta = 90^o$). In the case of ejected electrons with energies falling within the 12-50 eV range, a distinct pattern emerges. At low angles, DDCS values for all impact energies are nearly identical, but as the angles increase, the DDCS curves diverge. The greatest gap between the curves of the four energies is observed at angles near ($\theta = 180^o$).

Comparing the DDCSs of direct and backscattered scattering for 30 and 60 keV projectiles energies, the former is slightly greater than the latter for 30 keV case. Conversely, for the 60 keV case, the direct scattering is slightly smaller than its counterpart. The overall findings indicate that an increase in projectile energy leads to a higher ionization of backscattered electrons compared to direct scattering within this energy range.

3.5 Collision of Singly Charged Sodium Ions with Noble Gases

This section presents the total (TCS), single (SDCS) and double differential (DDCS) cross sections in the collision of singly charged sodium ion (Na^+) with neon (Ne), argon (Ar), krypton (Kr) and xenon (Xe). The TCS for electron capture and ionisation processes are measured in the projectile energy range $(10\text{keV} - 50\text{MeV})$. For the SDCS and DDCS, the energy of Na^+ is set to be 60 keV, this projectile energy is chosen for diagnostic purposes of the plasma. At this projectile energy, there is an increased probability of interactions occurring between Na^+

and the plasma, making it optimal for these diagnostic purposes. Lower projectile energies would result in reduced penetration of the plasma by Na^+ projectiles, limiting their effectiveness in diagnostic applications. Conversely, much higher impact energies would lower the probability of collisions between Na^+ projectiles and the plasma.

3.5.1 Total cross section (TCS) of electron capture and ionisation.

The total cross sections (TCSs) for electron capture and ionization channels are presented in figures 3.16 and 3.17, respectively. The peaks of TCS for all targets are around projectile energy 100 keV for electron capture channel and around projectile energy 2000 keV for ionisation channel.

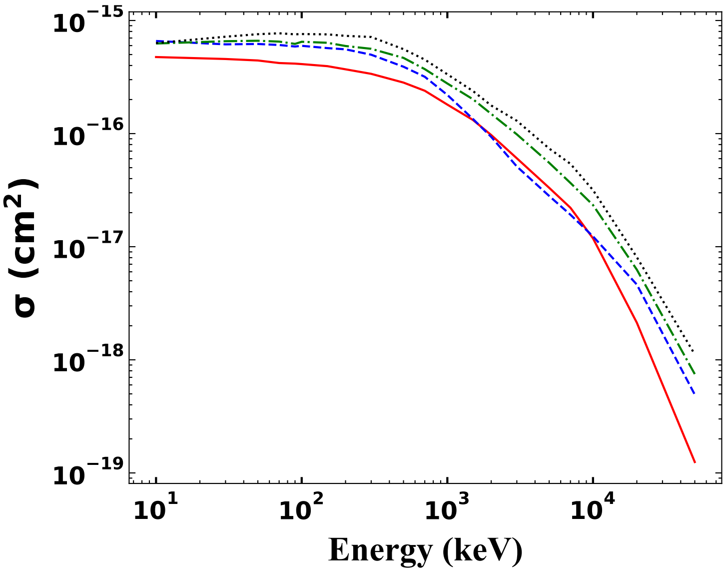

Figure 3.16 TCS of electron capture in the interaction of singly charged Sodium ion with, red solid line: Neon (2s and 2p), blue dashed line: Argon (2p, 3s, and 3p), green dashed-dotted line: Krypton (3d, 4s and 4p), black dotted line Xenon (3d, 4s, 4p, 4d, 5s and 5p).

In electron capture case (figure 3.16), all targets show high values of TCS at low projectile energies, and the TCS values for all targets remains almost horizontal at projectile energies between 10 keV and 300 keV, then these TCS values sharply decreases for projectile energies above 300 keV. It is clearly seen that Ne has the lowest electron capture TCS while Xe has the highest electron capture TCS. The electron capture TCSs of Ar and Kr show close values to each other, with the TCS of Kr slightly overestimate the TCS of Ar, this slight difference arises from close binding energies of the outermost electron of Ar in 3p shell and Kr in 4p shell, see table 2.2. However, the electron capture TCS of Ar exceeds the TCS of Kr for projectile energies larger than 10 MeV, this is due to significant contribution from the Ar(2p) shell to the total TCS of Ar.

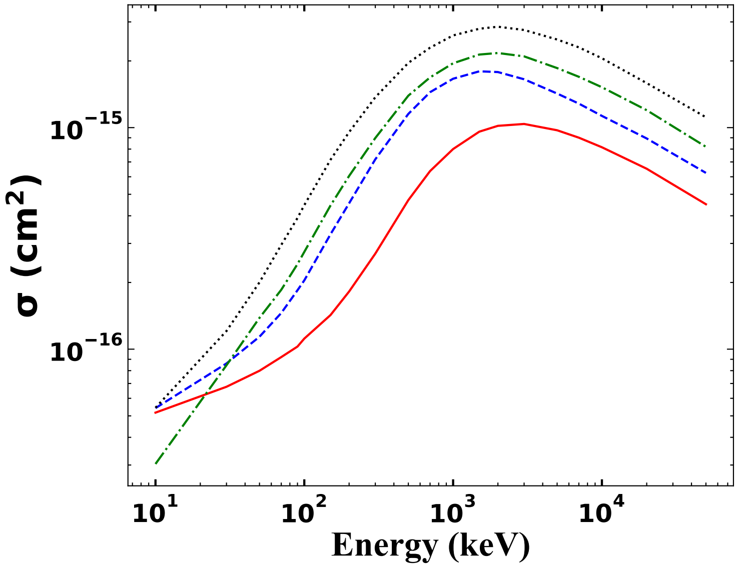

Figure 3.17 TCS of ionisation in the interaction of singly charged Sodium ion with, red solid line: Neon (2s and 2p), blue dashed line: Argon (2p, 3s, and 3p), green dashed-dotted line: Krypton (3d, 4s and 4p), black dotted line Xenon (3d, 4s, 4p, 4d, 5s and 5p).

In ionisation case (figure 3.17), the TCS curves of the various targets follow a similar trend. The lowest TCS values occurs at low projectile energies (i.e., less than 10 keV). All the TCS curves experience a rapid ascent with increasing the projectile energy until they reach their peak values at projectile energy around 1500 keV. After reaching their respective maxima, the TCS curves display a gradual decline, the decline is less steep compared to the preceding increase. Similar to the TCS pattern observed in electron capture, Neon (Ne) demonstrates the smallest ionisation TCS, while Xenon (Xe) exhibits the highest values. However, there is a notable exception for Krypton (Kr), which, at impact energies less than 20 keV, displays the smallest ionisation TCS among the elements studied.

3.5.2 Single differential cross section (SDCS) of ionisation

Figures 3.18 and 3.19 show the energy and angular single differential cross section (SDCS) of ejected electrons from nitrogen atoms and noble gases in the interaction with Na^{+}, respectively. The SDCS is presented at projectile energy of 60 keV. In Figure 3.18, the curves of Xe(4d) and Xe(5p) exhibit an identical pattern. Notably, the Xe(5p) curve shows a significantly higher level at lower energies, primarily owing to a notable difference in binding energy. However, as the electron energy increases, the disparity between the Xe(4d) and Xe(5p) curves diminishes. Beyond 100 eV, the curves of Xe(4d) and Xe(5p) overlap. Comparing Kr(4p) to Xe(5p), it is observed that the former shares an identical curve with slightly lower but closely aligned energy SDCS values. This slight difference is attributed to Kr(4p)'s marginally higher binding energy than Xe(5p), as elucidated in table 2.2. Examining the TCS curves of Ar(3p), Kr(4p), Xe(4d), and Xe(5p), a common characteristic is their initial high values at lower energies. A gradual decrease is discernible in the electron energy range below approximately 10 eV. Above this threshold, the energy SDCS curves exhibit a drastic drop. Notably, the energy SDCS curves of N(2p) and Ne(2p) display a less steep decrease at lower energies compared to the previously mentioned targets. The significant drop in N(2p)'s curve occurs around 10 eV, whereas the Ne(2p) curve maintains a higher value over a more extended energy range, experiencing a substantial decline between 40 and 50 eV.

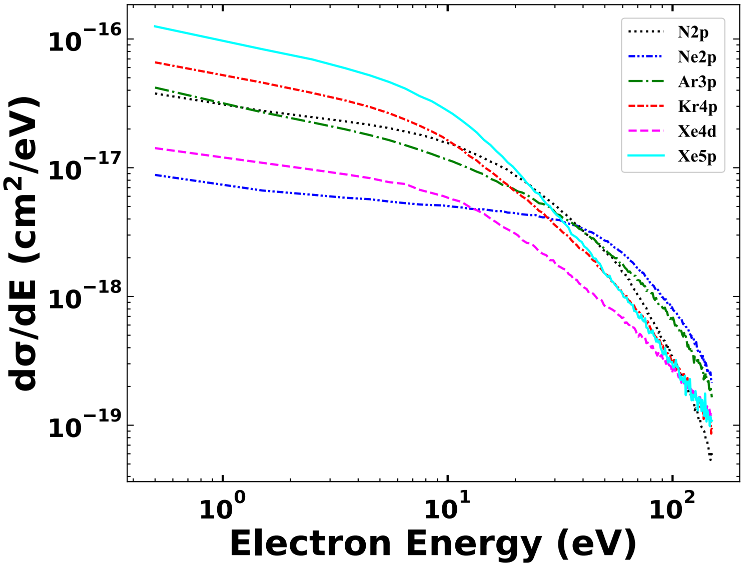

Figure 3.18 Energy single differential cross of the ejected electron from noble gases and nitrogen in the interaction with 60 keV Na^+. The SDCSs are function of the ejected electrons' energy. Black dotted line: $N(2p)$, blue dashed--two-dots line: $Ne(2p)$, green dashed-dotted line: $Ar(3p)$, red two-dashes-dotted line: $Kr(4p)$, magenta dashed line: $Xe(4d)$, cyan solid line: $Xe(5d)$.

In Figures 3.19, the angular distribution of SDCS for the studied targets is depicted. Two distinct trends emerge, with Ar(3p), Kr(4p), Xe(4d), and Xe(5p) following one trend, while N(2p) and Ne(2p) adhere to another. In both trends, direct scattering predominates. The differentiation lies in backscattering: Ar(3p), Kr(4p), Xe(4d), and Xe(5p) show no significant distinction between backward and right scattering. Conversely, for N(2p) and Ne(2p), backscattering surpasses right scattering. Angular SDCSs of the targets are arranged based on binding energies, revealing that the target with the lowest binding energy exhibits the highest angular SDCS values, and vice versa. An exception is observed in N(2p), where N(2p), Ar(3p), and Kr(4p) have closely aligned binding energies, resulting in similar angular SDCS curves. In forward scattering, the angular SDCS of N(2p) is lower than that of Ar(3p) and Kr(4p), whereas in backward scattering, the angular SDCS of N(2p) surpasses that of Ar(3p) and Kr(4p).

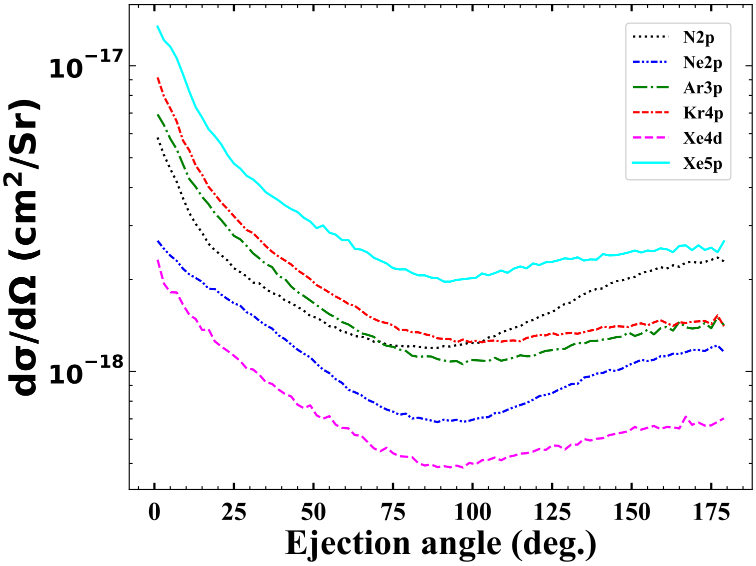

Figure 3.19 Angular single differential cross of the ejected electron from noble gases and nitrogen in the interaction with 60 keV Na^+. The SDCSs are function of the ejected electrons' scattering angle. Black dotted line: $N(2p)$, blue dashed-two-dots line: $Ne(2p)$, green dashed-dotted line: $Ar(3p)$, red two-dashes-dotted line: $Kr(4p)$, magenta dashed line: $Xe(4d)$, cyan solid line: $Xe(5d)$.

3.5.3 Double differential cross section (DDCS) of ionisation

Figure 3.20 illustrates the contour of DDCS as a function of ionised electron's energy and scattering angle in the collision of 60 keV Na^+ with the outer shells of Ne, Ar, Kr and Xe. For the four targets, the maximum values of DDCS are acquired at low electrons' energies and scattering angles, (approximately, $E_e \leq 10\, eV, \theta \leq 40^o$), while the lowest values of DDCS are acquired at electrons with energies exceeding 100 eV for all angles. The contour of Ne(2p) shows different trend when compared to the contours of the other three targets. Further discussion of DDCS is provided next for more in depth details, figures 3.21, 3.22 and 3.23.

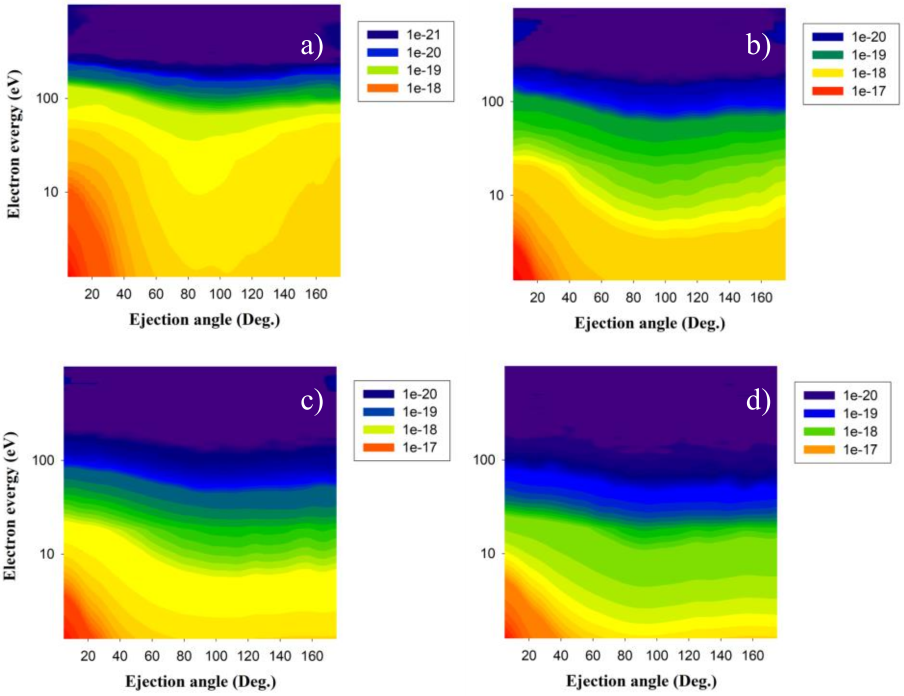

Figure 3.20 Contour plot of DDCS of ionisation process as a function of scattering angle and ejection energy of the ionised electron in the collision of 60 keV Na^+ with noble gases. **a)** Ne(2p), **b)** Ar(3p), **c)** Kr(4p), **d)** Xe(5p).

Figure 3.21 displays the dependence of the DDCS on the energy of the ionised electron categorised based on the target. The DDCSs are calculated at projectile energies 60 keV at selected ejection angles, namely, $\theta < 15^o$, 30^o, 60^o, 90^o, 120^o and 150^o, with $\pm 15^o$ range except for $\theta < 15^o$. Notably, the maximum value of DDCS is observed at low scattering angles (i.e., $\theta < 15^o$) across the various targets considered. Among the four targets, the DDCS curves of Ne(2p) at scattering angles

$(60^o, \ 90^o, 120^o$ and $150^o)$ maintain a relatively constant level in the energy range below 60 eV [An exception here is the DDCS curve of 30^o in which we see a slight drop from outset to electron energy around 10 eV]. For energies lager than 50 eV, the DDCS curves of Ne(2p) show a sudden drop. Conversely, for other targets, the DDCS curves commence decreasing from the outset, with the decline starting around 10 eV.

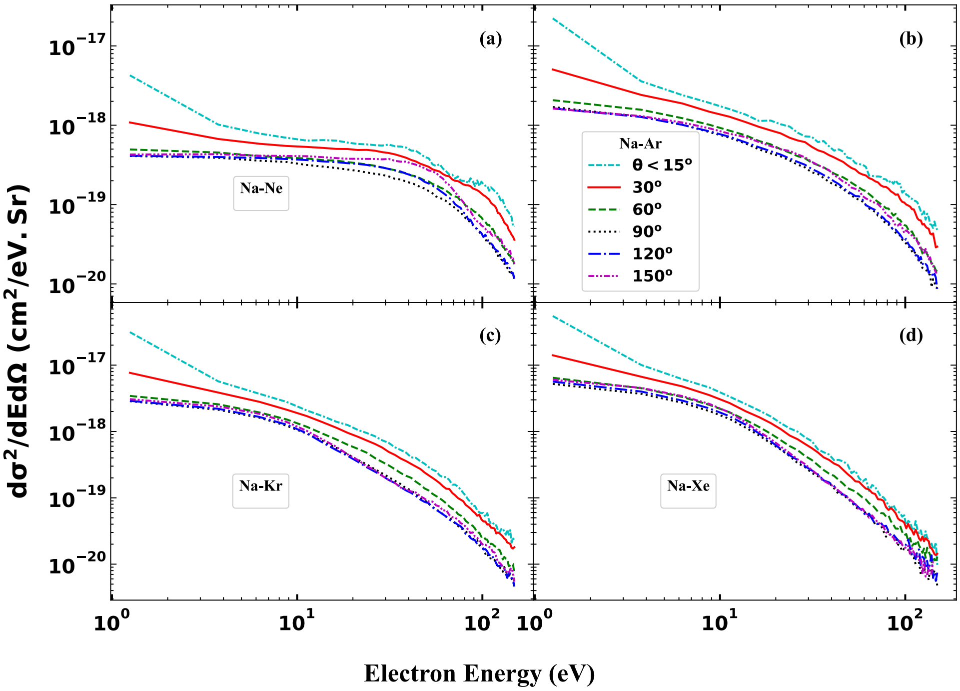

Figure 3.21 DDCS of ionisation of the outermost electron of **a)** Ne(2p), **b)** Ar(3p), **c)** Kr(4p) and **d)** Xe(5p) by 60 keV Na$^+$. The DDCS is a function of electron energy. Scattering angles; cyan two-dashes-dotted line: $\theta < 15^o$, red solid line: 30^o, green dashed line: 60^o, black dotted line: 90^o, blue dashed-dotted line: 120^o, and magenta dashed-two-dots line: 150^o.

In the collision systems $Na^+ - Ne(2p)$ and $Na^+ - Ar(3p)$, starting with the DDCS curve of the scattering angle $\theta < 15^o$, we see the previously discussed Fermi shuttle-type ionisation process [see section 3.4.3], this process is observed for electron energy larger than 10 eV and is also slightly observed for scattering angle $\theta < 30^o$. For the case of $Na^+ -$

$Ne(2p)$, the DDCS curve of scattering angle 90^o starts to drop around electron energy of 10 eV, the DDCS curves of scattering angles 60^o and 120^o start to drop around electron energy of 20 eV, while DDCS curve of the scattering angle 150^o will maintain the horizontal line for electron energy around 60 eV before dropping. After the drop, for electron energies larger than 70 eV, the DDCS curves of scattering angles 60^o and 150^o overlaps, while the DDCS curves of scattering angles 90^o and 120^o overlaps. Meanwhile, the DDCS curves of $\theta < 15^o$ and 30^o will maintain the highest and second highest values for all electrons' energies, respectively. Going to the case of $Na^+ - Ar(3p)$, compared to the case of $Na^+ - Ne(2p)$, a main difference is that the DDCS curves of scattering angles $60^o,\ 90^o$, 120^o and 150^o will start the gradual decrease from the lowest electron energies on the curve. A second difference is that the DDCS curve of scattering angle 60^o is slightly higher than the DDCS curves of scattering angles 90^o, 120^o and 150^o for electron energies less than 10 eV. Going to the similarities, the DDCS curves of $\theta < 15^o$ and 30^o will maintain the highest and second highest values for all electrons' energies, respectively. Moreover, we will also see the overlapping of the DDCS curves of scattering angles 60^o and 150^o, and the overlapping of the DDCS curves of scattering angles 90^o and 120^o.

The DDCS curves of Kr(4p) and Xe(5p) demonstrate analogous behaviour, with $\theta < 15^o$ consistently exhibiting the highest DDCS across all energies, followed by 30^o. Below 10 eV, DDCS curves at $60^o,\ 90^o$, 120^o and 150^o scattering angles are overlapping. Beyond 10 eV, the DDCS at 60^o diverges and surpasses the other angles, while 90^o, 120^o and 150^o angles continue to exhibit the overlapping pattern.

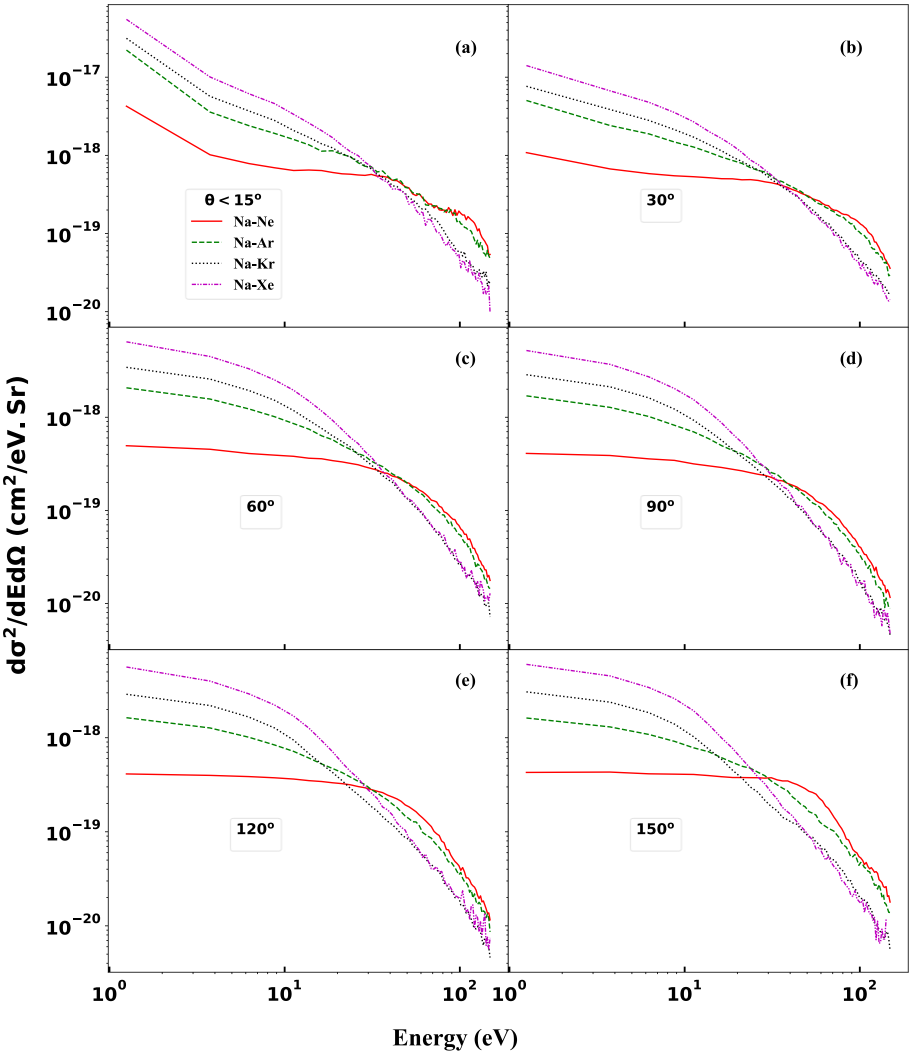

Figure 3.22 DDCS of ionisation of the outermost electron at scattering angles of **a)** $\theta < 15^o$, **b)** 30^o, **c)** 60^o, **d)** 90^o, **e)** 120^o and **f)** 150^o by 60 keV Na^+. The DDCS is a function of electron energy. The targets; red solid line: *Ne(2p)*, green dashed line: Ar(3p), black dotted line: Kr(4p), and magenta dashed-two-dots line: Xe(5p).

Figure 3.22 displays the dependence of the DDCS on the energy of the ionised electron categorised based on the scattering angles. An analogous pattern of the DDCS is seen for angles $\theta < 15^o$ and 30^o. We can clearly see that the DDCS curves intersect in the electron energy range $30 -$

$40\ eV$ for angles $\theta \leq 90^o$, and in the electron energy range $20 - 30\ eV$ for the angles 120^o and 150^o. Below the intersection energy, DDCS of Xe(5p) is the maximum, followed by the DDCS of Kr(4p) then Ar(3p) whereas the DDCS of Ne(2p) is the lowest. After the intersection energy, the DDCS of Ne(2p) becomes the largest followed by the DDCS of Ar(3p) with insignificant difference, moreover, the DDCSs of Xe(5p) and Kr(4p) overlap and becomes the lowest.

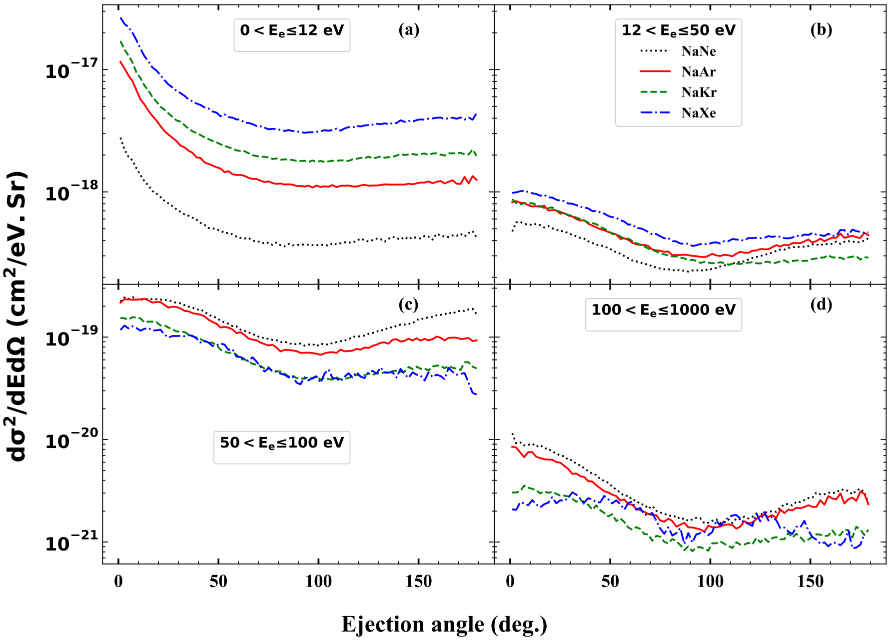

Figure 3.23 DDCS of ionisation of the outermost electron at ejection energy of **a)** $0 < E_e \leq 12\ eV$, **b)** 12< $E_e \leq 50\ eV$, **c)** $50 < E_e \leq 100\ eV$, and **d)** $100 < E_e \leq 1000\ eV$ by 60 keV Na$^+$. The DDCS is a function of scattering angle of the electron. The targets; black dotted line: Ne(2p), red solid line: Ar(3p), green dashed line: Kr(4p), and blue dashed-dotted line: Xe(5p).

Figure 3.23 displays the dependence of the double differential cross section (DDCS) on the scattering angle of the ionised electron. For This analysis, DDCSs are calculated at impact energies 60 keV at selected electrons energies, namely, $0 < E_e \leq 12\ eV$, $12 < E_e \leq 50\ eV$, $50 < E_e \leq 100\ eV$ and $100 < E_e \leq 1000\ eV$. In Figure 3.23(a), the focus is on the Angular DDCS for electron energies below 12 eV. The DDCS curves exhibit similarities for all targets, organized above each other without intersection based on their binding energies, with Ne(2p) registers the lowest DDCS, Xe(5p) records the highest DDCS, while Kr(4p) and Ar(3p) positioned as the second and third, respectively. All DDCS curves start at maximum value at scattering angles $\theta < 10^o$, experience a drastic decrease until approximately 70°, after which they tend to maintain a relatively constant DDCS values.

In Figure 3.23(b), the Angular DDCSs for electron energies in the range $12 < E_e \leq 50\ eV$ are presented. The figure shows that the highest DDCS values are produced at low scattering angles, followed by a gradual decrease with minimum values observed at 90°. Notably, below 90°, the DDCS of Ne(2p) is the lowest, while the DDCS of Xe(5p) is the highest, with Ar3p and Kr4p exhibiting nearly equal values. Beyond 90°, Xe(5p) maintain the largest DDCS, while Kr(4p) records the lowest DDCS. Additionally, the backscattering of Ne(2p) and Ar(3p) surpasses right-angle scattering in this energy range.

In Figure 3.23(c), the Angular DDCSs for electron energies in the range $50 < E_e \leq 100\ eV$ are presented. DDCSs at this energy range are lower than their counterparts at smaller electrons' energy ranges. Notably, DDCS of Kr(4p) and Xe(5p) are almost indistinguishable, and they the smallest compared to Ne(2p) and Ar(3p). DDCSs for all targets start high, followed by a slow decrease until 90°. Beyond 90°, Ar(3p), Kr(4p) and Xe(5p) experience a minute increase, Ne(2p) experience more increase in DDCS in the backscattering diverging from Ar(3p).

In Figure 3.23(d), the Angular DDCSs for electron energies in the range $100 < E_e \leq 1000\ eV$ are presented. DDCS values are the lowest among all energy ranges discussed. DDCSs of Ne(2p) and Ar(3p) are relatively identical, with DDCS of Ne(2p) is slightly higher over all angles. Their DDCSs are largest in forward scattering, followed by backward scattering, and their minimum are at right-angle scattering. The DDCS of Kr(4p) show a similar trend to Ne(2p) and Ar(3p), but it has lower values. The DDCS of Xe(5p) shows a sinusoidal behaviour with crests (at 50^0 and 125^0) and troughs (at 90^0 and 175^0).

3.6 Collision of Protons with noble Gas Atoms

This section presents the total (TCS), single (SDCS) and double differential (DDCS) cross sections in the collision of protons H^+ with neon (Ne), argon (Ar), krypton (Kr) and xenon (Xe). The TCS for electron capture and ionisation processes are measured in the projectile energy range $(0.2\ \mathrm{keV} - 50\mathrm{MeV})$. For the SDCS and DDCS cases, the energy of H^+ is set to be 35 keV, this projectile energy is chosen for diagnostic purposes of the plasma, see discussion in the introduction of section 3.5.

The total cross section of electron capture and ionisation include some sub shells of the targets. For neon, sub shells 2s and 2p. For Argon, 2p, 3s, and 3p. For krypton, 3d, 4s and 4p. For xenon, 3d, 4s, 4p, 4d, 5s and 5p.

3.6.1 Total cross section (TCS) of single electron capture

Figure 3.24 presents the TCS for electron capture during proton interactions with noble gases, specifically Ne, Ar, Kr, and Xe. The impact energy range investigated spans from 0.2 to 1300 keV. The TCS curves have a parabolic shape with peak values at approximately 10 keV, 4 keV, 1 keV, and 0.5 keV for Ne, Ar, Kr, and Xe, respectively.

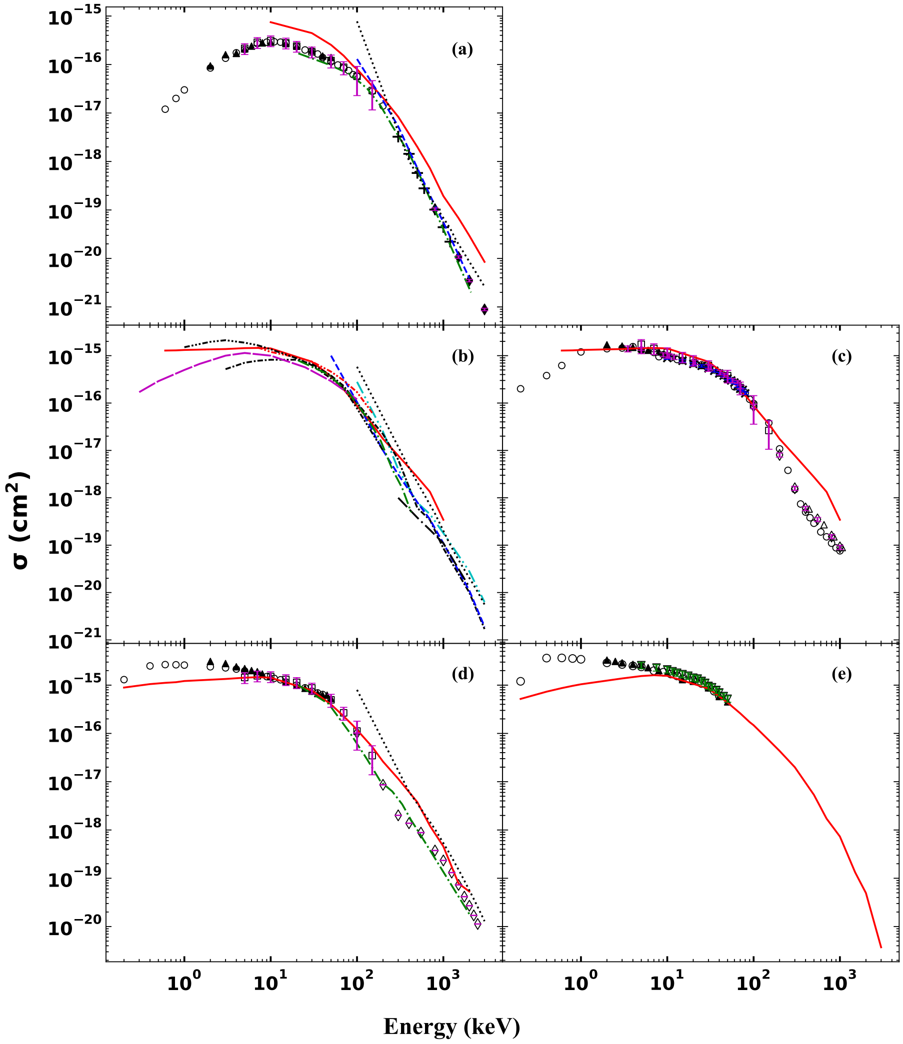

Figure 3.24 TCS of electron capture channel of the collision a) $H^+ - Ne$, b) $H^+ - Ar$, theoretical references, c) $H^+ - Ar$, experimental references, d) $H^+ - Kr$, and e) $H^+ - Xe$. red solid line: Our theoretical CTMC results. Theoretical results; green dashed-dotted line: Nikolaev[109], cyan long-dash-two-dots line Vinogradov et al.[110], black intense dashed-dotted line Shevelko[111], blue dashed line: Belkic[86], black two-long dashes-dotted line :Lin et al.[112], red short-dash-two-dots line: Amaya-Tapia et al.[113], black short-dash-three-dots line: Kirchner et al.[114], magenta long-dashes line: Cabrera_Trujillo et al.[115], black dotted line: Houmar et al.[116]. Experimental results; open circle: Allison[117], solid triangle: Williams et al.[118], open triangle: Welsh et al.[119], open diamond: Toburen et al.[120], black cross: Ormrod et al.[121], open star: Morgan et al.[122], open square: Rudd et al.[123], black diamond: Varghese et al.[124], plus sign: Almeida et al.[125], open inverted triangle: Afrosimov et al.[126].

When comparing the maximum TCS values of the targets, Xe exhibits the highest, Ne the lowest, and Ar and Kr have similar values, with Kr slightly higher. These differences are attributed to the binding energy of the outermost shell, where Ne has the highest, Xe the lowest, and Ar and Kr share close binding energies, as shown in Table 2.2.

In the collision $H^{+} - Ne$ (figure 3.24(a)), experimental data from various sources show good agreement with each other. Theoretical references align well with experimental data beyond 300 keV, with variations noted at lower energies. Our data align well with experimental and theoretical data with slight overestimation. In the collision $H^{+} - Ar$ (figure 3.24(b) and (c)), both theoretical and experimental data align remarkably well in the energy range of 10-200 keV. However, discrepancies emerge at lower and higher energies, where some theoretical models slightly overestimate the experimental results.

In the collision $H^{+} - Kr$ (figure 3.24(d)), the only available theoretical data are by Nikolaev[109] and Houmar[116] et al., and they exhibit varying degrees of agreement when compared with experimental data. Data by Nikolaev[109] consistently aligns well, while Houmar et al.'s[116] results tend to overestimate the experimental data. Additionally, the collision system $H^{+} - Xe$ (figure 3.24(e)) lacks theoretical references, with experimental data limited to the range of 0.2-50 keV.

Our results show a good agreement with the experimental and theoretical data in most of the energy range studied. However, our results slightly overestimate the experimental data at energies higher than 300 keV. Additionally, our data show some discrepancies at low energies less than 10 keV. For the case of $H^{+} - Xe$, we believe our results are accurate based on our results from collision systems $H^{+} - Ne$, $H^{+} - Ar$ and $H^{+} - Kr$.

3.6.2 Total cross section (TCS) of single ionization

In Figure 3.25, the total cross sections (TCS) of ionization resulting from proton interactions with noble gases are depicted, covering an impact energy range of 1 keV to 50 MeV. Notably, the TCS curves exhibit maximums at impact energies within the 60-70 keV range for all target gases. When comparing the ionization TCS maximums of the noble gases—Ne, Ar, Kr, and Xe—similar trends emerge as observed in electron capture TCS. Ne demonstrates the lowest TCS, Xe the highest, and Ar and Kr possess approximately equal TCS values, with Kr slightly higher. These variations are attributed to the binding energy of the outermost shell of the targets, as discussed in the previous sub-section.

For the single ionisation case, the available reference data are by Rudd et al.[123], Clementi et al.[127] and Bunge et al.[128]. Rudd et al.[123] presented experimental data for targets Ne, Ar, and Kr. Clementi et al.[127] and Bunge et al.[128] employing the Roothaan-Hartree-Fock (RHF) method, they presented Theoretical data of many sub shells of targets Ne and Ar. Regarding Kr and Xe, only available theoretical are for inner sub-shells, which has insignificant contribution to the overall TCS, hence they were excluded.

In Figure 3.25(a), the ionisation TCS of Ne are presented. In general, we see a good agreement between the CTMC data, experimental data and theoretical data, especially at high impact energies. At mid energy range, Bunge et al.[128] shows a good agreement with experimental data, the CTMC data align well with Clementi et al.[127], and both slightly overestimate the experimental data. At low energies, the CTMC show very good agreement with experimental data, Clementi et al.[127] and Bunge et al.[128] show inseparable results overestimating the experimental data.

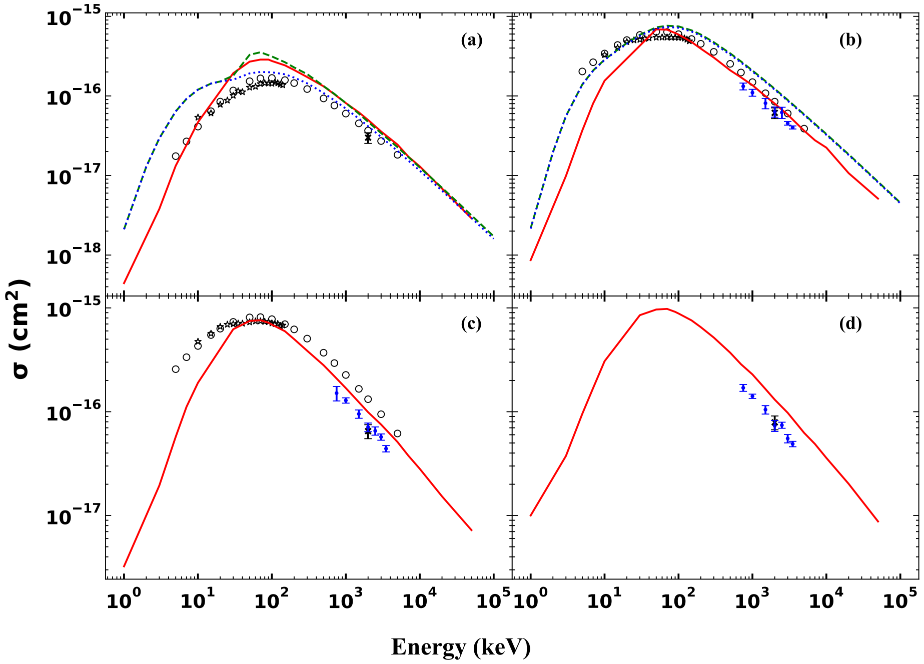

Figure 3.25 TCS of ionization channel in the collision a) $H^+ - Ne$, b) $H^+ - Ar$, c) $H^+ - Kr$, and d) $H^+ - Xe$. Theoretical results; red solid line: Our CTMC results, green dashed line: Clementi et al.[127], blue dotted line: Bunge et al.[128]. Experimental results; open circle: Rudd et al.[123] , solid cross: Melo et al. [129], open star: De Heer et al. [130], small blue circle: Cavalcanti et al. [131].

For proton interactions with Ar (Figure 3.25(b)), Clementi et al.[127] and Bunge et al.[128] closely mirror each other, overestimating experimental data above 50 keV while showing good agreement below this energy. In contrast, the CTMC results exhibit very good agreement with experimental data above 50 keV but underestimate it below 50 keV.

Regarding to the targets Kr and Xe (Figure 3.25 (c) and (d), respectively), the CTMC results of $H^+ - Kr$ follow the trend of experimental data by Rudd et al. [123]. For impact energy above 30 keV, and a good agreement is observed, but below this energy, the results tend to lose agreement by underestimating the experimental data. In the case of $H^+ - Xe$, no experimental data exist. However, the strong agreement of the CTMC results with reference data for targets Ne, Ar, and Kr indicates the acceptability of the results for the $H^+ - Xe$ system.

3.6.3 Single differential cross sections (SDCS) of ionisation

Figures 3.26 and 3.27 show the energy and angular single differential cross section (SDCS) of ejected electrons from noble gases in the interaction with protons (H^+), The SDCS is presented at impact energy of 35 keV, with only the outer shells are considered.

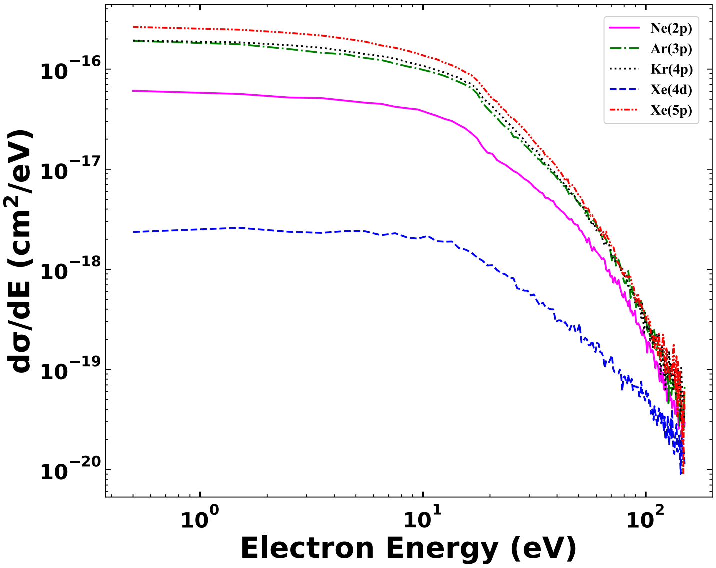

Figure 3.26 Energy single differential cross of the ejected electron from noble gases in the interaction of 35 keV protons (H^+). The SDCSs are function of the ejected electrons' energy. Magenta solid line: $Ne(2p)$, green dashed-dotted line: $Ar(3p)$, black dotted line: $Kr(4p)$, blue dashed line: $Xe(4d)$, red dashed-two-dots line: $Xe(5d)$.

In figure 3.26, The single differential cross section is plotted as a function of electron energy. The patterns of single differential cross sections (SDCS) for all targets are highly indistinguishable, but they have different values. This can be attributed to the projectile charge. Unlike the projectile previously discussed research of the interaction of Na^+ with noble gases, here the projectile is a proton, hence, the charge of the projectile is fixed at all interaction separations. The cross sections are stacked based on the binding energies of the targets, Xe(4d) having the highest binding energy has the lowest cross section, while Xe(5p) has the highest cross section due having the lowest binding energy. The SDCS curves of Ar(3p) and Kr(4p) are almost tangles due to their close binding energies. Notably, below around 20 eV, all targets maintain horizontal lines indicating constant values. However, beyond 20 eV, all cross sections experience a sudden drop, and all lines converge at energy larger than 100 eV.

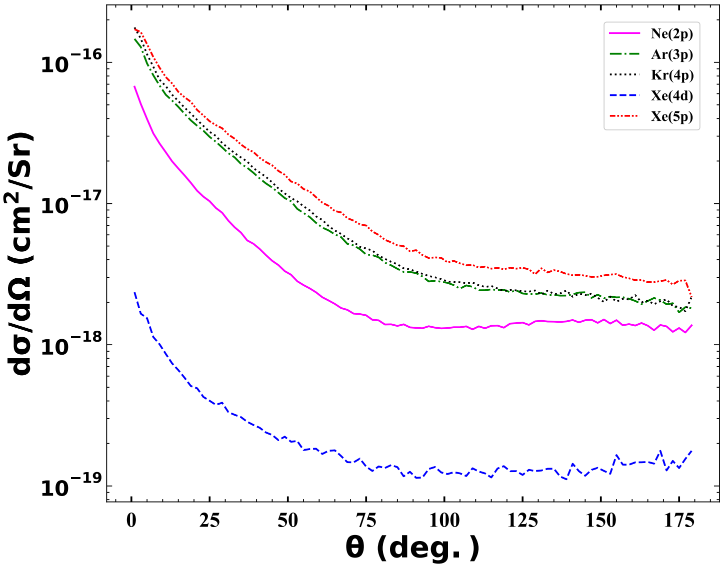

Figure 3.27 Energy single differential cross of the ejected electron from noble gases in the interaction of 35 keV protons (H^+). The SDCSs are function of the ejected electrons' scattering angle. Magenta solid line: $Ne(2p)$, green dashed-dotted line: $Ar(3p)$, black dotted line: $Kr(4p)$, blue dashed line: $Xe(4d)$, red dashed-two-dots line: $Xe(5d)$.

In figure 3.27, The single differential cross section is plotted as a function of the scattering angles of the ionised electrons. As discussed earlier, the cross section curves are stacked based on their binding energies. The cross section of all targets starts high at small angles, followed by a drastic fall until the lines reach an angle of 90°. In the backscattering above 90°, Ar(3p), Kr(4p), and Xe(5p) experience small gradual decrease, while Ne(2p) and Xe(4d) seems to maintain fixed values on average.

3.6.4 Double differential cross sections (DDCS) of ionisation

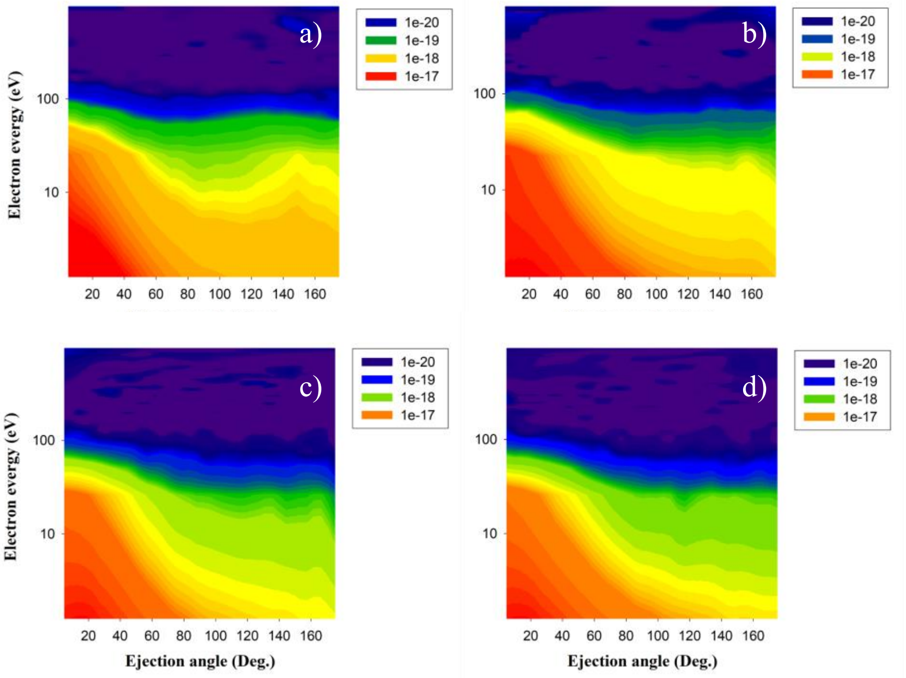

Figure 3.28 Contour plot of DDCS of ionisation process as a function of scattering angle and ejection energy of the ionised electron in the collision 35 keV protons (H^{+}) with, a) $Ne(2p)$, b) $Ar(3p)$, c) $Kr(4p)$, d) $Xe(5p)$.

Figure 3.28 illustrates the contour of double differential cross section (DDCS) as a function of ionised electron's energy and scattering angle in the collision of 35 keV protons (H^{+}) with the outer shells of Ne, Ar, Kr and Xe. For the four targets, the maximum values of DDCS are acquired at low electrons' energies and scattering angles, (approximately, $E_e \leq 20\ eV, \theta \leq 80^{o}$), i.e., forward scattering is dominant. The double differential cross sections (DDCS) diminish for electrons ejected with energies exceeding 100 eV for all angles. In figures 3.29 and 3.30 presents the energy distribution of the double differential cross section at specific angles. In figure 3.31, the energy distribution of the double differential cross section at specific energy ranges is presented.

Figure 3.29 displays the dependence of the DDCS on the energy of the ionised electron categorised based on the target. The DDCSs are calculated at protons energies of 35 keV at selected ejection angles, namely, 30^{o}, 60^{o}, 90^{o}, 120^{o} and 150^{o}, with $\pm 15^{o}$ range. The general trend for all targets, the highest cross sections (DDCS) occur in the forward scattering, especially the scattering angle 30^{o}. Additionally, the cross section for scattering angles of 120^{o} and 150^{o} are nearly equal. For the targets Ar(3p), Kr(4p) and Xe(5p), the cross sections are the lowest at these angles spanning over all energy ranges. This is true for the case of Ne(2p) only below electron energy of 20 eV, above this energy, the cross sections at ejection angles of 60^{o} and 90^{o} become the lowest, moreover, these cross sections become equal as well.

Figure 3.30 displays the dependence of the DDCS on the energy of the ionised electron categorised based on the scattering angles. Figure 3.30(a) shows the double differential cross section at scattering angle of 30^{o}. The cross section (DDCS) of Ne(2p) is the lowest among all targets over the entire energy range. The cross sections of Ar(3p) and Kr(4p) are nearly identical with slight difference, the cross section of Xe(5p) is not far from with slight overestimation. Notably, all cross sections (DDCS) at this scattering angle show fixed values for electron with energy under 10 eV, beyond the energy, the cross sections fall sharply. Figure 3.30(b) shows the double differential cross section at scattering angle of 60°. The patterns of cross sections at this angle are relatively similar to the cross sections at scattering angle of 30°, however, a slight difference in which the cross sections start decreasing from the beginning, but steadily.

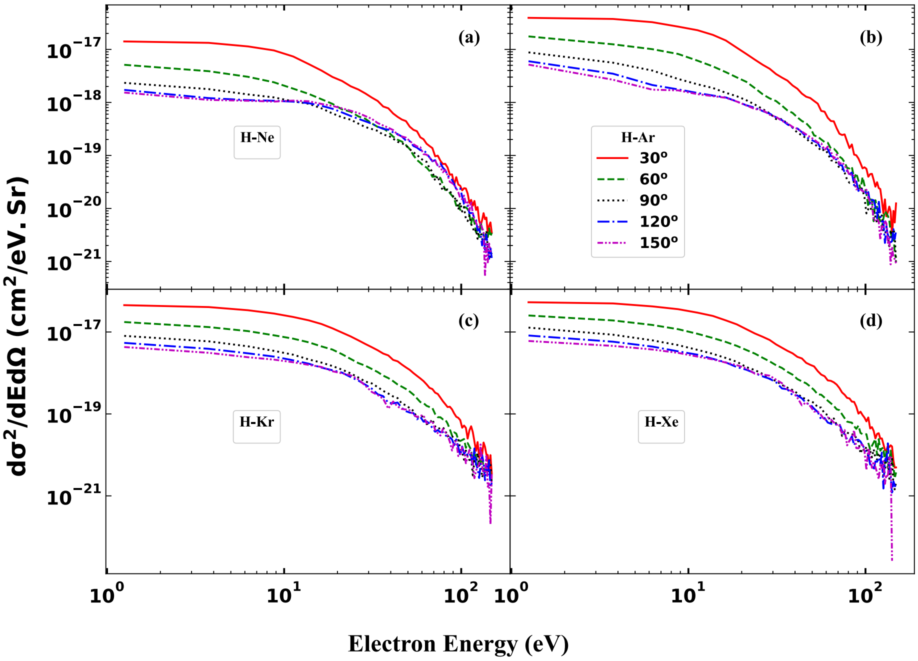

Figure 3.29 DDCS of ionisation of the outermost electron of **a)** Ne(2p), **b)** Ar(3p), **c)** Kr(4p) and **d)** Xe(5p) by 35 keV protons (H^+). The DDCS is a function of electron energy. Scattering angles; red solid line: 30^o, green dashed line: 60^o, black dotted line: 90^o, blue dashed-dotted line: 120^o, and magenta dashed-two-dots line: 150^o.

Figure 3.30(c) shows the double differential cross section at scattering angle of 90°. The patterns of cross sections of Ar(3p), Kr(4p) and Xe(5p) at this angle are nearly identical to their counterparts at scattering angle of 60° under 40 eV. Moreover, the cross section of Ne(2p) is less steep compared to the cross section at 60°. Beyond 40 eV, the cross sections of all targets mix up and become relatively equal.

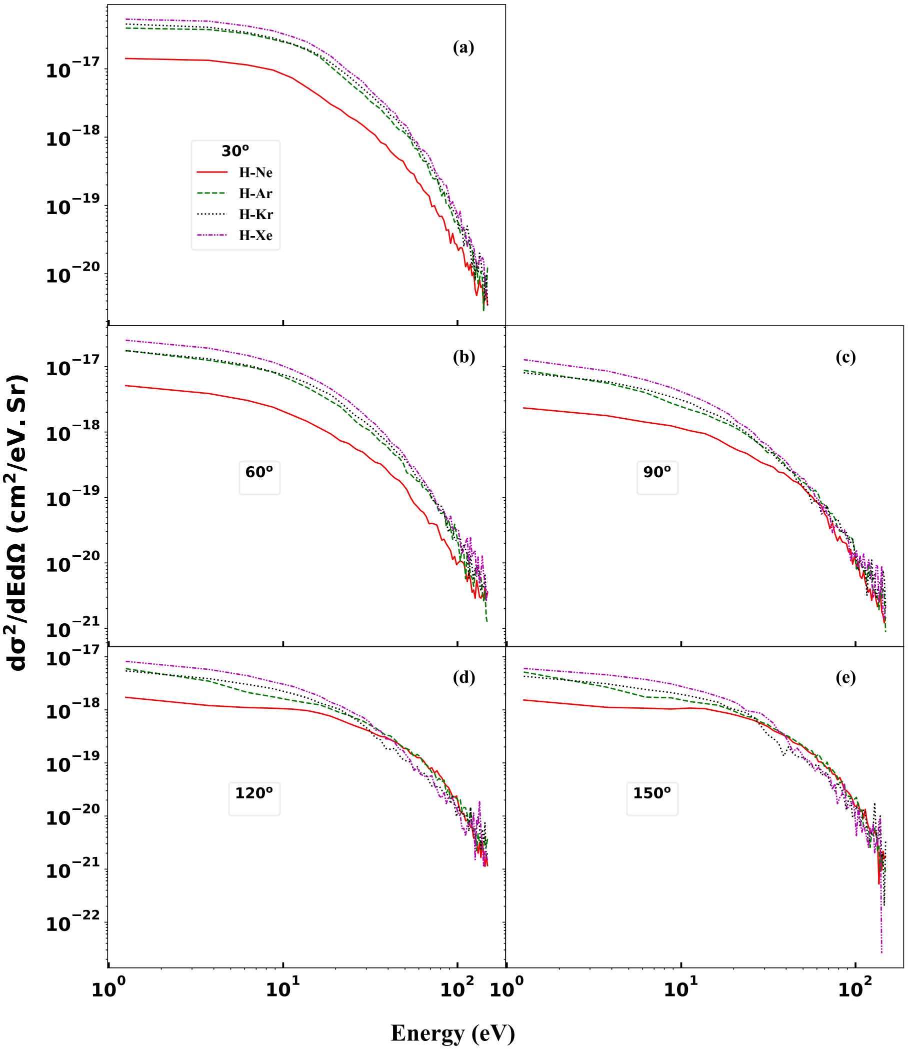

Figure 3.30 DDCS of ionisation of the outermost electron at scattering angles of **a)** 30^o, **b)** 60^o, **c)** 90^o, **d)** 120^o and **e)** 150^o by 35 keV protons (H^+). The DDCS is a function of electron energy. The targets; red solid line: $Ne(2p)$, green dashed line: $Ar(3p)$, black dotted line: $Kr(4p)$, and magenta dashed-two-dots line: $Xe(5p)$.

Figures 3.30(d) and 3.30(e) show the double differential cross section at scattering angle of 120° and 150°, respectively. For both angles, the cross sections (DDCS) are highly similar for the same target. Under 20 eV, the cross section of Ne(2p) is nearly fixed. Moreover, under 40 eV, the cross sections of Ne(2p) and Ar(3p) are smaller than the cross sections of Kr(4p) and Xe(5p), however, between 40 eV and 100 eV, the cross sections of Ne(2p) and Ar(3p) larger now. Over 100 eV, the cross sections for all targets mix up and become nearly equal.

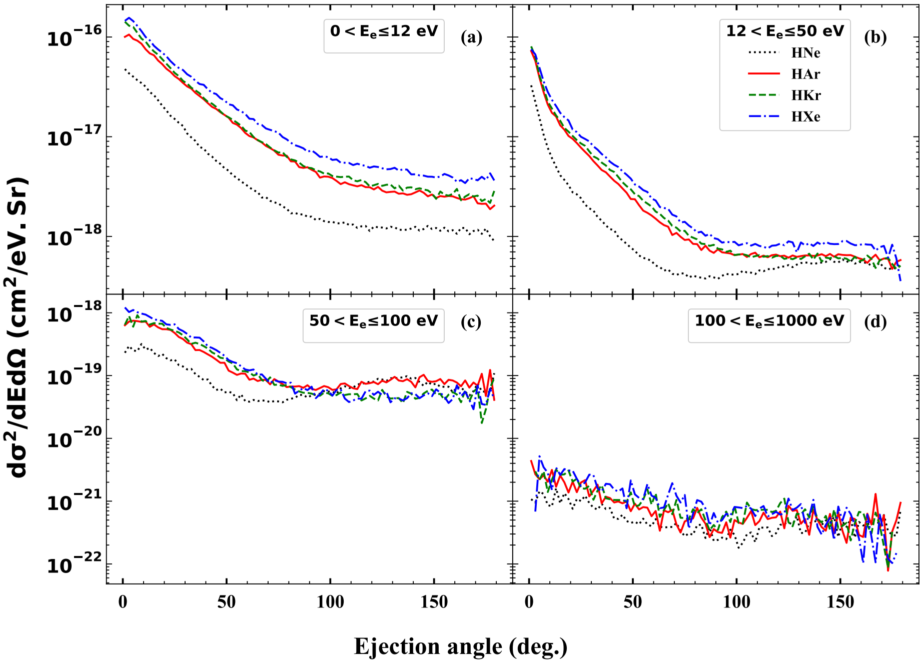

Figure 3.31 DDCS of ionisation of the outermost electron at ejection energy of **a)** $0 < E_e \leq 12\, eV$, **b)** 12$< E_e \leq 50\, eV$, **c)** $50 < E_e \leq 100\, eV$, and **d)** $100 < E_e \leq 1000\, eV$ by 35 keV protons (H^+). The DDCS is a function of scattering angle of the electron. The targets; black dotted line: $Ne(2p)$, red solid line: $Ar(3p)$, green dashed line: $Kr(4p)$, and blue dashed-dotted line: $Xe(5p)$.

Figure 3.31 displays the dependence of the double differential cross section (DDCS) on the scattering angle of the ionised electron. For This analysis, DDCSs are calculated at impact energies 35 keV at selected electrons energies, namely, $0 < E_e \leq 12\, eV$, $12 < E_e \leq 50\, eV$, $50 < E_e \leq 100\, eV$ and $100 < E_e \leq 1000\, eV$. Figure 3.31(a) present the Angular DDCS for electron energies below 12 eV. The cross section (DDCS) lines for all targets show similar trend, they start high followed by a sharp fall until reaching right scattering angles. Beyond 90°, the cross section lines show insignificant decrease. The cross section of Xe(5p) is the highest while Ne(2p) is the lowest. The cross sections of Ar(3p) and Kr(4p) are highly identical.

In Figure 3.31(b), the Angular DDCSs for electron energies in the range $12 < E_e \leq 50\ eV$ are presented. Like the case $0 < E_e \leq 12\ eV$ in 3.31(a), the cross section (DDCS) lines for all targets start high followed by a sharp fall until reaching right scattering angles, however, the fall is sharper compared to the lower energy. The cross sections of Ar(3p), Kr(4p) and Xe(5p) follow the same trend, after the sharp fall, they maintain approximately constant values. On the other hand, the cross section of Ne(2p) experiences a minimum at right angle scattering, above 90^o, the cross section experiences a slight increase.

In Figure 3.31(c), the Angular DDCSs for electron energies in the range $50 < E_e \leq 100\ eV$ are presented. At this energy range, the cross sections (DDCS) are smaller compared to their counterparts at lower electrons energies ranges. In the forward scattering, the cross sections of Ar(3p), Kr(4p) and Xe(5p) are nearly equal, while the cross section of Ne(2p) is lower. The cross section lines of all these targets intersect at an angle around 100^o, above this angle, the cross sections of Kr(4p) and Xe(5p) are approximately equal and experience fluctuations, however, the average cross sections seem constant. However, the cross sections of Ne(2p) and Ar(3p) becomes equal and experience a slight increase.

In Figure 3.31(d), the Angular DDCSs for electron energies in the range $100 < E_e \leq 1000\ eV$ are presented. At this energy range, the cross sections (DDCS) are the lowest compared to their counterparts at lower electrons energies ranges. The cross sections of all targets experience high fluctuations and are now tangled, especially in the back scattering region.

In the forward scattering region, the cross sections of Ne(2p) and Xe(5p) are the lowest and highest with small margins.

Summary

The inelastic electron processes in ion-atom collisions have great significance in many fields of science, such as particle beam therapy and fusion plasma physics. Among electron processes, ionisation has a great influence in radiation physics, atomic and molecular structure exploration, and modelling and diagnosing the magnetically confined fusion plasmas in tokamak reactors. The dissertation focuses on the collision of singly charged ions with neutral atomic impurities in plasma. The collision systems studied in the dissertation are composed of projectiles of proton, lithium, and sodium ions and atomic targets of nitrogen and noble gases, i.e. He, Ne, Ar, Kr and Xe. Studying the cross sections of these collision systems is essential due to their potential applications in the diagnostic of magnetically confined fusion plasmas.

During my PhD studies I used the 3-body Classical Trajectory Monte Carlo (CTMC) method, following its historical development from collinear molecular reactions to its adaptation for ion-atom collisions. The 3-body CTMC approach, a non-perturbative computational technique, is developed for a comprehensive understanding of collision dynamics. Within our CTMC model, the collision system is reduced to a three-body problem by employing the single active electron (SAE) approximation. I presented a discussion of the Garvey-type distance-dependent model potential [73] based on Green et al.'s work [76], the Hamiltonian of the collision system, and equations of motion. The initial conditions of the projectile and the active electron of the target are determined according to the Reinhold and Falcon's methodology [83]. The cross-section calculations include total cross-sections of electron capture and ionisation channels, as well as the differential cross-sections for ionisation channel.

I provided an extensive discussion of nuclear-nuclear interactions, shell contributions, and the impact parameter probabilities of ionisation and charge exchange channels. For instance, the role of nuclear-nuclear interaction (V_{TP}, see Figure 2.1) in $Li^{+} - He$ collision is examined, providing that the cross section change is hardly visible with and without taken into account this interaction. The contribution of inner electron shells in $H^{+} - Xe$ collisions is analysed, showing distinct patterns for various electron shells. Moreover, it shows insignificance of the contribution of most of the shells. Probabilities of ionisation and electron capture are investigated, exhibiting Gaussian-like shapes with shifting peak positions concerning impact energy.

I performed CTMC calculations of $Li^{+} - He$ and $Li^{+} - N$ collision systems. I calculated the ionization and electron capture total cross sections as a function of the impact energy in the range (20 keV-100 MeV), I also determined the impact parameter dependent probabilities. I found excellent agreement with the previous data.

I performed CTMC calculations of $Na^{+} - N$ collision systems. I calculated the ionisation total cross sections as a function of the projectile energy in the range between 10 keV and10 MeV. The calculations showed the insignificance contribution of inner shell at low energies, and how they become more important as the impact energy increases. Moreover, I calculated the ionisation differential cross sections for impact energies of 30, 40, 50 and 60 keV as a function of the scattering angle and the energy of the ionised electron, these energies are in the suitable range for diagnosis plasma in tokamak. Furthermore, contour plots of double differential cross sections (DDCS) reveal distinct patterns at different impact energies and scattering angles, with a noticeable Fermi shuttle-type ionization process. This study focuses on the role of the impact energy on the differential cross section for the same system. I found that the majority of electrons are ejected at lower angles followed by backscattered electrons, moreover, the majority of these electrons acquire kinetic energies of 20 eV and below.

I studied the collision of singly charged sodium (Na^+) with atomic noble gases i.e., neon, argon, krypton, and xenon. I performed calculations of the ionisation and electron capture total cross sections as a function of the projectile energy in the energy range between 10 keV and 50 MeV. Moreover, I calculated the ionisation differential cross sections for impact energy of 60 keV as a function of the scattering angle and the energy of the ionised electron. An extensive discussion is provided for these collision systems. This study focuses on the role of the type of the target on the differential cross section at the same impact energy. I found that electrons with energies below 10 eV are dominant in the forward scattering. Moreover, for 12 eV electrons, the DDCSs of backscattering and scattering at 90° show relatively identical results. I found that the backscattering DDCS was greater than the scattering DDCS at 90° for both Ne(2p) and Ar(3p) at electron energies larger than 12 eV. Furthermore, I found that the backscattering DDCS for Kr(4p) and Xe(5p) was greater than at scattering of 90° with energies larger than 50 eV.

I studied the collision of protons with noble gases i.e., neon, argon, krypton, and xenon. I performed calculations of the ionisation and electron capture total cross sections as a function of the projectile energy in the range (0.2 keV-50 MeV). Moreover, I calculated the ionisation differential cross sections for impact energy 35 of keV as a function of the scattering angle and the energy of the ionised electron. In comparing with experimental and theoretical data, I found excellent agreement regarding the total cross section data.

Összefoglaló

Az ion-atom ütközések rugalmatlan elektronfolyamatai nagy jelentőséggel bírnak számos területen, például a részecskesugár terápiában és a fúziós plazmafizikában. Az elektronfolyamatok közül az ionizáció nagy hatással van a sugárzásfizikára, az atom-és molekulaszerkezetek feltárására, valamint a mágnesesen zárt fúziós plazmák modellezésére és diagnosztizálására a tokamak reaktorokban. A disszertáció az egyszeres töltésű ionok és a fúziós plazmában előforduló semleges atomszennyeződésekkel való ütközési folyamatok hatáskeresztmetszeteinek számításaira összpontosít. A disszertációban vizsgált ütközési rendszerek proton, lítium- és nátriumionok lövedékeiből, valamint nitrogén-és nemesgázok atomi célpontjaiból állnak. Ezeknek az ütközési rendszereknek a keresztmetszeteinek tanulmányozása elengedhetetlen a mágnesesen zárt fúziós plazmák diagnosztikájában való potenciális alkalmazásuk miatt.

A PhD tanulmányaim során a 3-test klasszikus pályájú Monte Carlo (classical trajectory Monte Carlo (CTMC)) módszert alkalmaztam, követve annak történeti fejlődését a kollineáris molekuláris reakcióktól az ion-atom ütközésekhez való alkalmazkodásig. A 3 testes CTMC megközelítést, egy nem perturbatív számítási technika, mely az ütközésben résztvevő részecskék átfogó ütközés dinamikai megértését segíti. A CTMC modellen belül az ütközési rendszert háromtest közelítésben használtam, melyben a célatom egyetlen aktív elektronját vettük figyelembe (egy aktív elektron (SAE) közelítés). A többelektronos rendszet a Garvey-típusú távolságfüggő modell potenciál segítségével írtam le [73], le ami Green és munkatársainak munkája alpján lett kifelejlesztve [76], A PhD disszertációban bemutatom a ütközési rendszer

Hamiltonianját az abből levezethető klasszikus mozgásegyenleteket. A lövedék és a céltárgy aktív elektronjának kezdeti állapotát Reinhold és Falcon által javasolt eljárással határoztam meg [83]. A hatáskeresztmetszeti számítások tartalmazzák az elektron-befogási és ionizációs csatornák teljes keresztmetszetét, valamint az ionizációs csatorna differenciális keresztmetszetét.

Vizsgáltam a mag-mag kölcsönhatás és az alhéjek hozzájárulását az elektronikus folyamat hatáskeresztmetszeteihez. Meghatároztam az ionizaciós és elektronbefogási csatornák ütközési paramétertől való függését. Például megvizsgáltam a mag-mag kölcsönhatás szerepét a $Li^+ - He$ ütközésben. Elemeztem a belső elektronhéjak hozzájárulását a teljes ütközési hatáskeresztmetszetekhez $H^+ - Xe$ ütközésekben. Vizsgáltam az ionizáció és az elektronbefogási csatornák ütközési paramétertől való függését. Ezek jó közelítésben Gauss-szerű alakot mutatnak, amelyek az ütközési energia függvényében változó csúcspozíciókkal rendelkeznek.

CTMC közelítésben meghatároztam a $Li^+ - He$ és $Li^+ - N$ ütközési rendszerek hatáskeresztmetszeteit. 20 keV és 100 MeV közötti ütközési energiákra kiszámoltam az ionizációs és elektron-befogási teljes hatáskeresztmetszeteket. Meghatároztam az ütközési paraméterfüggő valószínűségeket is. Kiváló egyetértést találtam a korábbi adatokkal.

CTMC közelítésben meghatároztam a $Na^+ - N$ ütközési rendszerek hatáskeresztmetszeteit. 10 keV és 10 MeV lövedék energiatartományban kiszámoltam az ionizációs csatorna teljes hatáskeresztmetszetét. A számítások azt is megmutatták, hogy a belső héj jelentéktelen mértékben járul hozzá a teljes hatáskeresztmetszetekhez alacsonyabb lövedék energiáknál. Nagyobb lövedék energiák esetében azonben a belső héjak járuléke egyre nagyobb. Kiszámoltam a 30, 40, 50 és 60 keV ütközési energiákhoz tartozó ionizációs differenciális keresztmetszeteket a szórási szög és az ionizált elektron energiájának függvényében. Azért valasztottuk ezeket az energiákat, mert ezek azok az energiák, amiket tokamak diagnosztikai vizsgálataira használnak. Megmutattuk, hogy a kétszeresen differenciális hatáskeresztmetszetek kontúrdiagramjai különböző ütközési energiákon és szórási szögeken eltérő mintákat mutatnak. Észrevehető a Fermi típusú gyorsitási mechanizmus jellegzetes csúcsai is. Megállapítottam, hogy a kilépő elektronok többsége alacsonyabb szögben jelenik meg, és ezen elektronok többsége 20 eV vagy annál alacsonyabb kinetikus energiával rendelkeznek.

Tanulmányoztam az egyszeres töltésű nátrium ion (Na^+) atomi nemesgázokkal, azaz neonnal, argonnal, kriptonnal és xenonnal való ütközését. 10 keV és 50 MeV közötti lövedék energiákra elvégeztem az ionizációs és elektron-befogási teljes keresztmetszetek számítását. Ezen felül 60 keV-os ütközési energiára kiszámítottam az differenciális ionizációs hatáskeresztmetszeteket a szórási szög és az ionizált elektron energiájának függvényében. Megállapítottam, hogy a 10 eV alatti energiájú elektronok dominálnak az előszórásban. Megmutattam, hogy a 12 eV-es elektronok esetében a visszaszórás valamint a 90° szórás kétszeresen differenciális hatáskeresztmetszetei azonosak.

Tanulmányoztam a protonok ütközését nemesgázokkal, azaz neonnal, argonnal, kriptonnal és xenonnal. Elvégeztem az ionizációs és elektron-befogási teljes keresztmetszetek számítását a lövedék energiájának függvényében a tartományban 0,2 keV és 50 MeV energiatartományban. Ezen felül kiszámítottam a 35 keV ütközési energia ionizációs differenciális keresztmetszetét a szórási szög és az ionizált elektron energiájának függvényében. A kísérleti és elméleti adatokkal összevetve kiváló egyezést találtam a teljes keresztmetszeti adatok tekintetében.

Acknowledgement

This work has been carried out within the framework of the EURO fusion Consortium, funded by the European Union via the Euratom Research and Training Programme (Grant Agreement No. 101052200—EURO fusion). Views and opinions expressed are however those of the author(s) only and do not necessarily reflect those of the European Union or the European Commission. Neither the European Union nor the European Commission can be held existingible for them.

I would like to express my deepest appreciation to everyone who helped me through my study. Word cannot express my gratitude to my supervisor Prof. Dr. Károly Tőkési for directing my study.

I would like to thank my wife Manar, my father, my mother and my brothers and sisters and all my family for their support and believing in me, their support motivated me during my study.

Bibliography

1. Newhauser, W.D.; Zhang, R. The Physics of Proton Therapy. *Phys. Med. Biol.* **2015**, *60*, R155–R209, doi:10.1088/0031-9155/60/8/R155.
2. Schardt, D.; Elsässer, T.; Schulz-Ertner, D. Heavy-Ion Tumor Therapy: Physical and Radiobiological Benefits. *Rev. Mod. Phys.* **2010**, *82*, 383–425, doi:10.1103/RevModPhys.82.383.
3. XXII. The Penetration of Atomic Particles Through Matter. In *The Penetration of Charged Particles through Matter (1912–1954)*; Jens Thorsen, Ed.; Niels Bohr Collected Works; Elsevier, 1987; Vol. 8, pp. 423–568 ISBN 978-0-444-87003-2.
4. Kruezi, U.; Stoschus, H.; Schweer, B.; Sergienko, G.; Samm, U. Supersonic Helium Beam Diagnostic for Fluctuation Measurements of Electron Temperature and Density at the Tokamak TEXTOR. *Rev. Sci. Instrum.* **2012**, *83*, 065107, doi:10.1063/1.4707150.
5. Bandyopadhyay, I.; Barbarino, M.; Bhattacharjee, A.; Eidietis, N.; Huber, A.; Isayama, A.; Kim, J.; Konovalov, S.; Lehnen, M.; Nardon, E.; et al. Summary of the IAEA Technical Meeting on Plasma Disruptions and Their Mitigation. *Nucl. Fusion* **2021**, *61*, 077001, doi:10.1088/1741-4326/abfe76.
6. Hollmann, E.M.; Aleynikov, P.B.; Fülöp, T.; Humphreys, D.A.; Izzo, V.A.; Lehnen, M.; Lukash, V.E.; Papp, G.; Pautasso, G.; Saint-Laurent, F.; et al. Status of Research toward the ITER Disruption Mitigation System. *Phys. Plasmas* **2015**, *22*, 021802, doi:10.1063/1.4901251.
7. Bakhtiari, M.; Tamai, H.; Kawano, Y.; Kramer, G.J.; Isayama, A.; Nakano, T.; Kamiya, Y.; Yoshino, R.; Miura, Y.; Kusama, Y.; et al. Study of Plasma Termination Using High- Z Noble Gas Puffing in the JT-60U Tokamak. *Nucl. Fusion* **2005**, *45*, 318–325, doi:10.1088/0029-5515/45/5/002.
8. Lehnen, M.; Alonso, A.; Arnoux, G.; Baumgarten, N.; Bozhenkov, S.A.; Brezinsek, S.; Brix, M.; Eich, T.; Gerasimov, S.N.; Huber, A.; et al. Disruption Mitigation by Massive Gas Injection in JET. *Nucl. Fusion* **2011**, *51*, 123010, doi:10.1088/0029-5515/51/12/123010.
9. Manas, P.; Kappatou, A.; Angioni, C.; McDermott, R.M.; ASDEX Light Impurity Transport in Tokamaks: On the Impact of Neutral Beam Fast Ions. *Nucl. Fusion* **2020**, *60*, 056005, doi:10.1088/1741-4326/ab77e8.
10. Shiraki, D.; Commaux, N.; Baylor, L.R.; Eidietis, N.W.; Hollmann, E.M.; Lasnier, C.J.; Moyer, R.A. Thermal Quench Mitigation and Current Quench Control by Injection of Mixed Species Shattered Pellets in DIII-D. *Phys. Plasmas* **2016**, *23*, 062516, doi:10.1063/1.4954389.
11. Whyte, D.G.; Jernigan, T.C.; Humphreys, D.A.; Hyatt, A.W.; Lasnier, C.J.; Parks, P.B.; Evans, T.E.; Taylor, P.L.; Kellman, A.G.; Gray, D.S.; et al. Disruption Mitigation with High-Pressure Noble Gas Injection. *J. Nucl. Mater.* **2003**, *313–316*, 1239–1246, doi:10.1016/S0022-3115(02)01525-8.
12. Morozov, D.K.; Yurchenko, E.I.; Lukash, V.E.; Baronova, E.O.; Pozdnyakov, Yu.I.; Rozhansky, V.A.; Senichenkov, I.Y.; Veselova, I.Y.; Schneider, R. Mechanisms of Disruptions Caused by Noble Gas Injection into Tokamak Plasmas. *Nucl. Fusion* **2005**, *45*, 882–887, doi:10.1088/0029-5515/45/8/015.
13. Brooks, J.N. Analysis of Noble Gas Recycling at a Fusion Plasma Divertor. *Phys. Plasmas* **1996**, *3*, 2286–2292, doi:10.1063/1.871911.
14. Pusztai, I.; Pokol, G.; Dunai, D.; Réfy, D.; Pór, G.; Anda, G.; Zoletnik, S.; Schweinzer, J. Deconvolution-Based Correction of Alkali Beam Emission

Spectroscopy Density Profile Measurements. *Rev. Sci. Instrum.* **2009**, *80*, 083502, doi:10.1063/1.3205930.

15. Brix, M.; Dodt, D.; Dunai, D.; Lupelli, I.; Marsen, S.; Melson, T.F.; Meszaros, B.; Morgan, P.; Petravich, G.; Refy, D.I.; et al. Recent Improvements of the JET Lithium Beam Diagnostic. *Rev. Sci. Instrum.* **2012**, *83*, 10D533, doi:10.1063/1.4739411.
16. Anda, G.; Dunai, D.; Lampert, M.; Krizsanóczi, T.; Németh, J.; Bató, S.; Nam, Y.U.; Hu, G.H.; Zoletnik, S. Development of a High Current 60 keV Neutral Lithium Beam Injector for Beam Emission Spectroscopy Measurements on Fusion Experiments. *Rev. Sci. Instrum.* **2018**, *89*, 013503, doi:10.1063/1.5004126.
17. Réfy, D.I.; Brix, M.; Gomes, R.; Tál, B.; Zoletnik, S.; Dunai, D.; Kocsis, G.; Kálvin, S.; Szabolics, T.; JET Contributors Sub-Millisecond Electron Density Profile Measurement at the JET Tokamak with the Fast Lithium Beam Emission Spectroscopy System. *Rev. Sci. Instrum.* **2018**, *89*, 043509, doi:10.1063/1.4986621.
18. Zoletnik, S.; Anda, G.; Aradi, M.; Asztalos, O.; Bató, S.; Bencze, A.; Berta, M.; Demeter, G.; Dunai, D.; Hacek, P.; et al. Advanced Neutral Alkali Beam Diagnostics for Applications in Fusion Research (Invited). *Rev. Sci. Instrum.* **2018**, *89*, 10D107, doi:10.1063/1.5039309.
19. Zoletnik, S.; Hu, G.H.; Tál, B.; Dunai, D.; Anda, G.; Asztalos, O.; Pokol, G.I.; Kálvin, S.; Németh, J.; Krizsanóczi, T. Ultrafast Two-Dimensional Lithium Beam Emission Spectroscopy Diagnostic on the EAST Tokamak. *Rev. Sci. Instrum.* **2018**, *89*, 063503, doi:10.1063/1.5017224.
20. Isler, R.C.; Crume, E.C.; Horton, L.D.; Murakami, M.; Baylor, L.R.; Bell, G.L.; Bigelow, T.S.; England, A.C.; Glowienka, J.C.; Jernigan, T.C.; et al. Radiative Losses and Improvement of Plasma Parameters after Gettering in the Advanced Toroidal Facility. *Nucl. Fusion* **1991**, *31*, 245–259, doi:10.1088/0029-5515/31/2/003.
21. Hemsworth, R.; Decamps, H.; Graceffa, J.; Schunke, B.; Tanaka, M.; Dremel, M.; Tanga, A.; De Esch, H.P.L.; Geli, F.; Milnes, J.; et al. Status of the ITER Heating Neutral Beam System. *Nucl. Fusion* **2009**, *49*, 045006, doi:10.1088/0029-5515/49/4/045006.
22. Patel, M.; Thomas, J.; Joshi, H.C. Flow Characterization of Supersonic Gas Jets: Experiments and Simulations. *Vacuum* **2021**, *192*, 110440, doi:10.1016/j.vacuum.2021.110440.
23. Yuan, B.D.; Yu, Y.; He, R.C.; Yang, X.Y.; Xu, T.C.; Yuan, J.B.; Hong, R.J.; Nie, L.; Ke, R.; Long, T.; et al. Development of a Multi-Color Gas Puff Imaging Diagnostic on HL-2A Tokamak. *Rev. Sci. Instrum.* **2020**, *91*, 073505, doi:10.1063/5.0005545.
24. Dimitriou, K.; Aumayr, F.; Katsonis, K.; Winter, H. H+–He(1s2) Collisions: CTMC Calculations of Single Ionisation and Excitation Cross Sections. *Int. J. Mass Spectrom.* **2004**, *233*, 137–144, doi:10.1016/j.ijms.2003.12.014.
25. Brañas, B.; Tafalla, D.; Tabarés, F.L.; Ortiz, P. Atomic Beam Diagnostics for Characterization of Edge Plasma in TJ-II Stellarator. *Rev. Sci. Instrum.* **2001**, *72*, 602–606, doi:10.1063/1.1319868.
26. Schmid, K.; Manhard, A.; Linsmeier, Ch.; Wiltner, A.; Schwarz-Selinger, T.; Jacob, W.; Mändl, S. Interaction of Nitrogen Plasmas with Tungsten. *Nucl. Fusion* **2010**, *50*, 025006, doi:10.1088/0029-5515/50/2/025006.
27. Bell, M.G.; Kugel, H.W.; Kaita, R.; Zakharov, L.E.; Schneider, H.; LeBlanc, B.P.; Mansfield, D.; Bell, R.E.; Maingi, R.; Ding, S.; et al. Plasma Response to Lithium-Coated Plasma-Facing Components in the National Spherical Torus Experiment.

Plasma Phys. Control. Fusion **2009**, *51*, 124054, doi:10.1088/0741-3335/51/12/124054.

28. Canik, J.M.; Guttenfelder, W.; Maingi, R.; Osborne, T.H.; Kubota, S.; Ren, Y.; Bell, R.E.; Kugel, H.W.; LeBlanc, B.P.; Souhkanovskii, V.A. Edge Microstability of NSTX Plasmas without and with Lithium-Coated Plasma-Facing Components. *Nucl. Fusion* **2013**, *53*, 113016, doi:10.1088/0029-5515/53/11/113016.
29. Lyublinski, I.; Vertkov, A.; Mirnov, S.; Lazarev, V. Protection of Tokamak Plasma Facing Components by a Capillary Porous System with Lithium. *J. Nucl. Mater.* **2015**, *463*, 1156–1159, doi:10.1016/j.jnucmat.2014.12.017.
30. Wolfrum, E.; Schweinzer, J.; Bridi, D.; Igenbergs, K.; Kamleitner, J.; Aumayr, F. A Sodium (Na) Beam Edge Diagnostic. *Proc. 18th Int. Conf. Plasma-Surf. Interact. Control. Fusion Device* **2009**, *390–391*, 1110–1113, doi:10.1016/j.jnucmat.2009.01.282.
31. Kaganovich, I.D.; Startsev, E.A.; Davidson, R.C.; Kecskemeti, S.R.; Bin-Nun, A.; Mueller, D.; Grisham, L.; Watson, R.L.; Horvat, V.; Zaharakis, K.E.; et al. Ionization Cross-Sections for Ion–Atom Collisions in High-Energy Ion Beams. *Nucl. Instrum. Methods Phys. Res. Sect. Accel. Spectrometers Detect. Assoc. Equip.* **2005**, *544*, 91–97, doi:10.1016/j.nima.2005.01.198.
32. Zapukhlyak, M.; Kirchner, T. Projectile Angular-Differential Cross Sections for Electron Transfer Processes in Ion-Helium Collisions: Evidence for the Applicability of the Independent Electron Model. *Phys. Rev. A* **2009**, *80*, 062705, doi:10.1103/PhysRevA.80.062705.
33. Samanta, R.; Purkait, M.; Mandal, C.R. Single-Electron-Capture Processes in Collisions of He 2 + , Li q + (q = 1 , 2 , 3) , C 6 + , and O 8 + Ions with Helium. *Phys. Rev. A* **2011**, *83*, 032706, doi:10.1103/PhysRevA.83.032706.
34. Woitke, O.; Závodszky, P.A.; Ferguson, S.M.; Houck, J.H.; Tanis, J.A. Target Ionization and Projectile Charge Changing in 0.5 – 8 − MeV / q Li q + + He (q = 1 , 2 , 3) Collisions. *Phys. Rev. A* **1998**, *57*, 2692–2700, doi:10.1103/PhysRevA.57.2692.
35. Al-Ajaleen, M.S.A.; Taoutioui, A.; Tokesi, K. Charge Transfer and Ionisation Cross-Sections in Collisions of Singly Charged Lithium Ions with Helium and Nitrogen Atoms. *Plasma Phys. Control. Fusion* **2023**, doi:10.1088/1361-6587/acc6ed.
36. Al-Ajaleen, M.; Tőkési, K. Total and Differential Ionization Cross Sections in Collision between Nitrogen Atom and Singly Charged Sodium Ion. *Sci. Rep.* **2023**, *13*, 14080, doi:10.1038/s41598-023-41134-0.
37. Tőkési, K. State Selective Electron Capture in Low Energy Positron and Argon Collisions. *Nucl. Instrum. Methods Phys. Res. Sect. B Beam Interact. Mater. At.* **2012**, *279*, 62–65, doi:10.1016/j.nimb.2011.10.068.
38. Frémont, F.; Laurent, G.; Rangama, J.; Sobocinski, P.; Tarisien, M.; Adoui, L.; Cassimi, A.; Chesnel, J.-Y.; Fléchard, X.; Hennecart, D.; et al. Electron Capture in Collisions of Slow Highly Charged Ions with an Atom and a Molecule: Processes and Fragmentation Dynamics. *Int. J. Mol. Sci.* **2002**, *3*, 115–131, doi:10.3390/i3030115.
39. Sidky, E.Y.; Lin, C.D. Total Cross-Section Calculations on Proton-Impact Ionization of Hydrogen. *Phys. Rev. A* **2001**, *65*, 012711, doi:10.1103/PhysRevA.65.012711.
40. Massey, H.S.W.; Burhop, E.H.S.; Gilbody, H.B. *Electronic and Ionic Impact Phenomena*; International series of monographs on physics; Clarendon Press: Oxford, 1969; Vol. I;

41. Bell, K.L.; Kingston, A.E. The First Born Approximation. In *Advances in Atomic and Molecular Physics*; Elsevier, 1974; Vol. 10, pp. 53–130 ISBN 978-0-12-003810-7.
42. Bethe, H. Zur Theorie des Durchgangs schneller Korpuskularstrahlen durch Materie. *Ann. Phys.* **1930**, *397*, 325–400, doi:10.1002/andp.19303970303.
43. Yates, A.C. High-Energy Higher-Order Born Approximations: Theoretical Development. *Phys. Rev. A* **1979**, *19*, 1550–1558, doi:10.1103/PhysRevA.19.1550.
44. Dewangan, D.P. On Higher Order Born Approximations in Atomic Scattering Calculations. *J. Phys. B At. Mol. Phys.* **1980**, *13*, L595–L598, doi:10.1088/0022-3700/13/19/005.
45. Dal Cappello, C.; Haddadou, A.; Menas, F.; Roy, A.C. The Second Born Approximation for the Single and Double Ionization of Atoms by Electrons and Positrons. *J. Phys. B At. Mol. Opt. Phys.* **2011**, *44*, 015204, doi:10.1088/0953-4075/44/1/015204.
46. Crothers, D.S.F.; Dubé, L.J. Continuum Distorted Wave Methods in Ion—Atom Collisions. In *Advances In Atomic, Molecular, and Optical Physics*; Elsevier, 1992; Vol. 30, pp. 287–337 ISBN 978-0-12-003830-5.
47. Cheshire, I.M. Continuum Distorted Wave Approximation; Resonant Charge Transfer by Fast Protons in Atomic Hydrogen. *Proc. Phys. Soc.* **1964**, *84*, 89–98, doi:10.1088/0370-1328/84/1/313.
48. Gayet, R. Charge Exchange Scattering Amplitude to First Order of a Three Body Expansion. *J. Phys. B At. Mol. Phys.* **1972**, *5*, 483–491, doi:10.1088/0022-3700/5/3/013.
49. Fainstein, P.D.; Ponce, V.H.; Rivarola, R.D. A Theoretical Model for Ionisation in Ion-Atom Collisions. Application for the Impact of Multicharged Projectiles on Helium. *J. Phys. B At. Mol. Opt. Phys.* **1988**, *21*, 287–299, doi:10.1088/0953-4075/21/2/013.
50. Belkić, D. Total Cross Sections in Five Methods for Two-Electron Capture by Alpha Particles from Helium: CDW-4B, BDW-4B, BCIS-4B, CDW-EIS-4B and CB1-4B. *J. Math. Chem.* **2020**, *58*, 1133–1176, doi:10.1007/s10910-020-01123-4.
51. Igenbergs, K.; Schweinzer, J.; Aumayr, F. Charge Exchange in Be $^{4+}$ –H(*n* = 1, 2) Collisions Studied Systematically by Atomic-Orbital Close-Coupling Calculations. *J. Phys. B At. Mol. Opt. Phys.* **2009**, *42*, 235206, doi:10.1088/0953-4075/42/23/235206.
52. Fritsch, W.; Lin, C.D. The Semiclassical Close-Coupling Description of Atomic Collisions: Recent Developments and Results. *Phys. Rep.* **1991**, *202*, 1–97, doi:10.1016/0370-1573(91)90008-A.
53. Bransden, B.H.; McDowell, M.R.C. *Charge Exchange and the Theory of Ion-Atom Collisions*; Oxford science publications; Clarendon Press ; Oxford University Press: Oxford : New York, 1992; ISBN 978-0-19-852020-7.
54. Bates, D.R.; McCarroll, R. Electron Capture in Slow Collisions. *Proc. R. Soc. Lond. Ser. Math. Phys. Sci.* **1958**, *245*, 175–183, doi:10.1098/rspa.1958.0075.
55. Joseph, D.C.; Saha, B.C. Charge Exchange in Slow Collisions of Si3+ with Hydrogen Atom: Molecular-Orbital Close-Coupling Approaches in the Adiabatic Representation. In *Advances in Quantum Chemistry*; Elsevier, 2021; Vol. 84, pp. 73–94 ISBN 978-0-12-823877-6.
56. Wang, R.; Stancil, P. Molecular-Orbital Close-Coupling Calculation of 20-Chnnael H-H+ Collision. **2020**, *236*, 247.03.
57. Omidvar, K. Asymptotic Form of the Charge-Exchange Cross Section in Three-Body Rearrangement Collisions. *Phys. Rev. A* **1975**, *12*, 911–926, doi:10.1103/PhysRevA.12.911.

58. Kuang, Y.R. Model-Potential Oppenheimer-Brinkman-Kramers Approximation for *K* -Shell Electron Capture in Asymmetric Collisions. *Phys. Rev. A* **1991**, *44*, 1613–1619, doi:10.1103/PhysRevA.44.1613.
59. Kuang, Y.R. Modified Oppenheimer-Brinkman-Kramers Approximation for K-Shell Capture in Asymmetric Collisions. *J. Phys. B At. Mol. Opt. Phys.* **1991**, *24*, 4993–5001, doi:10.1088/0953-4075/24/23/025.
60. Oppenheimer, J.R. On the Quantum Theory of the Capture of Electrons. *Phys. Rev.* **1928**, *31*, 349–356, doi:10.1103/PhysRev.31.349.
61. Brinkman, H.; Kramers, H. Zur Theorie Der Einfangung von Elektronen Durch α-Teilchen.*;* 1930; Vol. 33, pp. 973–984.
62. Tőkési, K.; Barna, I.F.; Burgdörfer, J. Ionization of Helium in Positron Impact. *Nucl. Instrum. Methods Phys. Res. Sect. B Beam Interact. Mater. At.* **2005**, *233*, 307–311, doi:10.1016/j.nimb.2005.03.127.
63. Olson, R.E.; Salop, A. Charge-Transfer and Impact-Ionization Cross Sections for Fully and Partially Stripped Positive Ions Colliding with Atomic Hydrogen. *Phys. Rev. A* **1977**, *16*, 531–541, doi:10.1103/PhysRevA.16.531.
64. Abrines, R.; Percival, I.C. Classical Theory of Charge Transfer and Ionization of Hydrogen Atoms by Protons. *Proc. Phys. Soc.* **1966**, *88*, 861–872, doi:10.1088/0370-1328/88/4/306.
65. Tökési, K.; Hock, G. Versatility of the Exit Channels in the Three-Body CTMC Method. *Nucl. Instrum. Methods Phys. Res. Sect. B Beam Interact. Mater. At.* **1994**, *86*, 201–204, doi:10.1016/0168-583X(94)96177-8.
66. Burgess, A.; Percival, I.C. Classical Theory of Atomic Scattering. In *Advances in Atomic and Molecular Physics*; Elsevier, 1968; Vol. 4, pp. 109–141 ISBN 978-0-12-003804-6.
67. Dalgarno, A. Some Problems in Planetary Atmospheres Involving Collision Processes. *Rev. Mod. Phys.* **1967**, *39*, 858–861, doi:10.1103/RevModPhys.39.858.
68. Wall, F.T.; Hiller, L.A.; Mazur, J. Statistical Computation of Reaction Probabilities. *J. Chem. Phys.* **1958**, *29*, 255–263, doi:10.1063/1.1744471.
69. Bunker, D.L.; Blais, N.C. Monte Carlo Calculations. V. Three-Dimensional Study of a General Bimolecular Interaction Potential. *J. Chem. Phys.* **1964**, *41*, 2377–2386, doi:10.1063/1.1726274.
70. Bunker, D.L. Methods in Computational Physics. *At. Mol. Scatt.* **1971**, *10*, 287–325.
71. Percival, I.C. Monte Carlo Methods for Classical Collisions between Electrons and Atoms. *Comput. Phys. Commun.* **1973**, *6*, 347–357, doi:10.1016/0010-4655(73)90043-X.
72. Salop, A.; Olson, R.E. Electron Removal from Atomic Hydrogen by Collisions with Fully Stripped Iron Ions. *Phys. Lett. A* **1979**, *71*, 407–410, doi:10.1016/0375-9601(79)90621-2.
73. Garvey, R.H.; Jackman, C.H.; Green, A.E.S. Independent-Particle-Model Potentials for Atoms and Ions with $36<Z\ensuremath{\le}54$ and a Modified Thomas-Fermi Atomic Energy Formula. *Phys. Rev. A* **1975**, *12*, 1144–1152, doi:10.1103/PhysRevA.12.1144.
74. Green, A.E.S. An Analytic Independent Particle Model for Atoms. In *Advances in Quantum Chemistry*; Elsevier, 1973; Vol. 7, pp. 221–262 ISBN 978-0-12-034807-7.
75. Green, A.E.S.; Sawada, T.; Saxon, D.S.; Moszkowski, S.A. The Nuclear Independent Particle Model. *Am. J. Phys.* **1970**, *38*, 938–938, doi:10.1119/1.1976518.

76. Green, A.E.S.; Sellin, D.L.; Zachor, A.S. Analytic Independent-Particle Model for Atoms. *Phys. Rev.* **1969**, *184*, 1–9, doi:10.1103/PhysRev.184.1.
77. Thomas, L.H. The Calculation of Atomic Fields. *Math. Proc. Camb. Philos. Soc.* **1927**, *23*, 542–548, doi:10.1017/S0305004100011683.
78. Fermi, E. Eine statistische Methode zur Bestimmung einiger Eigenschaften des Atoms und ihre Anwendung auf die Theorie des periodischen Systems der Elemente. *Z. F�r Phys.* **1928**, *48*, 73–79, doi:10.1007/BF01351576.
79. Verhulst, P.-F. Notice Sur La Loi Que La Population Suit Dans Son Accroissement. *Corresp. Math. Phys.* **1838**, *10*, 113–129.
80. Green, A.; Garvey, R.; Jackman, C. A Thomas—Fermi-like Analytic Independent Particle Model for Atoms and Ions. *Int. J. Quantum Chem.* **1975**, *9*, 43–50.
81. Bass, J.N.; Green, A.E.S.; Wood, J.H. An Analytic Independent Particle Model for Atoms. In *Advances in Quantum Chemistry*; Elsevier, 1973; Vol. 7, pp. 263–275 ISBN 978-0-12-034807-7.
82. Szydlik, P.P.; Green, A.E.S. Independent-Particle-Model Potentials for Ions and Neutral Atoms with $Z \leq 18$. *Phys. Rev. A* **1974**, *9*, 1885–1894, doi:10.1103/PhysRevA.9.1885.
83. Reinhold, C.O.; Falcón, C.A. Classical Ionization and Charge-Transfer Cross Sections for H+ + He and H+ + Li+ Collisions with Consideration of Model Interactions. *Phys Rev A* **1986**, *33*, 3859–3866, doi:10.1103/PhysRevA.33.3859.
84. Tökési, K.; Kövér, Á. Electron Capture to the Continuum at 54.4 eV Positron-Argon Atom Collisions. *J. Phys. B At. Mol. Opt. Phys.* **2000**, *33*, 3067–3077, doi:10.1088/0953-4075/33/16/310.
85. Tőkési, K.; Mukoyama, T. Theoretical Investigation of the ECC Peak for Charged Particles with the CTMC Method. *Bull. Inst. Chem. Res. Kyoto Univ.* **1994**, *72*, 62–68.
86. Belkić, D. Electron Capture in High-Energy Ion-Atom Collisions. *Phys. Rep.* **1979**, *56*, 279–369, doi:10.1016/0370-1573(79)90035-8.
87. Allison, S.K.; Cuevas, J.; Garcia-Munoz, M. Experiments on Charge-Changing Collisions of Lithium Ionic and Atomic Beams. *Phys. Rev.* **1960**, *120*, 1266–1278, doi:10.1103/PhysRev.120.1266.
88. Van Eck, J.; Kistemaker, J. Charge Exchange, Ionization and Electron Loss Cross-Sections of Li Ions and Atoms of 5 to 22.5 keV in H2 and He. *Physica* **1960**, *26*, 629–630, doi:10.1016/0031-8914(60)90125-7.
89. Nikolaev, V.S.; Dmitriev, I.S.; Fateeva, L.N.; Teplova, Ya.A. EXPERIMENTAL INVESTIGATION OF ELECTRON CAPTURE BY MULTIPLY CHARGED IONS. *Sov. Phys. JETP* **1961**, *13*, 695–869.
90. Ogurtsov, G.; Kikiani, B.; Flaks, I. Charge Exchange of Alkali Metal Ions on Gas Atoms and Molecules. *Sov. Phys. Tech. Phys.-USSR* **1966**, *11*, 362.
91. Pivovar, L.; Nikolaichuk, L.; Grigor'ev, A. Charge Exchange of Alkali Metal Ions in Alkali Metal Vapor and Inert Gases. *Sov Phys Jetp* **1970**, *30*, 236–239.
92. Pivovar, L.; Levchenko, Y.Z.; Krivonosov, G. IONIZING COLLISIONS AND CHARGE EXCHANGE FOR Li Li 2 AND Li 3 IONS IN. *Sov. Phys. JETP* **1971**, *32*.
93. Dmitriev, I.; Nikolaev, V.; Tashaev, Y.A.; Teplova, V.A. Experimental Study of the Loss and Capture of Electrons by Fast Unexcited and Metastable Heliumlike Ions in Ion-Atomic Collisions. *Zh Eksp Teor Fiz* **1974**, *67*, 2047–2063.
94. Hvelplund, P. Electron Capture and Loss by Ground-State and Metastable Li $^{+}$ in Helium and Argon Targets. *J. Phys. B At. Mol. Phys.* **1976**, *9*, 1555–1565, doi:10.1088/0022-3700/9/9/020.

95. Schultz, D.R.; Reinhold, C.O.; Krstić, P.S. Analysis of Unexplained Oscillations in Intermediate-Energy Ion-Atom Collisions. *Phys. Rev. Lett.* **1997**, *78*, 2720–2723, doi:10.1103/PhysRevLett.78.2720.
96. Lockwood, G.J. Charge-Transfer Cross Sections for H + , Li + , and Na + on N 2. *Phys. Rev.* **1969**, *187*, 161–166, doi:10.1103/PhysRev.187.161.
97. Graham, W.G.; Latimer, C.J.; Browning, R.; Gilbody, H.B. Ionization of Fragmentation of Diatomic Molecular Gases by 5-45 keV Ne $^+$ and Na $^+$ Ions and Ne Atoms. *J. Phys. B At. Mol. Phys.* **1973**, *6*, 2641–2652, doi:10.1088/0022-3700/6/12/030.
98. Sulik, B.; Koncz, Cs.; Tőkési, K.; Orbán, A.; Berényi, D. Evidence for Fermi-Shuttle Ionization in Intermediate Velocity C + + X e Collisions. *Phys. Rev. Lett.* **2002**, *88*, 073201, doi:10.1103/PhysRevLett.88.073201.
99. Sulik, B.; Stolterfoht, N.; Hellhammer, R.; Pei, Z.; Koncz, C.; Tkesi, K.; Berenyi, D. Fermi-Shuttle Acceleration of Electrons in Ion–Matter Interaction. *Nucl. Instrum. Methods Phys. Res. Sect. B Beam Interact. Mater. At.* **2003**, *212*, 32–44, doi:10.1016/S0168-583X(03)01720-8.
100. Tőkési, K.; Sulik, B.; Stolterfoht, N. Fermi-Shuttle Type Multiple Electron Scattering in Atomic Collisions. *Nucl. Instrum. Methods Phys. Res. Sect. B Beam Interact. Mater. At.* **2005**, *233*, 187–190, doi:10.1016/j.nimb.2005.03.103.
101. Sulik, B.; Tőkési, K. Accelerating Multiple Scattering of Electrons by Ion Impact: Contribution to Molecular Fragmentation and Radiation Damages. In *Advances in Quantum Chemistry*; Elsevier, 2007; Vol. 52, pp. 253–276 ISBN 978-0-12-034852-7.
102. Fermi, E. On the Origin of the Cosmic Radiation. *Phys. Rev.* **1949**, *75*, 1169–1174, doi:10.1103/PhysRev.75.1169.
103. Beuhler, R.J.; Friedlander, G.; Friedman, L. Cluster-Impact Fusion. *Phys. Rev. Lett.* **1989**, *63*, 1292–1295, doi:10.1103/PhysRevLett.63.1292.
104. Burgdörfer, J.; Wang, J.; Ritchie, R.H. Estimates for Cluster-Impact Fusion Yields Using the Fermi Acceleration Map. *Phys. Scr.* **1991**, *44*, 391–394, doi:10.1088/0031-8949/44/4/016.
105. Wang, J.; Burgdörfer, J.; Bárány, A. Ionization Spectrum for Ion-Atom Collisions with Zero-Ranged Potentials in One and Three Dimensions. *Phys. Rev. A* **1991**, *43*, 4036–4039, doi:10.1103/PhysRevA.43.4036.
106. Jakas, M.M. Trapping of a Classical Electron between Two Heavy Scattering Centers. *Phys. Rev. A* **1995**, *52*, 866–869, doi:10.1103/PhysRevA.52.866.
107. Jakas, M.M. The Production of High-Energy Electrons during Low Energy Atomic Collisions in Solids. *Nucl. Instrum. Methods Phys. Res. Sect. B Beam Interact. Mater. At.* **1996**, *115*, 255–260, doi:10.1016/0168-583X(95)01559-0.
108. Reinhold, C.O.; Schultz, D.R.; Bechthold, U.; Kraft, G.; Hagmann, S.; Schmidt-Böcking, H. Ternary Ridge of Ejected Electrons from Fast Ion-Atom Collisions. *Phys. Rev. A* **1998**, *58*, 2611–2614, doi:10.1103/PhysRevA.58.2611.
109. Nikolaev, V.S. Calculation of the Effective Cross Sections for Proton Charge Exchange in Collisions with Multi-Electron Atoms. *Sov Phys JETP* **1967**, *24*, 163.
110. Vinogradov, A.V.; Shevel’Ko, V.P. Role of Inner Shells in Charge-Exchange between Protons and Multielectron Atoms. *Sov. Phys. JETP* **1971**, *32*.
111. Shevelko, V.P. One-Electron Capture in Collisions of Fast Ions with Atoms. *Z. Für Phys. At. Nucl.* **1978**, *287*, 19–26.
112. Lin, C.D.; Tunnell, L.N. Subshell Electron Capture Cross Sections of Argon Atoms by Protons. *J. Phys. B At. Mol. Phys.* **1979**, *12*, L485–L490, doi:10.1088/0022-3700/12/16/002.

113. Amaya-Tapia, A.; Martínez, H.; Hernández-Lamoneda, R.; Lin, C.D. Charge Transfer in H + + Ar Collisions from 10 to 150 keV. *Phys. Rev. A* **2000**, *62*, 052718, doi:10.1103/PhysRevA.62.052718.
114. Kirchner, T.; Horbatsch, M.; Keim, M.; Lüdde, H.J. State-Selective Electron-Capture Calculations for *p* -Ar Collisions in an Independent Many-Electron Model. *Phys. Rev. A* **2004**, *69*, 012708, doi:10.1103/PhysRevA.69.012708.
115. Cabrera-Trujillo, R.; Amaya-Tapia, A.; Antillón, A. Differential, State-to-State, and Total-Charge-Transfer Cross Sections for H + Colliding with Ar. *Phys. Rev. A* **2009**, *79*, 012712, doi:10.1103/PhysRevA.79.012712.
116. Houamer, S.; Popov, Yu.V.; Cappello, C.D. Total Cross Sections for Charge Transfer Reactions of Protons with Atomic and Molecular Targets at High Projectile Energies: The Role of Inner Orbitals. *Phys. Lett. A* **2009**, *373*, 4447–4452, doi:10.1016/j.physleta.2009.10.003.
117. Allison, S.K. Experimental Results on Charge-Changing Collisions of Hydrogen and Helium Atoms and Ions at Kinetic Energies above 0.2 Kev. *Rev. Mod. Phys.* **1958**, *30*, 1137–1168, doi:10.1103/RevModPhys.30.1137.
118. Williams, J.F.; Dunbar, D.N.F. Charge Exchange and Dissociation Cross Sections for H 1 + , H 2 + , and H 3 + Ions of 2- to 50-keV Energy Incident Upon Hydrogen and the Inert Gases. *Phys. Rev.* **1966**, *149*, 62–69, doi:10.1103/PhysRev.149.62.
119. Welsh, L.M.; Berkner, K.H.; Kaplan, S.N.; Pyle, R.V. Cross Sections for Electron Capture by Fast Protons in H 2 , He, N 2 , and Ar. *Phys. Rev.* **1967**, *158*, 85–92, doi:10.1103/PhysRev.158.85.
120. Toburen, L.H.; Nakai, M.Y.; Langley, R.A. Measurement of High-Energy Charge-Transfer Cross Sections for Incident Protons and Atomic Hydrogen in Various Gases. *Phys. Rev.* **1968**, *171*, 114–122, doi:10.1103/PhysRev.171.114.
121. Ormrod, J.H.; Michel, W.L. Charge Equilibrium Fractions and Charge-Exchange Cross Sections for Fast Ions in Nitrogen and Argon. *Can. J. Phys.* **1971**, *49*, 606–620, doi:10.1139/p71-079.
122. Morgan, T.J.; Eriksen, F.J. Single- and Double-Electron Capture by 1-100-keV Protons in Collisions with Magnesium and Barium Atoms. *Phys. Rev. A* **1979**, *19*, 1448–1456, doi:10.1103/PhysRevA.19.1448.
123. Rudd, M.E.; DuBois, R.D.; Toburen, L.H.; Ratcliffe, C.A.; Goffe, T.V. Cross Sections for Ionization of Gases by 5-4000-keV Protons and for Electron Capture by 5-150-keV Protons. *Phys. Rev. A* **1983**, *28*, 3244–3257, doi:10.1103/PhysRevA.28.3244.
124. Varghese, S.L.; Bissinger, G.; Joyce, J.M.; Laubert, R. Atomic Total Electron-Capture Cross Sections from C-, O-, F-, and S-Bearing Molecular Gases for ∼ MeV/u H + and He + Projectiles. *Phys. Rev. A* **1985**, *31*, 2202–2209, doi:10.1103/PhysRevA.31.2202.
125. Almeida, D.P.; De Castro Faria, N.V.; Freire, F.L.; Montenegro, E.C.; De Pinho, A.G. Collisional Formation and Destruction of Fast Negative Hydrogen Ions in He, Ne, and Ar Targets. *Phys. Rev. A* **1987**, *36*, 16–25, doi:10.1103/PhysRevA.36.16.
126. Afrosimov, V.; Mamaev, Y.A.; Panov, M.; Fedorenko, N. INVESTIGATION, BY THE COINCIDENCE METHOD, OF CHARGE STATE CHANGES OCCURRING IN THE INTERACTION BETWEEN H+, H0 , AND H- AND THE XENON ATOM. *Sov. Phys. JETP* **1969**, *28*.
127. Clementi, E.; Roetti, C. Roothaan-Hartree-Fock Atomic Wavefunctions. *At. Data Nucl. Data Tables* **1974**, *14*, 177–478, doi:10.1016/S0092-640X(74)80016-1.
128. Bunge, C.F.; Barrientos, J.A.; Bunge, A.V. Roothaan-Hartree-Fock Ground-State Atomic Wave Functions: Slater-Type Orbital Expansions and Expectation Values

for Z = 2-54. *At. Data Nucl. Data Tables* **1993**, *53*, 113–162, doi:10.1006/adnd.1993.1003.

129. Melo, W.S.; Santos, A.C.F.; Sant'Anna, M.M.; Sigaud, G.M.; Montenegro, E.C. Multiple Ionization of Noble Gases by 2.0 MeV Proton Impact: Comparison with Equi-Velocity Electron Impact Ionization. *J. Phys. B At. Mol. Opt. Phys.* **2002**, *35*, L187–L192, doi:10.1088/0953-4075/35/9/102.
130. De Heer, F.J.; Schutten, J.; Moustafa, H. Ionization and Electron Capture Cross Sections for Protons Incident on Noble and Diatomic Gases between 10 and 140 keV. *Physica* **1966**, *32*, 1766–1792, doi:10.1016/0031-8914(66)90091-7.
131. Cavalcanti, E.G.; Sigaud, G.M.; Montenegro, E.C.; Schmidt-B Cking, H. Absolute Cross Sections for Multiple Ionization of Noble Gases by Swift Proton Impact. *J. Phys. B At. Mol. Opt. Phys.* **2003**, *36*, 3087–3096, doi:10.1088/0953-4075/36/14/311.